People's Democratic Republic of Algeria
Ministry of Higher Education and Scientific Research

University of Batna 2– Mostefa Ben Boulaïd
Faculty of Technology
Department of Mechanical Engineering

Thesis

Performed at
(Energetic and Industrial Systems Studying Laboratory-**LESEI**)

Submitted to the Department of Mechanical Engineering in partial fulfilment of the requirements for the degree of:

LMD Doctor in Mechanical Engineering
Option: Energetics

Theme:

Numerical study of two-phase streams in a linear solar concentrator with a new S-shaped absorber. Application: Direct Steam Generation

by:
ACHI Alladdine

Before the Jury Composed of:

SI-AMEUR Mohamed	Professor	The University of Batna 2	President
DEMAGH Yassine	Professor	The University of Batna 2	Supervisor
HACHICHA A. Amine	Professor	The University of Sharjah, UAE	Co-supervisor
BORDJA Lyes	Professor	The University Larbi Ben Mhidi	Examiner
KABAR Yassine	Professor	Nat. Poly. School of Constantine	Examiner
MEBARKI Ghazali	Professor	The University of Batna 2	Examiner
BENMOUSSA Hocine	Professor	The University of Batna 2	Invited

26/10/2023

ACKNOWLEDGEMENTS

Primary, I thank Allah for being able to complete this project with success.

Then, I'm deeply grateful to Professor Demagh Yassine, my thesis director from the university of Mostefa Ben Boulaid of Batna 2, whose constant support, valuable guidance and patience have served as the primary contributor toward the completion of this project. And I would like to thank Professor Hachicha Ahmed Amine from university of Sharjah (UAE), my thesis co-director.

I would like to thank Professor Si-Ameur Mohamed from university of Batna 2 who honoured me by chairing my thesis committee.

I would like to express my sincere gratitude and thanks to Pr. Benmoussa Hocine and Pr. Mebarki Ghazali from university Batna 2, Pr. Bordja Lyes from university of Larbi Ben Mhidi in Oum El Bouaghi, and Pr. Kabar Yassine from National Polytechnic School of Constantine for kindly accepting to be part of committee to judge this work.

I would like to thank my parents, who supported me through these years.

Contents

Chapter III : Mathematical model validation

Chapter IV : Direct steam generation in the DISS test facility

Nomenclature

Roman letters

A	Area (m^2)	L_r	Aperture width (m)
A_C	Area influenced by the single-phase convection $(-)$	$\dot{m}$	Mass flow rate (kg/s)
A_i	interphase contact area (m^{-1})	$\vec{n}$	Normal vector
A_Q	Area influenced by the nucleating bubbles $(-)$	N_a	Nucleation site density (m^{-2})
a	absorber absorptivity $(-)$	P	Pressure (Pa)
Cp	Heat capacity $(J/kg\ K)$	Pr	Prandtl number $(-)$
d_B	Bubble diameter (m)	q	Heat flux (W/m^2)
d_{dep}	Bubble departure diameter (m)	q_k q_k^{turb}	Heat conduction flux, and turbulent heat conduction flux, respectively for phase k (W/m^2)
f	Bubbles departure frequency (s^{-1})	q_l	Convective heat flux to liquid phase (W/m^2)
f_l	Focal length (m)	q_w	Total heat flux from the wall (W/m^2)
F	Interphase force (kg/m^2s^2)	R	Mirror reflectivity $(-)$
g	Gravity (m/s^2)	Re	Reynolds number $(-)$
G	Mass flux $(kg/m^2\ s)$	S	Cross-section (m^2)
h	Heat transfer coefficient $(W/m^2\ K)$	T	Temperature (K)
H	Specific enthalpy (J/kg)	$\vec{U}$	Velocity vector (m/s)
H_{lv}	Latent heat (J/kg)	x	Vapour quality $(-)$
k	Turbulent kinetic energy (m^2/s^2):		

Greek symbols

α	Volume fraction $(-)$	ρ	Density (kg/m^3)
ε	turbulent dissipation rate (m^2/s^3)	Δ	Absorber bending (m)
σ	Stefan-Boltzmann constant $(= 5.670373 \times 10^{-8}\ W/m^2K^4)$	Γ_{ki}	Mass transfer rate due to phase change from phase k to phase i (kg/m^3s)

ϵ	emissivity (–)	σ_t	Surface tension (N/m)
η	Overall optical efficiency $(-)$	τ	Viscous stress $(kg/m \cdot s^2)$
φ	Circumferential angle (°)	τ_g	Transmittance $(-)$
θ_{sun}	the finite size of the sun half angle ($\theta_{sun} = 16'$)	τ^{turb}	Reynolds (turbulent) stress $(kg/m \cdot s^2)$
Φ_k	Wall heat source (W/m^3)	γ	Intercept factor $(-)$
λ	Thermal conductivity $(W/m\,K)$	ν	Kinematic viscosity (m^2/s) :
μ	Dynamic viscosity $(kg/m \cdot s)$		

Subscripts

a	Absorber	l	Liquid
amb	Ambient	q	Quenching
c	Continuous phase	m	Mixture
d	Dispersed phase	mom	Momentum
D	Drag	r	Relative
e	Evaporative	$stat$	Static
eff	Effective	sub	Subcooled
$frict$	Friction	t	Turbulent
g	Glass cover	TD	Turbulent dispersion
i	Interface	v	Vapour
in	Inlet	VM	Virtual mass
BIT	Bubble induced turbulence	w	Wall
I	Inversion	L	Lift

Abbreviation:

DISS	Direct solar steam	DSG	Direct steam generation
DNI	Direct normal irradiance	CFL	Courant-Friedrichs-Lewy number
RPI	Rensselaer Polytechnic Institute		

List of figures

Chapter I

Chapter III

Chapter IV

Chapter V

List of tables

Chapter I

Chapter II

Chapter III

Chapter IV

Chapter V

General introduction

General introduction

As part of the new global policy to reduce dependence on fossil fuels; exploiting new, clean, and renewable energies is essential. Solar photovoltaic and thermodynamic systems have shown an excellent way out of this impasse due to the enormous solar energy potential available in large parts of the world.

The photovoltaic system mainly uses solar cells to capture and convert solar radiation directly into electricity. In contrast, conventional solar thermodynamic systems use mirrors to concentrate a high heat flux on the receiver to heat the fluid passing through it. This energy will produce superheated steam which when expanded in a turbine produces electricity through a generator. One of the most used technologies is the parabolic trough power plant (PTC).

Over the past decade, Direct Steam Generation (DSG) systems using parabolic trough collectors have been considered as a replacement for conventional synthetic oil-based solar power plants, as superheated steam is produced instantly in the absorber tubes. As a result, eliminating substantial heat exchangers between the solar field and the power unit resulted in significant cost savings.

The coexistence of two phases in the absorber affects considerably, and in a general way, the heat, momentum and mass exchange processes. Most importantly, scientists must identify the growth and development of the heat transfer coefficient, pressure drop, and maximum temperature gradient at the absorber wall with certainty to overcome problems that may arise by readjusting operating conditions or by proposing technical solutions to improve them.

In recent studies, Demagh et al. (Refs. [74, 75], Chapter I) developed and patented a new solar receiver with an S-curved shape of the absorber tube whose theoretical studies have revealed advantages when used in conventional power plants operating on synthetic oil.

1. Motivation

In the study by Bitam et al. (ref. [76], Chapter I), the authors performed a comparison between the conventional straight and the S-shaped solar receiver. The investigation concerns monophasic flow (Syltherm 800 synthetic oil). It takes into account the actual 3D heat flux distribution on the outer absorber wall, obtained using the Monte Carlo Ray tracing method.

The mean Nusselt number increases to 63%, and the mean friction factor to 40.8%. The authors concluded that the primary cause of this performance is the emergence of Dean vortices at the absorber bends.

The current work will highlight the performances of the DISS test facility (Almeria, Spain) (Refs [4-5], Chapter I) adopting the scenario where the conventional straight solar absorber came to be replaced by the S-shaped absorber tube, newly developed and designed by Demagh et al. (Refs. [74, 75], Chapter I). Besides, a comparative study of the numerical results for similar operating conditions will be performed, highlighting its advantages and disadvantages.

2. Objectives of this thesis

The main objective of this numerical study is to conclude the performance of the S-shaped solar absorber in the production of superheated steam. Simulations, entirely performed with open-source software, highlight the effects of the bends of the new absorber on void fraction, pressure drop, and maximum wall temperature difference around the absorber.

This work aims to:

- Use the Monte Carlo ray tracing method in Tonatiuh software (open source) to generate heat flux distribution around the outer wall of the absorber tube (straight and S-shaped).
- Use OpenFOAM (open source) as a simulator of boiling flow in the solar absorber for a commercial scale, as in the test facility of Almeria (Spain).
- Couple the output of Tonatiuh heat flux results with OpenFOAM boundary condition via the swak4FOAM library (open source).
- Considering each collector alone, the CFD challenge of processing a domain of length 400m, which represents the total straight length of the eight collectors composing the evaporation section, has been overcome. Then, the output results of the first collector are reproduced at the input of the second to the last.
- Compare the performance of the S-shaped solar absorber with the straight one.

3. Research approach

In literature, the Eulerian-Eulerian formulation with the RPI (Rensselaer Polytechnic Institute) wall boiling model is suitable for studying boiling flow in straight and coiled tubes. It provides accurate results for void fraction and pressure drop. It overcomes the problems related to the VOF method, such as the mesh sensitivity (the VOF method strongly depends on mesh refinement to give better results) and the coefficient calibration of the Lee model (Ref. [19], Chapter II) of the phase change.

So, the research approach of the current work is:

- To validate the mathematical model with the experimental study of Wojtan et al. (Ref. [11], Chapter I), dealing with boiling flow in a horizontal and straight laboratory-scale tube.

- To validate the same mathematical model with experimental work of boiling flow within a horizontal coiled tube of Sajadi et al. (Ref. [51], Chapter I), dealing with boiling flow in a horizontal and coiled laboratory-scale tube.
- To validate the same mathematical model with DSG in the solar absorber of the commercial-scale parabolic trough in the DISS test facility of Almeria, Spain.
- Use the validated mathematical model to anticipate the thermohydraulic behaviour of DSG in the new S solar absorber compared to the straight one.

4. Thesis layout

After a general introduction, motivation, objective and research approach of this work, the thesis will be organized as follows:

- Chapter 1: Presents an introduction to different solar concentrator technologies, a literature review of boiling flow in straight and coiled tubes, as well as on DSG in the parabolic trough, and the various improvement techniques (modification/ insertion) used in the DISS test facility.
- Chapter 2: Presents a review of different mathematical models used in literature about the Eulerian method with RPI wall boiling.
- Chapter 3: Presents the validation of the mathematical model with the boiling flow in horizontal straight and coiled laboratory-scale tubes.
- Chapter 4: Presents the validation of the previous mathematical model with DSG in the commercial-scale parabolic trough in the DISS solar power plant, verifying the accuracy of the solar absorber parameters such as the external heat flux and energy loss modelling.
- Chapter 5: Presents the scenario in which the S-shaped absorber receiver replaces the conventional straight one for DSG (DISS solar power plant) and compares their performances.

Finally, a general conclusion summarises the main findings and recommendations and gives a strategy for future studies.

Chapter I : Literature review

I.1. Introduction

Solar energy, the world's leading renewable energy source, is created by nuclear fusion that takes place in the sun and releases in space through electromagnetic radiation. It is harnessed in daily life using different technologies to generate electricity or to be used in solar lighting, heating, ventilation, distillation, Etc.

Solar energy is an attractive source of generating electricity due to its wide geographic distribution, for which it is possible to determine the solar direct normal irradiation for any solar power plants based on geolocation (see Figure I.1).

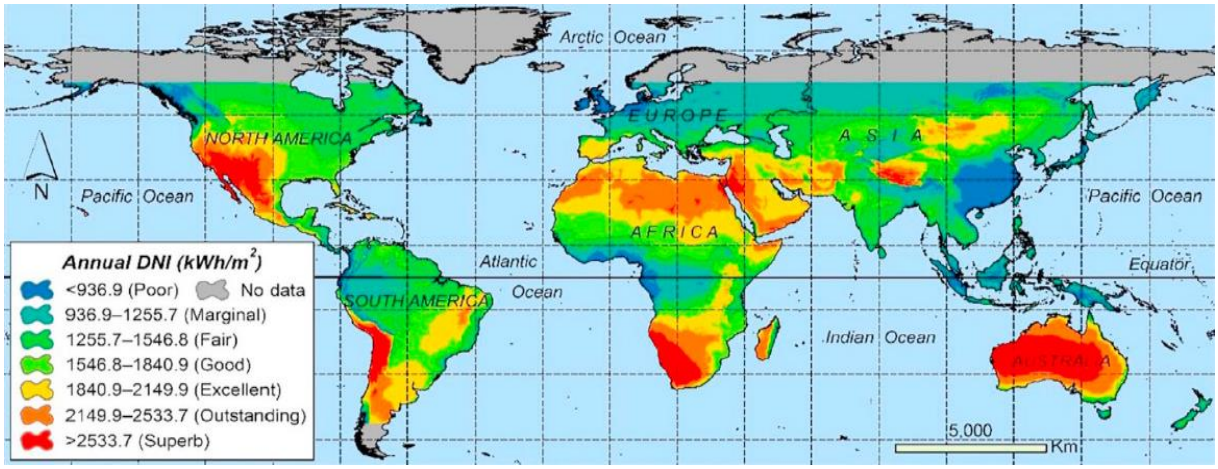

Figure I.1. Average Annual DNI in the world [1].

In recent literature, DSG is the next step of advancement by replacing the heat transfer fluid (oil and molten salt) with water [2-5]. It has the advantage of avoiding the risk of toxic oil leakage and eliminating the heat exchangers used for steam production, which leads to a compact system with a minor investment cost.

In the last two decades, DSG in parabolic troughs of the DISS test facility [2-3] has been studied experimentally and numerically to enhance operating conditions and reduce the maximum temperature difference in the receiver to avoid thermal stress. Many papers in the literature propose inserting metal foams or tapes, others suggest etching micro-channels in the inner surface of the receiver, and others tried to find the best operating conditions without any modifications in the receiver using the last developed thermo-hydraulic models.

The main objective of this thesis is to perform a 3D numerical study of the phase change fluid (DSG) flows in a newly designed S-shaped absorber considering the actual operating conditions of the DISS test facility and determining its advantages and disadvantages.

I.2. Solar concentrator technologies

Solar concentrator power plants mainly use the beam part of solar radiation since concentration needs parallel rays. The area where solar radiation is incident in the concentrator is called “the aperture”. In contrast, the area of the absorber that receives the reflected rays is called “the receiver area”. The ratio of the aperture area to the receiver area is called the ‘’concentration ratio’’. All solar concentrators of solar power plants need to track the sun throughout the day and can be classified according to their way of concentrating the solar rays on the receiver, which can be linear (1 axis of tracking) or punctual (2 axes of tracking).

I.2.1. Parabolic trough

It is a type of linear concentration technology. The solar rays that hit the mirror parallel to its plane of symmetry are reflected toward the absorber tubes located on the focal lines (see Figure I.1.a). The heat transfer fluid in the collector loop can be synthetic oil or water/steam, depending on solar thermal power use.

I.2.2. Fresnel collectors

It is another type of linear concentration technology [6]. Direct solar radiation is reflected on several long, flat, or slightly curved single-axis tracking mirrors onto the receiver (see Figure I.1.b). It outperforms the parabolic trough collectors in terms of low wind load, low weight structure, and easy accessibility for maintenance. It can provide heat up to 400 C and is used for thermal oil and water for DSG.

I.2.3. Parabolic dishes

It is a punctual concentration technology. It consists of a paraboloid reflective surface that collects and reflects solar rays to the receiver (see Figure I.1.c). Commercially available parabolic dish collectors can attain a higher concentration ratio than 2000 [7]. Its primary application is generating electricity, using Stirling engines mounted at the central receiver.

I.2.4. Tower collectors

It is another punctual concentration technology that uses small reflectors called heliostats, with two axes of orientation to reflect solar rays to the receiver up in the tower [8] (see Figure I.1.d). It is often cheaper than the previously cited technology (parabolic dishes) as the receiver is centralized in the tower, not the reflector.

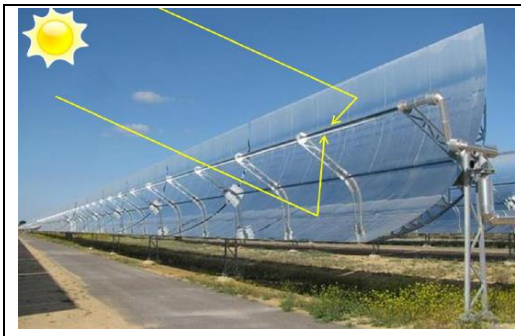

(a) Parabolic trough

(b) Fresnel collectors

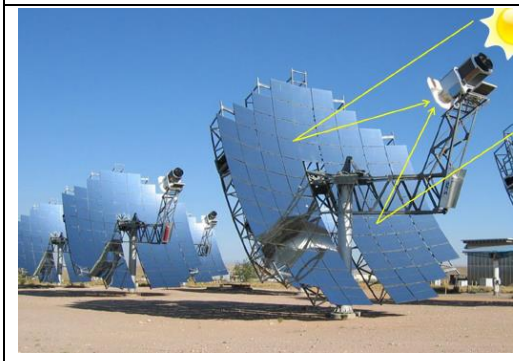

(c) Parabolic dish

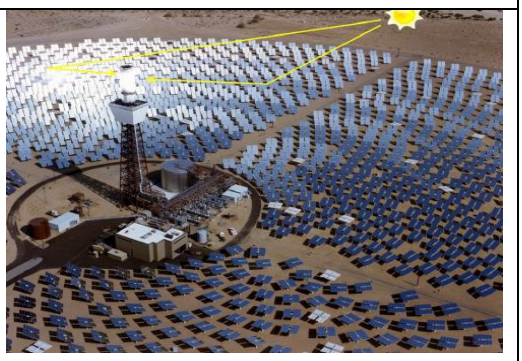

(d) Tour collectors

Figure I.2. The different solar concentrator technologies [9].

Critical information on the four CSP technologies is presented in Table I.1. Brief details are provided on the working temperature and concentration ratio to consider the appropriate concentration technology based on the thermodynamic cycle requirements.

Table I.1. The main characteristics of the four leading CSP technologies [10].

	Focusing type	**Tracking axis**	**Concentration ratio**	**Temperature range (C)**
Parabolic trough	Linear	1 axis (N-S)	50-90	150-550
Fresnel collectors	Linear	1 axis (N-S)	35-170	150-400
Parabolic dish	Punctual	2 axis	Less than 3000	300-1500
Tower collectors	Punctual	2 axis	600-1000	300-1200

I.3. Boiling flow review

Two-phase boiling flow in horizontal straight or coiled tubes is widespread in various industrial applications such as power plants, refrigeration systems, desalination plants, DSG, Etc.

The current study is about DSG in solar absorbers, so the two-phase boiling flow is the task of interest. The presence of two phases inside the absorber tube can affect the heat transfer coefficient and pressure drop. The phase distribution can appear under different flow patterns [11-12]. The expected flow regimes observed in these studies include bubbly, intermittent, stratified wavy, annular, and mist flow. Such flows depend on fluid properties, mass velocity, vapour quality, and geometry. The transition from one flow pattern to another in boiling flow is complicated. In this situation, any attempt to deeply understand the phenomena in solar absorbers at the time of the phase change must go through the knowledge of the flow pattern map.

I.3.1. Horizontal tubes

I.3.1.1. Flow pattern map

In boiling flow, the majority of research on flow pattern maps is developed for horizontal straight tubes, as it is the most common geometry in the industry.

The general flow patterns map shown in Figure I.3 in the horizontal tube are [11-12]:

Bubbly flow: The bubbles are distributed throughout the liquid at the beginning of evaporation due to low vapour quality and tend to move to the upper part of the tube at low liquid velocities. For higher velocities, their distribution seems uniform.

Stratified flow: The two phases, liquid and vapour, are separated with a straightforward interface due to the dominant gravity effect. The vapour phase is at the top, and the liquid phase is below. Usually, this phenomenon occurs when both phases have low velocities.

Stratified-wavy flow: When the vapour velocity increases in the stratified flow, the interface disturbance will occur, and the waves appear and develop in the flow direction.

Slug flow: As the amplitude of waves in stratified wavy flow are high, they can frequently touch the upside of the tube, which can play a significant role in enhancing the heat transfer coefficient when evaporating.

Plug flow: In low vapour quality, for a low gas flow rate and a moderate liquid flow rate, bubbles can coalesce to create elongated and considerable bubbles that remain dispersed in the

liquid phase. It must be known that in this flow pattern, the tube's inner surface is fully wetted by the liquid phase.

Intermittent flow: This irregular flow pattern represents a mixture of plug and slug flow patterns.

Annular flow: It occurs at high vapour quality. A liquid film covers the channel's perimeter, and the vapour passes through the core at high velocity.

Mist flow: It occurs at the highest vapour quality, the vapour is the dominant phase, and liquid droplets disperse through it.

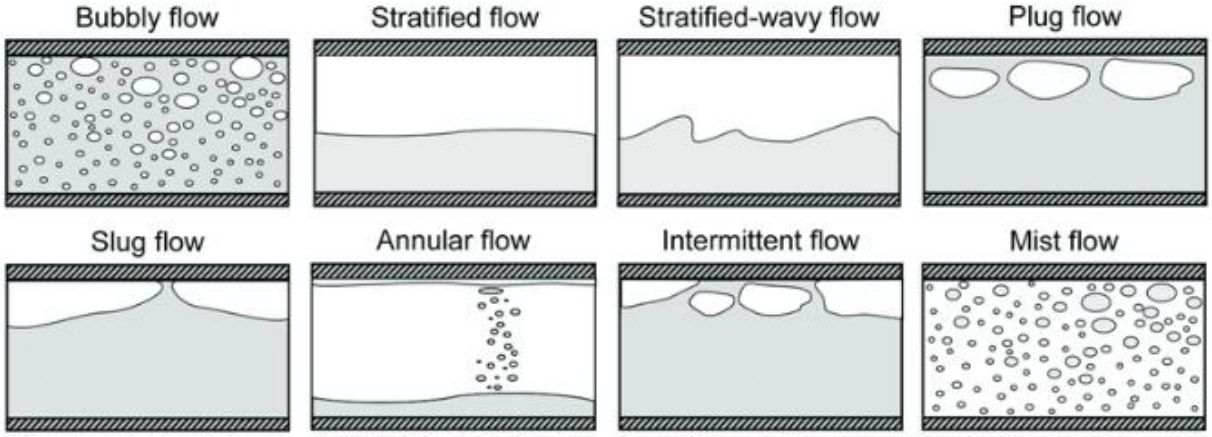

Figure I.3. Two-phase flow pattern [5].

Initially, diabatic two-phase flow regimes used the developed flow patterns, such as the Baker map [13], Taitel and Dukler map [14], and the Hashizume map [15]. They were limited by the range of their experimental data and needed to generate better diabatic flow results**.** **Steiner** [16] extended the Taitel and Dukler map [14] to a diabatic flow pattern map.

Kattan [17] (1996) and **Kattan et al.** [18–19] (1998) make the **Steiner** map easier by manipulating the axis of the map as mass velocity in function with vapour quality to follow the flow patterns during the evaporation. They also investigated the dry out of the annular flow, which leads to mist flow. In addition, the authors proposed new correlations of heat transfer coefficients based on flow patterns.

Thome and Hajal [20] (2003) presented a simple mathematical method to calculate stratified angle directly from the void fraction instead of the previous iteration method, enabling the calculation of the dimensionless variables quickly and implementing the Kattan map directly.

Wojtan et al. [11] (2005) proposed the latest version of the Kattan map utilizing a visual approach. The dynamic void fraction was used to split the stratified wavy region into three

distinct sub-zones: slug, slug/stratified wavy, and stratified wavy. As a result, they update the Kattan map to include all boiling flow regimes seen in horizontal tubes.

Figure I.4 shows the last most developed version of the flow pattern map; it is an example of flow pattern map distribution for refrigerant R-22 boiling flow in a horizontal tube with a mass velocity of 100 $^{kg}/_{m^2\ s}$, an inner diameter of 13.84 mm, heated with 2.1 $^{kW}/_{m^2}$ heat flux, and five degrees of saturation temperature.

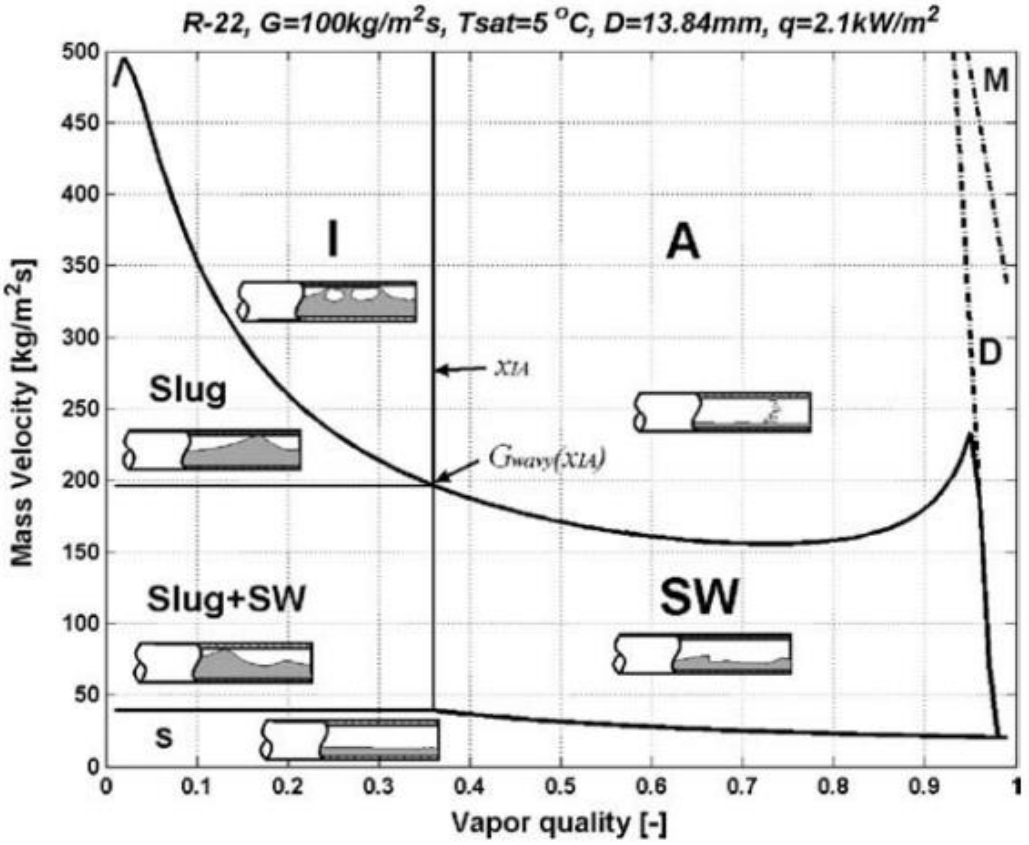

Figure I.4. Flow pattern map for R22 at Tsat=5C (mass velocity VS vapour quality) [11].

The advantages of the Wojtan et al. map [11] are:

- It allows us to follow the change in flow pattern map with vapour quality for certain mass velocity, as in most evaporators.
- It proposes correcting the Kattan et al. map [18] that predicting accurately 96.2% flow patterns for 720 experimental points.
- The lines separating flow patterns are defined by equations that depend mainly on fluid properties, vapour quality (solid lines), and heat flux (dash lines). It makes it simpler to use with programming software and provides different maps for different fluids.

- In recent research [21-23], it is increasingly employed to anticipate the flow pattern in direct steam generation in parabolic troughs.

To obtain this flow pattern map is shown in Ref [11].

I.3.1.2. Void fraction

The void fraction is the ratio of the surface of the vapour to the cross-section. It is defined as:

$$\alpha_v = \frac{A_v}{A_{cross-section}} \quad \text{(I. 1)}$$

Where A_v is the area occupied by the vapour in a cross-section.

The void fraction is influenced by different fluid properties (density, surface tension, Etc.) and flow properties (velocities, geometry, vapour quality, Etc.).

Wojtan et al. [11, 12, 24, 25] used a new optical measurement system, for boiling flows, at the outlet of a horizontal glass tube test section of 13.6 mm diameter. The dynamic and time-averaged void fraction is recorded using R22 and R-410A as working fluids. The mass velocity ranges (70-200 kg/m^{2}s) and vapour quality (0.01-0.95). A total of 227,000 images were analyzed during the experiment. The void fraction was evaluated regarding the homogeneous model and Rouhani-Axelsson void fraction correlation [26] (Eq. (I.2)). Compared to the experiment data, the homogeneous model overpredicts the void fraction for all vapour qualities, but the Rouhani-Axelsson correlation shows excellent consistency and agreement. The Rouhani-Axelsson correlation for the horizontal tube is defined as:

$$\alpha_v = \frac{x}{\rho_v}\left[\left(1 + 0.12(1-x)\right)\left(\frac{1-x}{\rho_l} + \frac{x}{\rho_v}\right) + \frac{1.18(1-x)[g\sigma_t(\rho_l - \rho_v)]^{0.25}}{G\rho_l^{0.25}}\right]^{-1} \quad \text{(I. 2)}$$

I.3.1.3. Frictional pressure drop

The pressure drop measured in a two-phase flow is the total pressure drop. It consists of three components:

$$\Delta P_{total} = \Delta P_{stat} + \Delta P_{frict} + \Delta P_{mom} \quad \text{(I. 3)}$$

(ΔP_{stat}) is the static pressure drop, which is zero for a horizontal tube. As a consequence, the two-phase frictional pressure drop (ΔP_{frict}) is:

$$\Delta P_{frict} = \Delta P_{total} - \Delta P_{mom} \quad \text{(I. 4)}$$

Where (ΔP_{mom}) is the momentum pressure drop produced by flow acceleration in a diabatic two-phase flow. (ΔP_{mom}) is assumed as [39]:

$$\Delta P_{mom} = G^2 \left\{ \left[\frac{(1-x)^2}{\rho_l(1-\alpha_v)} + \frac{x^2}{\rho_v \alpha_v} \right]_{out} - \left[\frac{(1-x)^2}{\rho_l(1-\alpha_v)} + \frac{x^2}{\rho_v \alpha_v} \right]_{in} \right\} \quad \text{(I. 5)}$$

(ΔP_{mom}) is zero for an adiabatic channel.

In the literature, there are many correlations to evaluate the two-phase frictional pressure drop in horizontal tubes. The common correlations are from **Lockart & Martinelli [27] (1949), Bankoff [28] (1960), Thom [29] (1964), Baroczy [30] (1965), Chawla [31] (1967), Chisholm [32] (1973), Gronnerud [33] (1979), Friedel [34] (1979), Olujic [35] (1985), Muller-Steinhagen & Heck [36] (1986), Hart [37] (1989),** and **Ouldi-Didi [38] (2002).**

These are empirical correlations with excellent precision in their experimental database ranges.

Despite several theoretical and experimental studies, no reliable correlation predicts two-phase pressure drop accurately, as they need to account for flow patterns. They do not capture the peak in the curve of frictional pressure drop. Most do not use appropriate void fractions in their correlations to get appropriate velocities for vapour and liquid phases and, thus, the corresponding pressure drop.

Quibén and Thome [39] (2007) and **Quibén [40] (2005)** conducted a series of experimental frictional pressure drop measurements during evaporation in horizontal tubes using the same types of equipment as Wojtan et al. [25] and the flow map of Wojtan et al. [11]. They provided considerable data using different refrigerants (R134a, R22, R410A) for mass velocity ranges (70-700 kg/m^{2}s) and heat flux (6-57.5 kW/m^2), using test sections with inner diameters of 8 mm and 13.8 mm.

Quibén and Thome [41] (2007) used the experimental results of **Quibén and Thome [39] (2007)** to develop new correlations for different flow patterns with smooth transition when the flow pattern change during phase change to overcome the limitation of previous correlations [27-38]

The detailed Moreno-Quiben correlations of different frictional pressure drop is given in Ref [41].

I.3.2. Coiled and bend tubes

As coiled and bend tubes have no specific geometry, there is no generalised flow map, void fraction, or frictional pressure drop correlations.

Yang et al. [42] (2008) conducted experiments on boiling flow in a horizontal coiled tube with a 6 mm inner diameter, using joule heating on its outer surface. The tube is made up of

quartz (glass) and is highly transparent, enabling visualization of flow patterns inside the tube. The general flow patterns observed in horizontal straight parts are bubbly, slug, stratified, and stratified wavy. For the bend regions, the liquid phase is pushed toward the outer side due to centrifugal force, whereas the vapour phase remains near the inner side of the bend.

Cioncolini et al. [43] (2008) studied pressure drop inside subcooled and saturated water boiling flow experimentally in a vertical coiled tube with inner diameters 4.03 mm and 4.98 mm, with three different coil diameters. Among different correlations, only the straight tube Lockhart and Martinelli [27] could successfully predict pressure drop in saturated flow, which hints that the curvature effect has no significant importance.

Xiao et al. [44] (2018) studied experimentally two-phase flow water-steam inside a vertical coiled tube with inner diameters of 12.5 mm and 14.5 mm and three different coil diameters of 180, 280 and 380 mm. The operating pressure range is 2 – 8 MPa. They found that Ju's correlation [45] gives the best predictions among many correlations with a small average error of about 5%.

Ferraris and Marcel [46] (2020) used the experimental data of a vertical coiled tube from Santini et al. [47] to test diverse correlations for a frictional pressure drop of a two-phase flow. The correlations such as Colombo [47] (2015), Guo [48] (2001), Xiao [44] (2017), Cioncolini [49] (2016), and Hardik [50] (2017) were found not successful enough to predict friction pressure drop. The newly developed correlation based on the homogeneous equilibrium model that converges for single-phase flow correlation at vapour qualities at 0 and 1 fit the experimental data with an average error of 7.4%. The new correlation is recommended for water-steam flow in a vertical helical tube, with liquid Reynolds number 20 000 – 124 000, pressure 1 – 8 MPa, curvature between 0.01 – 0.08, and vapour qualities 0 – 1.

Sajadi et al. [51] (2021) studied heat transfer and pressure drop characteristics of R1234yf boiling flow experimentally in a horizontal straight tube and a horizontal coiled tube (the same horizontal tube is custom-made to be coiled). Under the experimental conditions, using a coiled tube instead of a horizontal straight tube leads to an increase of 299% in heat transfer coefficient, and pressure drop increased by up to 227%.

I.4. Direct steam generation in parabolic trough review

The enormous structures of solar collectors and the long runtime of 3D simulations pose a real CFD problem; only a few papers in the literature address this. A different approach to reducing the cost of simulations was to use empirical or semi-empirical correlations.

Eck & Steinmann [52] (2004) studied DSG in the solar absorber numerically as a 1D problem with Matlab software and used empirical correlations in their mathematical model. To account for the void fraction, they used the Rouhani-Axelsson correlation. Friedel correlation [34] for frictional pressure drop is adopted as it is the best according to the European DISS project [53]. They validated their models with the DISS test facility under actual operating conditions for pressure between 30 and 100 bar. In the second step, they used the finite element method in Ansys to get the solar absorber temperature fields. They found the maximum wall temperature difference in the secure zone (below 50K). They also refer to the importance of installing valves at the inlet of every single collector loop to prevent flow instabilities.

Lobón et al. [54] (2014) used a homogeneous boiling model under a commercial STAR CCM+ package to study DSG in the DISS test facility. They used a normalized function to model noun-uniform heat flux around the absorber. They validated their CFD simulation with the solar absorber's temperature, pressure, and maximum wall temperature difference for all collectors.

Hoffmann et al. [55] (2014) used a code called ATHLET to study DSG in the parabolic trough in the DISS facility. They found a good agreement between the numerical and the experiment results for transient outlet temperature, steam mass flow, and inlet pressure.

Elsafi [22] (2015) studied the DSG in the parabolic trough with the once-through mode of platform solar DISS. They used a new 1D mathematical model in EES software based on the flow map of Wojtan et al. [11]. To accurately estimate the heat transfer coefficient, they used Wojtan correlations for different flow patterns [56]. For the frictional pressure drop, they used Thome-Quiben correlations [41] as they were developed for the Wojtan map. For heat loss, they used experimental correlation of LS3 [57]. There is good agreement between numerical and experimental temperature and pressure along the absorber for different cases.

He observed that stratified wavy flow is dominant when DNI is low, without annular flow in the evaporation section. He suggests reducing inlet pressure to shift the annular flow transition to lower steam quality.

Biencinto et al. [58] (2016) developed 1D, a quasi-dynamic model. They adopted the Rouhani-Axelsson correlation for the void fraction [26], Friedel [34], Muller-Steinhagen and Heck [36], and Moreno-Quiben correlations [41] for frictional pressure drop. For heat transfer correlation, they use the Kandlikar correlation [59]. The model is validated with experimental data obtained from DISS solar test facility; their numerical results consist of temperature and pressure drop along all collectors from preheating to superheating sections for different inlet

pressure drops (3, 6, 10 bar). They also validate the transient outlet temperature with the experiment.

Kumar & Reddy [21] (2018) developed a 1D thermo-hydraulic model to study DSG in the solar absorber of the parabolic trough of the DISS facility using the FORTRAN code. To account for the flow pattern transition during evaporation, they used Wojtan map [11], along with empirical correlations for pressure drop (Lockart & Martinelli [27], Gronnerud [33], Thome and Quiben [41]). Heat transfer coefficient (Gungor & Winterton [60], Shah [61], Wojtan et al. [56]), and they also took into account the presence of a glass envelope. The comparative study illustrated that all the two-phase flow correlations could estimate fluid temperature and pressure in good agreement with experimental results.

Hachicha et al. [62] (2018) developed a mathematical model based on the finite volume method to determine temperature and pressure drop in the solar absorber, considering the realistic non-uniform heat flux distribution and the influence of bending and conic eccentricity. The heat loss is modelled with experimental correlation [57]. This optical model is coupled with the fluid mathematical model with energy balance. For the 1D fluid model, they used the Gnielinski correlation [63] to account for the Nusselt number in the case of single-phase flow, along with the Blasius equation that uses Moody friction factor correlation [64]. For two-phase flow, they used the Odeh correlation [65] for the heat transfer coefficient and Friedel for pressure drop [34]. They validated their mathematical model with the DISS test facility with a once-through operating mode. After that, they studied the effect of inlet temperature and pressure and DNI and incident angle on the maximum wall temperature difference. They found that the increase in inlet temperature can lead to the risk of bending in superheat section. The contrary happens to inlet pressure, which seems favourable as the maximum wall temperature difference is smaller due to the annular flow inside the absorber. They also noticed that the increase in DNI will slightly reduce the preheating section, but it can lead to a higher wall temperature difference in the superheating section. It can pass 50K, and consequently, the risk of thermal bending. In the same trend, they studied the impact of incidence angle on the maximum wall temperature difference. Increases in incidence angle are similar to decreasing DNI due to the cosine effect. It is recommended to work with a normal incidence angle and higher DNI with attention to maximum wall temperature difference.

Also, in their simulations, they studied the two-phase flow operating conditions' effect on the overall efficiency. They found that efficiency increases in preheating and evaporation sections and decreases in the superheating section. The same observations were noted in their

simulation: the heat transfer coefficient increases with mass velocity from preheating to evaporation and decreases in the superheating section.

We can agree as the same observations are studied experimentally for boiling flow in horizontal tubes by [19, 25] (look boiling research). They stated that the heat transfer coefficient increased from low to high vapour quality (corresponding slug and stratified wavy to annular flow) and then decreased after the dry-out of the annular flow, followed by mist flow and superheated steam.

Pal and Kumar [66] (2021) studied the DSG in the parabolic trough with identical flow parameters to the DISS test facility employing the Ansys Fluent 2020R1 code and the Eulerian multiphase wall-boiling model. Using non-uniform heat flux distribution around the receiver obtained by Malan and Kumar [67]. The 12 m length of a solar receiver was considered with and without a glass envelope. They observed that the vapour fraction at the outlet decreased with increased operating pressure, and the pressure drop was higher at low operating pressure.

I.5. Improvements in direct steam generation in parabolic trough review

I.5.1. Modification in the solar absorber by introducing inserts

Rojas et al. [68] (2008) studied with the HELIOS program the benefice of integrating capillary systems (porous coating or micro-channels) in LS3 solar collectors of the DISS test facility. The stratified flow in low mass velocity or after the dry out of annular flow can cause a big temperature difference in the absorber cross-section due to the low conductivity of steam and thereby cause thermal stress on the receiver. The internal surface of the absorber can be kept wet if the appropriate capillary system is integrated. They calculated the matrix of the optimal characteristics of the capillary system. They suggested modifying the porous coated pipes with metallic wire meshes or using a milling machine for etching micro-channels in the inner surface of the receiver because of the absence of commercial pipes with integrated capillary systems of diameter above 4 cm.

Another way to improve solar receivers' performances is by using inserts, as described below in the literature. The primary purpose is to reduce the maximum circumferential temperature difference in the absorber tube in the superheating section [69–72], which can risk receiver bending. According to Eck et al. [52], the safe temperature difference should not pass 50 K.

Wang et al. [69] (2013) investigated the consequence of inserting metal foams in the receiver tube of the parabolic trough in the superheating section numerically, at the top and the bottom of the receiver, with different heights (H), and metal foams porosity, with realistic noun uniform heat flux obtained by Monte Carlo Ray Trace (MCRT) method

- For (H=0.25) (the best thermohydraulic result) in the bottom of the receiver, the Nusselt number improves about 5-10 times, the friction factor rises about 10-20 times, and the performance evaluation criteria vary from 1.4 to 3.2.
- For (H=0.75) (the best thermal result) at the top of the receiver, the Nusselt number improves 10-12 times. The friction factor rises 400-700 times as the flow accelerates in the narrow channel, and the PEC vary from 1.1 to 1.5.

The largest circumferential temperature differential on the receiver's outer surface falls by around 45%, significantly decreasing thermal stress.

Liu et al. [70] (2016) studied numerically the single-phase water steam inside the solar absorber with twisted tape inserts to reduce circumferential temperature difference. For simplification, they used $q_{upper} = 0\ W/m^2$ heat flux at the upper half outer surface of the cylinder. In contrast, $q_{bottom} = 30\ 000\ W/m^2$ in the bottom half; the operating conditions are similar to the DISS test facility. The results reveal that the multi-longitudinal vortices flow efficiently minimizes the circumferential temperature difference and that higher viscous dissipation causes a drop in circumferential temperature difference. However, there is a limit to temperature difference reduction when generating more multi-longitudinal vortices.

Kumar and Reddy [71] (2020) the superheating section was studied numerically by inserting a metal foam in the lower half of the absorber. They considered the noun uniform heat flux with a normalized function, and the heat loss is adopted from experimental correlation [57] in the DISS test Facility [2,3]. The results showed that the absorber tube with inserted metal foam helps reduce circumferential thermal stress by 47% to 72% in the range of operating conditions. The Nusslet number increased up to 10 times. The performance evaluation criteria $\left(PEC = \frac{(Nu/Nu_{clear})}{(f/f_{clear})^{1/3}}\right)$ was found to be enhanced up to 5. The maximum gain in the net energy efficiency is 3.71% due to enhanced heat transfer and reduction of heat loss, and 2.32% in the exergy efficiency of the collector.

Housseinalipour et al. [72] (2020) proposed a receiver tube with twisted tape inserts. In their numerical study, the twisted tape's generated vortices in the core of the flow led to heat transfer enhancement (Nusselt number increases 1-1.7 times) and reduction in circumferential temperature gradient by 10-45%, which significantly reducing thermal stresses. They also found an increase in friction factor (1.8 – 4.1 times) in the range of their studies.

I.5.2. Receiver tube maximum circumferential temperature decrease without introducing inserts

Eck et al. [73] (2004) explored the influence of tilting the collector (by 4°) experimentally in the DISS test facility. They found that the maximum circumferential temperature difference decreased in the evaporation section. However, in the superheating section, it remains higher. Consequently, tilting can only affect two-phase flow distribution, especially the stratified flow that causes this problem. Hence, their main conclusion is that tilting of the collectors is inefficient for DSG in the parabolic trough because the horizontal absorber ensures adequate cooling in the evaporation section.

The literature below focuses mainly on improving operating conditions:

Elsafi [22] (2015) developed a 1D comprehensive modelling approach for direct steam generation in the parabolic trough. His model basis is the Wojtan map [11]. He validated his model with the DISS test facility and tested the effect of DNI, inlet pressure, and temperature on the annular flow length in the evaporation section (annular flow shows the highest transfer coefficient [56]). He found:

- Considering the outlet condition as superheated steam at 400 °C in all DNI cases, low DNI leads to stratified wavy flow without the presence of annular flow in the evaporation section (annular flow is shown only for higher DNI).
- Low inlet pressure shifts the annular flow transition to low steam qualities, favouring the heat transfer coefficient.
- Higher inlet temperature lead to a higher filling percentage of annular flow.

His main conclusion is that to obtain a higher heat transfer coefficient (which occurs in annular flow), one must work with high DNI and low inlet pressure.

Hachicha et al. [62] (2018) developed a thermohydraulic model to study the effect of inlet temperature, pressure, DNI, and incident angle. They confirmed the previous conclusion that the superheating section is the most vulnerable to bending and thermal stress. They found that:

- The higher operating pressure leads to a lower maximum temperature difference in the superheating section.
- Higher DNI leads to a higher maximum wall temperature difference in the superheating section.
- A higher incident angle leads to a lower maximum temperature difference in the superheating section since the incident angle is just the cosine effect of DNI.

They suggest as a main conclusion to work with a higher operating pressure and a low DNI or a high angle of incidence if (the DNI is high).

I.6. Conclusion

This chapter presented the state of the art of DSG in the parabolic trough of the DISS test facility in Almeria (Spain), as it was the base of most studies in the literature. The flow pattern of the DSG in the solar absorber is similar to the boiling flow in the horizontal tubes. Therefore, samples of papers about boiling flow patterns, void fraction, and frictional pressure drop were presented. They were followed by numerical studies in DSG in the DISS facility using 1D models based on empirical and semi-empirical correlations (to model pressure drop, heat transfer coefficient, and void fraction), as the simulation will need an extended time for 3D numerical simulations.

The second part dealt with different proposals for improving the heat transfer coefficient, which would have as direct consequences the decrease of the maximum wall temperature difference, lower thermal stresses and a controlled bending of the absorber. DISS found that the highest maximum temperature difference occurs in the superheat section; therefore, most researchers' scenario focuses on inserting metallic foams or twisted tape in this region, reducing the maximum temperature difference to about 47% to 72%. The Nusselt numbers increased up to 10 times. On the other hand, heat exchange enhancement techniques that did not introduce any insertions, such as tilting the absorber, were useless because the maximum temperature remained higher in the superheated part. Some papers have considered optimal operating conditions to improve the heat transfer coefficient by adopting low operating pressure and high DNI, which contradicts the maximum reduction of temperature difference. Therefore, the best solution may be to work with optimal conditions that improve the heat transfer coefficient in the evaporation section and use insertions in the superheated section.

Recently, we have seen promising results in improving thermal performance in conventional (non-phase change) solar receivers using a new configuration of absorber tubes. These studies praise the use of a new S-curve absorber configuration proposed by Demagh et al. [74, 75]. Numerical results obtained by Bitam et al. [76] have shown an improvement in the thermal performance of the absorber without using any insertion. Indeed, curved shapes are known to have the capacity to produce, in a natural way, vortices within the flow due to an imbalance of dynamic forces. Consequently, in this study, we proposed to replace the classical straight absorber of the DISS test installation with the S-shaped one, thus highlighting its advantages and disadvantages in the DSG.

References

[1] Pravalie R, Patriche C, Bandoc G. Spatial assessment of solar energy potential at global scale. A geographical approach. *Journal of Cleaner Production*. 2019; 209: 692-721.

[2] Eck M, Zarza E, Eickhoff M, Rheinländer J, Valenzuela L. Applied research concerning the direct steam generation in parabolic troughs. *Solar energy*. 2003; 74(4): 341-351.

[3] Zarza E, Valenzuela L, Leon J, Hennecke K, Eck M, Weyers H. D, Eickhoff M. Direct steam generation in parabolic troughs: Final results and conclusions of the DISS project. *Energy*. 2004; 29(5-6): 635-644.

[4] Giglio A, Lanzini A, Leone P, García M. M. R, Moya E. Z. Direct steam generation in parabolic-trough collectors: a review about the technology and a thermo-economic analysis of a hybrid system. *Renewable and Sustainable Energy Reviews*. 2017; 74: 453-473.

[5] Dirker J, Juggurnath D, Kaya A, Osowade E. A, Simpson M, Lecompte S, ... & Markides C. N. Thermal energy processes in direct steam generation solar systems: Boiling, condensation and energy storage–A review. *Frontiers in Energy Research*. 2019; 6: 147.

[6] Zhu G, Wendelin T, Wagner M.J, Kutscher C. History, current state, and future of linear Fresnel concentrating solar collectors. *Solar Energy*. 2014; 103: 639-652.

[7] Coventry J, Andraka C. Dish systems for CSP. *Solar Energy*. 2017.

[8] Yang H, Li J, Huang Y, Kwan T.H, Cao J, Pei G. Feasibility research on a hybrid solar tower system using steam and molten salt as heat transfer fluid. *Energy*. 2020.

[9] Dinsenmeyer R. *Étude des écoulements avec changement de phase: application à l'évaporation directe dans les centrales solaires à concentration*. Thèse, Université Grenoble Alpes. 2015.

[10] Pal R. K, Kumar K. R. Investigation of thermo-hydrodynamics, structural stability, and thermal energy storage for direct steam generation in parabolic trough solar collector: A comprehensive review. *Journal of Cleaner Production*. 2021; 311, 127550.

[11] Wojtan L, Ursenbacher T, Thome J. R. Investigation of flow boiling in horizontal tubes: Part I—A new diabatic two-phase flow pattern map. *International journal of heat and mass transfer*. 2005; 48(14): 2955-2969.

[12] Wojtan L. *Experimental and analytical investigation of void fraction and heat transfer during evaporation in horizontal tubes*. Thesis No. 2978, Swiss Federal Institute of Technology, Lausanne. 2004.

[13] Baker O. Design of pipelines for the simultaneous flow of oil and gas. *In Fall meeting of the petroleum branch of AIME*. *OnePetro*. 1953, October.

[14] Taitel Y, Dukler A. E. A model for predicting flow regime transitions in horizontal and near horizontal gas-liquid flow. *AIChE journal*. 1976; 22(1): 47-55.

[15] Hashizume K. Flow pattern and void fraction of refrigerants two-phase flow in a horizontal pipe. Bulletin of JSME 26. 1983; 219: 1597-1602.

[16] Steiner D. Heat transfer to boiling saturated liquids. *VDI-Warmeatlas (VDI Heat Atlas).* 1993.

[17] Kattan, N. *Contribution to the heat transfer analysis of substitute refrigerants in evaporator tubes with smooth or enhanced surfaces*. (Doctoral dissertation, Thesis). 1996.

[18] Kattan N, Thome J, Favrat D. Flow boiling in horizontal tubes: Part 1: Development of a diabatic two-phase flow pattern map. *Journal of heat transfer*. 1998; 120(1): 140-147.

[19] Kattan N, Favrat D, Thome J. R. Flow Boiling in Horizontal Tubes. Part 3; Development of a New Heat Transfer Model Based on Flow Pattern. *Journal of heat transfer*. 1998; 120(1): 156-165.

[20] Thome J. R, Hajal J. E. Two-phase flow pattern map for evaporation in horizontal tubes: latest version. *Heat Transfer Engineering*. 2003; 24(6): 3-10.

[21] Kumar B. N, Reddy K. S. Comparison of two-phase flow correlations for thermo-hydraulic modeling of direct steam generation in a solar parabolic trough collector system. *Journal of Thermal Science and Engineering Applications*. 2018; 10(4), 041005.

[22] Elsafi A.M. On thermo-hydraulic modeling of direct steam generation. *Solar Energy*. 2015; 120: 636-650.

[23] Hoffmann A, Schleider E, Keller L, Leon Alonso J, Pitz-Paal R. Application of a single wire-mesh sensor in a parabolic trough facility with direct steam generation. *Solar Energy*. 2017.

[24] Ursenbacher T, Wojtan L, Thome J.R. Interfacial measurements in stratified types of flow. Part I: New optical measurements technique and dry angle measurements. *International journal of multiphase flow*. 2004; 30: 107-124.

[25] Wojtan L, Ursenbacher T, Thome J.R. Interfacial measurements in stratified types of flow. Part II: Measurements for R-22 and R-410A. *International journal of multiphase flow*. 2004; 30: 125-137.

[26] Rouhani S. Z, Axelsson E. Calculation of void volume fraction in the subcooled and quality boiling regions. *International Journal of Heat and Mass Transfer*. 1970; 13(2): 383-393.

[27] Lockhart R.W, Martinelli R.C. Proposed correlation of data for isothermal two-phase, two-component in pipes. *Chem. Eng. Proce*. 1949;45 (1): 39–48.

[28] Bankoff S.G. A variable density single-fluid model two-phase flow with particular reference to steam-water. *J. Heat Transf*. 1960. 11 (Series B): 265–272.

[29] Thom J.R.S. Prediction of pressure drop during forced circulation boiling of water. *Int. J. Heat Mass Transf*. 1964; 7: 709–724.

[30] Baroczy C.J. A systematic correlation for two-phase pressure drop. *Chem. Eng. Prog. Symp. Ser*. 1965; 62 (44): 232–249.

[31] Chawla J.M. Wa¨rmeu¨bergang and druckfall in waagerechten rohren bei der stro¨mung von verdampfenden ka¨ltemitteln. 523. *VDIForschungsh*, Ch. Lg1-Lg2. 1967.

[32] Chisholm D. Pressure gradients due to friction during the flow of evaporating two-phase mixtures in smooth tubes and channels. *Int. J. Heat Mass Transf*. 1973;16: 347–358.

[33] Gronnerud R. Investigation of liquid hold-up, flow-resistance and heat transfer in circulation type of evaporators, Part iv: two-phase flow resistance in boiling refrigerants. In: Annexe 1972-1, *Bull. de l'Inst. du Froid*. 1979

[34] Friedel L. Improved friction pressure drop correlation for horizontal and vertical two-phase pipe flow. *Proc. of European Two-Phase Flow Group Meet*. 1979. Ispra, Italy.

[35] Olujic Z., 1985. Predicting two-phase flow friction loss in horizontal pipes. *Chem. Eng*. 24 (June), 45–50.

[36] Müller-Steinhagen H, Heck K. A simple friction pressure drop correlation for two-phase flow in pipes. *Chemical Engineering and Processing: Process Intensification*. 1986; 20(6): 297-308.

[37] Hart J, Hamersma P.J, Fortuin J.M.H. Correlations predicting frictional pressure drop and liquid holdup during horizontal gas-liquid pipe flow with a small liquid holdup. *Int. J. Multiphase Flow*. 1989; 15 (6): 947–964.

[38] Ould-Didi M.B, Kattan N, Thome J.R. Prediction of two-phase pressure gradients of refrigerants in horizontal tubes. *Int. J. Refrig*. 2002; 25: 935–947.

[39] Quibén J. M, Thome J. R. Flow pattern based two-phase frictional pressure drop model for horizontal tubes. Part I: Diabatic and adiabatic experimental study. *International Journal of Heat and Fluid Flow*. 2007; 28(5): 1049-1059.

[40] Quibén J. M. *Experimental and analytical study of two-phase pressure drops during evaporation in horizontal tubes*, PhD. Thesis, Swiss Federal Institute of Technology (EPFL), Lausanne, Switzerland. 2005.

[41] Quibén J. M, Thome J. R. Flow pattern based two-phase frictional pressure drop model for horizontal tubes, Part II: New phenomenological model. *International Journal of Heat and Fluid Flow*. 2007; 28(5): 1060-1072.

[42] Yang Z, Peng X.F, Ye P. Numerical and experimental investigation of two phase flow during boiling in coiled tube. *International Journal of Heat and Mass* transfer. 2008; 51: 1003-1016.

[43] Cioncolini A, Santini L, Ricotti M.E. Subcooled and saturated water flow boiling pressure drop in small diameter helical coils at low pressure. *Experimental Thermal and Fluid Science*. 2008; 32: 1301-1312.

[44] Xiao Y, Hu Z, Chen S, Gu H. experimental study of two-phase frictional pressure drop of steam-water in helically coiled tubes with small coil diameters at high pressure. *Applied Thermal Engineering*. 2018; 132: 18-29.

[45] Ju H, Huang Z, Xu Y, Duan B, Yu Y. Hydraulic performance of small bending radius helical coil-pipe. *Journal Nuclear Science Technology*. 2001; 38: 826-831.

[46] Ferraris D.L, Marcel C.P. Two-phase flow frictional pressure drop prediction in helical coiled tubes. *International Journal of Heat and Mass Transfer*. 2020; 162: 120372.

[47] Colombo M, Colombo L, Cammi A, Ricotti M. A scheme of correlation for frictional pressure drop in steam-water two-phase flow in helicoidal tubes. *Chemical Engineering Science*. 2015; 123: 460-473.

[48] Guo L, Feng Z, Chen X. An experimental investigation of the frictional pressure drop of steam-water two-phase flow in helical coils. *International Journal of Heat and Mass Transfer*. 2001; 44: 2601-2610.

[49] Cioncolini A, Santini L. An experimental investigation regarding the laminar to turbulent flow transition in helically coiled pipes. *Exp. Thermal Fluid Science*. 2006; 30.

[50] Hardik B.K, Prabhu S.V. Boiling pressure drop and local heat transfer distribution of helical coils with water at low pressure. *International Journal of Thermal Science*. 2017; 114: 44-63.

[51] Sajadi B, Naserinejad J, Akhavan-Benhabadi M.A, Razi P, Soleimani M. Heat transfer and pressure drop of R1234yf boiling in helically coiled tubes. *Heat Transfer Engineering*. 2021; 43(7): 584-597.

[52] Eck M, Steinmann W. D. Modelling and design of direct solar steam generating collector fields. *Journal of Solar Energy Engineering*. 2005; 127(3): 371-380.

[53] Zarza E. DISS phase II - Final Project Report, EU-Project No. JOR3-CT980277 (2002).

[54] Lobón D. H, Baglietto E, Valenzuela L, Zarza E. Modeling direct steam generation in solar collectors with multiphase CFD. *Applied Energy*. 2014; 113: 1338-1348.

[55] Hoffmann A, Merk B, Hirsch T, Pitz-Paal R. Simulationen zur Thermofluiddynamik in Absorberrohren von Parabolrinnenkraftwerken mit Direktverdampfung mit dem Computercode ATHLET. *Kerntechnik*. 2014; 79(3): 175-185.

[56] Wojtan L, Ursenbacher T, Thome J.R. Investigation of flow boiling in horizontal tubes: Part II – Development of a new heat transfer model for stratified-wavy, dryout and mist flow regimes. *International journal of Heat and Mass transfer*. 2005; 48 (14): 2970-2985.

[57] Valenzuela L, Zarza E, Berenguel M, Camacho E. F. Control concepts for direct steam generation in parabolic troughs. *Solar Energy*. 2005; 78(2): 301-311.

[58] Biencinto M, González L, Valenzuela L. A quasi-dynamic simulation model for direct steam generation in parabolic troughs using TRNSYS. *Applied energy*. 2016; 161: 133-142.

[59] Kandlikar S.G. A general correlation for saturated two-phase flow boiling heat transfer inside horizontal and vertical tubes. *Journal of Heat Transfer*. 1990; 112(1):219-228.

[60] Gungor K.E, Winterton R.H.S. A general correlation for flow boiling in tubes and annuli. *International Chemical Engineering*. 1986; 29(3): 351-358.

[61] Shah M.M. Chart correlation for saturated boiling heat transfer: equation and further study. *ASHRAE Trans.*1982; 88: 185-196.

[62] Hachicha A. A, Rodríguez I, Ghenai C. Thermo-hydraulic analysis and numerical simulation of a parabolic trough solar collector for direct steam generation. *Applied Energy*. 2018; 214: 152-165.

[63] Gnielinski V, New equations for heat and mass transfer in turbulent pipe and channel flow, *Int Chem Eng*. 1976; 16 (2) : 359–363.

[64] Moody L.F, Friction factors for pipe flow, *Trans ASME*. 1944; 66 (8): 671–684.

[65] Odeh S.D, Morrison G.L, Behnia M, Modelling of parabolic trough direct steam generation solar collectors, *Solar Energy*. 1998; 62 (6): 395–406.

[66] Pal R. K, Kumar R. Two-fluid modeling of direct steam generation in the receiver of parabolic trough solar collector with non-uniform heat flux. *Energy*. 2021; 226, 120308.

[67] Malan A, Kumar K. R. Investigation of thermal performance of a large aperture parabolic trough solar collector. *In Proceedings of the 25th National and 3rd International ISHMT-ASTFE Heat and Mass Transfer Conference (IHMTC-2019).* Begel House Inc.

[68] Rojas M.E, de Andres M.C, Gonzalez L. Designing capillary systems to enhance heat transfer in LS3 parabolic trough collectors for direct steam generation (DSG). *Solar Energy*. 2008; 82: 53-60.

[69] Wang P, Liu D.Y, Xu C. Numerical study of heat transfer enhancement in the receiver tube of direct steam generation with parabolic trough by inserting metal foams. *Applied Energy*. 2013; 102: 449-460.

[70] Liu Y, Chen Q, Hu K, Hao J.H. Flow field optimization for the solar parabolic trough receivers in direct steam generation systems by the variational principle. *International Journal of Heat and Mass Transfer*. 2016; 102: 1073-1081.

[71] Kumar B.N, Reddy K.S. Numerical investigations on metal foam inserted solar parabolic trough DSG absorber tube for mitigating thermal gradients and enhancing heat transfer. *Applied Thermal Engineering*. 2020; 178: 115511.

[72] Hosseinalipour S.M, Rostami A, Shahriari G. Numerical study of circumferential temperature difference reduction at the absorber tube of parabolic trough direct steam generation collector by inserting a twisted tape in superheated region. *Case Studies in Thermal Engineering*. 2020; 21: 100720.

[73] Eck M, Steinmann W.D, Rheinländer J. Maximum temperature difference in horizonatal and tilted absorber pipes with direct steam generation. *Energy*. 2004; 29: 665-676.

[74] Demagh Y, Bordja I, Kabar Y, Benmoussa H. A design method of an S-curved parabolic trough collector absorber with a three-dimensional heat flux density distribution. *Solar Energy*. 2015; 122: 873-884.

[75] Demagh Y, Kabar Y, Bordja L, Noui S. The 3D heat flux density distribution on a novel parabolic trough wavy absorber. *In AIP conference proceedings*. 2016. May; 1734 (1): 070004. AIP Publishing LLC.

[76] Bitam E, Demagh Y, Hachicha A, Benmoussa H, Kabar Y. Numerical investigation of a novel sinusoidal tube receiver for parabolic trough technology. *Applied Energy*. 2018; 218: 494-510.

Chapter II : Mathematical model

II.1. Introduction

This chapter provides a brief review of various mathematical models that have been established to understand the boiling flow processes in straight and coiled tubes. In general, due to the large size of solar power plant installations and too long simulation time, the majority of studies in the literature [1-5] use 1D models coupled with empirical or semi-empirical correlations (to estimate void fraction, heat transfer coefficient, and pressure drop) to save time and money. It cannot be adopted in the current study that uses a new shape of solar absorber due to the lack of appropriate correlations that deal with this geometry. Therefore, the only solution is to use 3D simulations.

The most commonly used mathematical models in numerical studies are mainly based on the Eulerian two-fluid method (continuum-dispersed) and the volume of fluid (VOF) method (one fluid with mixture properties) [6].

In this study, the mathematical model based on Eulerian–Eulerian method is presented under the OpenFOAM package, as well as the governing equations and the interphase mass and heat exchange models, and details about different turbulence models.

II.2. Mathematical models review

II.2.1. Straight tubes

Krepper et al. [7] (2007) investigated subcooled boiling flow in vertical straight tubes using the Eulerian method and the RPI (Rensselaer Polytechnic Institute) wall-boiling model [8] in ANSYS CFX. They found an excellent fit of the cross-section void fraction, average fluid temperature, and wall temperature, with reported experimental results for different locations in the tube.

Fontoura et al. [9] (2013) investigated the boiling flow in a horizontal pipe (25m length) of petrochemical pre-heaters using the Eulerian approach in OpenFOAM software. They incorporated a new subroutine to account for phase change. The numerical pressure losses are compared to the Blasius friction factor correlation. They showed excellent agreement, with an error margin of less than 5% for all Reynolds numbers, indicating the validity of the mathematical model.

Braz Filho et al. [10] (2016) used the Eulerian multiphase model in ANSYS Fluent (2013b) to analyse the subcooled boiling flow in DEBORA vertical tube tests. They revealed that the behaviour of boiling flow along the tube is accurate for vapour volume fraction, bulk liquid temperature, and wall temperature.

Abdullah Alali [11] (2018) examined the same problem (DEBORA vertical tube) with OpenFOAM. Their results were similar to earlier research.

As was mentioned in the introduction, the simulations of DSG in solar plants are costly; the DISS test facility solar collectors exceed 500 m. Therefore, the best choice is 1D models using empirical correlations [1-5]. However, to overcome this constraint, particularly for novel correlations required for any optimization, modification, or insertion in the solar absorber, the 3D numerical modelling of the DSG process in a parabolic trough absorber is significantly better (Lobon et al. [12]). However, the rest of the works in the literature simulate only parts of the solar absorber.

Lobon et al. [12] studied DSG in a parabolic trough with actual operating conditions in the DISS test facility. They employed a homogeneous boiling flow model implemented in the commercial STAR-CCM+ software. They used a normalised function to model the variation in heat flux around the absorber. The numerical pressure drop, fluid temperature, and circumferential maximum wall temperature difference coincided quite closely with the DISS measurements (Eck et al. [13] and Zarza et al. [14]).

Dinsenmeyer et al. [15] (2017) investigated the DSG in a Fresnel concentrating solar power plant using the VOF method in Ansys Fluent 14.5. The flow pattern evolution from dispersed bubbles to (intermittent) slug regimes was successfully observed using user-defined functions (UDFs) for accounting for bubble generations and mass transfer.

Pal & Kumar (2021). [16] studied DSG in the parabolic trough for different operating conditions using the Eulerian two-fluid method coupled with the RPI wall-boiling model in Ansys Fluent 2020R1. Taking into account the glass envelope effect and adopting the curve-fitting of noun uniform heat flux from Malan and Kumar [17], they studied the effect of mass velocity on maximum circumferential wall temperature difference and pressure drop.

II.2.2. Coiled tubes

Wu et al. [18] (2007) studied subcooled boiling flow in a horizontal serpentine tube using the Eulerian multiphase method using the Lee model [19] phase change rate coefficient at 0.1 s^{-1}. They were particularly curious about liquid/vapour phase distributions in straight and bend parts. The stratification flow is observed in straight sections, demonstrating the dominant buoyancy force. In the bend parts, the phase distribution is affected by both buoyancy and centrifugal forces, pushing the liquid to the outer wall of the bend and where the vapour remains in the central region. The visual observation for phase distribution for numerical results agreed

well with the experiments in the bend. The numerical outlet void fraction is consistent with the Rouhani-Axelsson correlation [20].

Yang et al. [21] (2008) experimented with boiling flows of R141b in a horizontal transparent serpentine tube and used them to validate numerical simulations performed using the Ansys Fluent code. The numerical model based on the VOF method coupled with Lee's model [19], assuming a 100 s^{-1} for the phase change rate coefficient, had well predicted the two-phase distribution observed in the experiments.

Sun et al. [22] (2017) studied numerically boiling flows in a vertically coiled tube, assuming a two-phase Eulerian model using Ansys Fluent. The primary purpose is to test the inner tube diameter and heat flux effects on the heat transfer coefficient and temperature distribution. At first, the model is validated quantitatively and qualitatively. Murai et al. [23] (2005) experiments for air-water flow in a vertical transparent coiled tube were used to validate the numerical simulations qualitatively. A good agreement is obtained, showing the dominance of centrifugal force for phase distribution. The experimental data in the paper of Hwang et al. [24] (2014) is simulated for quantitative validation. The results for the heat transfer coefficient showed the same trend as in the experiments, with a slight difference for different vapour qualities. Another quantitative validation of the wall temperature difference is demonstrated in the experiment of Chung et al. [25] (2014). The results displayed that the highest wall temperature was at the inside of the coiled tube, and the minimum was at the outside. Generally, the temperature distribution in cross-section for different sides (top, bottom, inside, and outside) is similar for both numerical and experimental results.

Abdous et al. [26] (2018) studied the subcooled and saturated flow boiling in a vertically coiled tube with the Two-phase Eulerian method using the model of Lee [19]. The phase change rate coefficient is set at 0.1 s^{-1}. In the validation part, they used the experimental work of Cioncolini et al. [27] (2008). A good agreement between the numerical and experimental results for pressure loss [27] was found. The correlation of Woldesemayat and Ghajar [28] is successfully used to validate the numerical void fraction of Abdous et al. [26] (2018). Furthermore, it is observed that gravity and centrifugal force are the main dominant forces in the phase distribution.

II.3. Eulerian-Eulerian approach

Using the OpenFOAM +1906 package, the Eulerian two-fluid approach examines boiling flow inside straight and coiled horizontal tubes. The conservation equations of mass, momentum, and energy are calculated independently for each phase, as shown below.

The equation for mass conservation,

$$\frac{\partial}{\partial t}(\alpha_k \rho_k) + \nabla \cdot \left(\alpha_k \rho_k \vec{U}_k\right) = \Gamma_{ki} - \Gamma_{ik} \tag{II. 1}$$

Γ_{ki} and Γ_{ik} are the mass transfers because of the evaporation/condensation from phase k to phase i or the opposite.

The equation for momentum conservation,

$$\frac{\partial}{\partial t}\left(\alpha_k \rho_k \vec{U}_k\right) + \nabla \cdot \left(\alpha_k \rho_k \vec{U}_k \vec{U}_k\right) = -\alpha_k \nabla P + \nabla \cdot \left(\alpha_k \left(\tau_k + \tau_k^{turb}\right)\right) + \alpha_k \rho_k \vec{g} + \vec{F}_k + \Gamma_{ki} \vec{U}_i - \Gamma_{ik} \vec{U}_k \tag{II. 2}$$

$\vec{F}_k$ being a source term described in the subsection (momentum interphase model).

The equation for energy conservation,

$$\frac{\partial}{\partial t}(\alpha_k \rho_k H_k) + \nabla \cdot \left(\alpha_k \rho_k H_k \vec{U}_k\right) = \nabla \cdot \left(\alpha_k \left(q_k + q_k^{turb}\right)\right) + \alpha_k \frac{Dp_k}{Dt} + \Gamma_{ki} H_i - \Gamma_{ik} H_k + \Phi_k \tag{II. 3}$$

q_k, q_k^{turb} and Φ_k are the heat flux conduction, turbulent heat flux conduction, and wall heat source for phase k, respectively.

Interphase transfers such as momentum, heat, mass, and turbulence appear as source terms. They are described as follows:

II.3.1. Momentum interphase model

$\left(\vec{F}_k\right)$ is the momentum exchange source term. It is expressed as:

$$\vec{F}_k = \vec{F}_D + \vec{F}_L + \vec{F}_{TD} + \vec{F}_{WL} + \vec{F}_{VM} \tag{II. 4}$$

The forces on the right-hand side of equation (II.4) represent the interphase drag, lift, turbulent dispersion, wall lubrication, and virtual mass forces, respectively. They are defined as:

II.3.1.1. Interphase drag force

The interfacial drag force for bubbly and mist flow is described by Ishii & Zuber [29]:

$$\vec{F}_D = -\frac{3}{4}\frac{C_D}{d_B}\rho_c \alpha_d \left|\vec{U}_d - \vec{U}_c\right|\left(\vec{U}_d - \vec{U}_c\right) \tag{II. 5}$$

The subscript d refers to the dispersed phase, whereas c refers to the continuous phase.

II.3.1.2. Interphase lift force

$(\vec{F}_L)$ acts perpendicular to the flow stream. It is caused by interactions between the bubble and the velocity profile, as well as vortex formation in the liquid phase. When the Tomiyama et al. [30] model is used, it is represented as follows:

$$\vec{F}_L = -C_L \rho_l (\vec{U}_v - \vec{U}_l) \times (\nabla \times \vec{U}_l) \quad \text{(II. 6)}$$

C_L is the lift coefficient given by the Tomiyama correlation [30].

II.3.1.3. Turbulent dispersion force

$(\vec{F}_{TD})$ represents the turbulent diffusion of the vapour phase (small bubbles). The turbulent dispersion is given by De Bertodano [31]:

$$\vec{F}_{TD} = -C_{TD} \rho_l k_l \nabla \alpha_v \quad \text{(II. 7)}$$

Where k_l is the liquid turbulent kinetic energy, and C_{TD} is the turbulent dispersion coefficient.

II.3.1.4. Wall lubrication force

$(\vec{F}_{WL})$ acts perpendicular to the wall, driving bubbles away from it and stopping them from assembling nearby due to the dynamic pressure difference. It is given by Antal et al. [32]

$$\vec{F}_{WL} = -\frac{\alpha_v \rho_l (\vec{U}_v - \vec{U}_l)^2}{d_B} \cdot \max\left(C_{w1} + C_{w2} \frac{d_B}{y_w}, 0\right) \vec{n} \quad \text{(II. 8)}$$

y_w refers to the distance from the wall, and $\vec{n}$ is the normal vector to the wall. The non-dimensional coefficients C_{w1} and C_{w2} are set to (-0.01) and (0.05), respectively.

II.3.1.5. Virtual mass force

$(\vec{F}_{VM})$ represents the virtual mass force. The relative acceleration of the vapour and liquid phases causes it. In this study, it is calculated using Zuber's [33] formula:

$$\vec{F}_{VM} = C_{VM} \alpha_d \rho_c \left[\left(\frac{\partial \vec{U}_d}{\partial t} + \vec{U}_d \cdot \nabla \vec{U}_d\right) - \left(\frac{\partial \vec{U}_c}{\partial t} + \vec{U}_c \cdot \nabla \vec{U}_c\right)\right] \quad \text{(II. 9)}$$

C_{VM} is the virtual mass coefficient set (0.5).

II.3.2. Interphase mass and heat transfer models

- The mass transfer rate (Γ_{lv}) due to phase change by condensation is calculated as follows:

$$\Gamma_{lv} = \frac{h_{ki} A_i (T_{sat} - T_l)}{H_{lv}} \quad \text{(II. 10)}$$

- The mass transfer rate due to phase change by evaporation Γ_{vl} is calculated as follows :

$$\Gamma_{vl} = \frac{h_{ki} A_i (T_{sat} - T_v)}{H_{lv}} \quad \text{(II. 11)}$$

(H_{lv}) denotes the latent heat, and (h_{ki}) is the interfacial heat transfer coefficient. From Ranz and Marshall (1952) [34], it is calculated as follows:

$$h_{ki} = \frac{\lambda_k}{d_B} Nu = \frac{\lambda_k}{d_B} (2.0 + 0.6 \mathrm{Re}^{0.5} \mathrm{Pr}^{0.33}) \quad \text{(II. 12)}$$

(d_B) is the bubble mean Sauter diameter, and (λ_k) is the thermal conductivity of phase (k). (A_i) is the interphase contact area, defined as:

$$A_i = \frac{6}{d_B} \alpha_v \quad \text{(II. 13)}$$

Kurul and Podowski [8] express the bubble mean Sauter diameter as linearly variable with subcooled temperature, and it is corrected by Anglart and Nylund (1997) [35] to be calculated as:

$$d_B = \frac{d_{B,1}(T_{sub} - T_{sub,2}) + d_{B,2}(T_{sub} - T_{sub,1})}{T_{sub,2} - T_{sub,1}} \quad \text{(II. 14)}$$

Where, $d_{B,1} = 0.1\ mm$ at $T_{sub,1} = 13.5\ K$ and $d_{B,2} = 2\ mm$ at $T_{sub,2} = 5\ K$.

II.3.3. Wall boiling model (RPI)

Kurul & Podowski [8] describe the overall wall heat flux (q_w) in subcooled flow as the sum of the convective (q_l), quenching (q_q), and evaporative (q_e) heat fluxes:

$$q_w = q_l + q_q + q_e \quad \text{(II. 15)}$$

Every heated surface unit is divided into two parts: the nucleating bubbles affect one part (A_Q), while the single-phase convection influences the other part (A_C). Therefore,

$$A_Q + A_C = 1 \quad \text{(II. 16)}$$

II.3.3.1. Single-phase liquid convection heat flux

The liquid convection heat flux (q_l) through the wall surface part (A_C) is:

$$q_l = h_l A_C (T_w - T_l) \quad \text{(II. 17)}$$

Where (T_w) denotes the wall temperature, and (h_l) is the liquid heat transfer coefficient.

II.3.3.2. Quenching heat flux

Mikic & Rohsenow [36] (1969) defined quenching heat transfer (q_q) as the process that occurs between the formation of two successive bubbles in the same site, they consider it as a

transient conduction between the wall and the the liquid that replaces the detached bubble, and it is expressed as:

$$q_q = h_q A_Q (T_w - T_l) \quad \text{(II. 18)}$$

(A_Q), the fraction of the unit wall area influenced by vapour bubbles, is given by:

$$A_Q = \min\left[1, N_a \pi d_{dep}^2\right] \quad \text{(II. 19)}$$

The bubble departure diameter (d_{dep}) is obtained by Tolubinski & Kostanchuk [37] as:

$$d_{dep} = \min\left\{0.6[mm]\exp\left(\frac{-\Delta\left(T_{sat} - (T_l)\right)}{45K}\right), 1.4[mm]\right\} \quad \text{(II. 20)}$$

The nucleation site density is estimated by Lemmert & Chawla [38] formula as:

$$N_a = [210(T_w - T_l)]^{1.805} \quad \text{(II. 21)}$$

The Quenching heat transfer coefficient (h_q) is given as:

$$h_q = \frac{2}{\sqrt{\pi}} f \sqrt{t_{wait} \lambda_l \rho_l C p_l} \quad \text{(II. 22)}$$

(f), the bubble departure frequency. It is calculated by Cole [39]:

$$f = \sqrt{\frac{4g(\rho_l - \rho_v)}{3 d_{dep} \rho_l}} \quad \text{(II. 23)}$$

(t_{wait}), the waiting time between the departure of the first bubble and the appearance of the second one at the same nucleation site, it is calculated as follows:

$$t_{wait} = \frac{0.8}{f} \quad \text{(II. 24)}$$

II.3.3.3. Evaporative heat flux

The evaporative heat flux (q_e) is the evaporation mass flux of the subcooled liquid at the unit wall area, and it is given as follow:

$$q_e = \rho_v \frac{\pi}{6} d_{dep}^3 f N_a H_{lv} \quad \text{(II. 25)}$$

Therefore, the mass transfer rate due to the evaporation rate is expressed as:

$$\Gamma_{vl} = \rho_v \frac{\pi}{6} d_{dep}^3 f \cdot N_a \quad \text{(II. 26)}$$

II.3.4. Turbulence modelling

In OpenFOAM, only a few turbulence models are available for the Eulerian multiphase-derived solvers, as the Eulerian-Eulerian approach treats the phases as continuous or dispersed. Usually, the dispersed phase generates additional eddies in the continuous phase. The best

solution to account for them is to add source terms to the standard turbulence model equations. The available turbulence models are Lahey KEpsilon [40], Mixture KEpsilon [41], and Sato KOmega SST [42, 43] models.

II.3.4.1. Lahey KEpsilon model

The liquid is considered the continuous phase in the boiling flow, whereas the bubble represents the dispersed phase. According to Lahey [40] (2005), the standard $(k-\varepsilon)$ model is used for the liquid phase, with the source term (S_{BIT}) introduced to account for the dispersed bubbles effect in turbulence.

The modified $(k-\varepsilon)$ model equations are presented as follows:

The equation for turbulent dissipation:

$$\frac{\partial(\alpha_l\rho_l\varepsilon_l)}{\partial t}+\nabla\cdot\left(\alpha_l\rho_l\varepsilon_l\vec{U}_l\right)-\nabla^2\left(\alpha_l\varepsilon\left(\mu+\frac{\mu_t}{\sigma_\varepsilon}\right)\right)$$
$$=\alpha_l\rho_l C_2\varepsilon_l-C_1\frac{\alpha_l\rho_l\varepsilon_l}{k}G-\left(\left(\frac{2}{3}C_1+C_2\right)\alpha_l\rho_l\varepsilon_l\nabla\cdot\vec{U}_l\right)-\frac{C_2\alpha_l\rho_l\varepsilon_l^2}{k_l}$$
$$+S_{BIT} \qquad \text{(II. 27)}$$

For phase inversion $\alpha^I=0.3$.

The source term (S_{BIT}) is calculated:

$$S_{BIT}=\frac{\alpha_l\rho_l C_2\varepsilon_l G_{bubble}}{k}+\max(\alpha^I-\alpha_l,0)\min\left(\frac{\varepsilon_v}{k_v},\frac{1}{\Delta t}\right)\rho_l(\varepsilon_v-\varepsilon_l) \qquad \text{(II. 28)}$$

Where

$$G_{bubble}=\frac{C_P\alpha_v}{d_B}\left|\vec{U}_r\right|^{5/3}\left(C_d\left|\vec{U}_r\right|\right)^{4/3} \qquad \text{(II. 29)}$$

The equation for turbulent kinetic energy:

$$\frac{\partial(\alpha_l\rho_l k_l)}{\partial t}+\nabla\cdot\left(\alpha_l\rho_l k_l\vec{U}_l\right)-\nabla^2\left(\alpha_l\left(\mu+\frac{\mu_t}{\sigma_k}\right)\right)$$
$$=\alpha_l\mu_t G-\frac{2}{3}\rho\varepsilon\nabla\cdot\vec{U}-\alpha_l\rho_l\varepsilon_l+S_{BIT} \qquad \text{(II. 30)}$$

The source term (S_{BIT}) is given by:

$$S_{BIT}=\alpha_l\rho_l G_{bubble}+\max(\alpha^I-\alpha_l,0)\min\left(\frac{\varepsilon_v}{k_v},\frac{1}{\Delta t}\right)\rho_l(\varepsilon_v-\varepsilon_l)(k_v-k_l) \qquad \text{(II. 31)}$$

The other coefficients are the same as in the standard $(k-\varepsilon)$ model presented in Table II.1.

Table II.1. Defaults coefficients of the standard $(k-\varepsilon)$ model.

Coefficients	C_μ	C_1	C_2	σ_l	σ_ε
Default value	0.09	1.44	1.92	1.0	1.33

As the vapour quality increases, the vapour phase is no longer considered to fluctuate in the liquid phase, requiring an independent turbulence model. For the vapour phase, a supplementary model based on the standard $(k-\varepsilon)$ model is used, which allows phase inversion.

The effective turbulent viscosity in the vapour phase is expressed as:

$$\nu_t^{eff} = \frac{1-\min\left(1, e^{\min\left(\frac{\phi_l}{\phi_v}, 50\right)}\right)}{1+\min\left(1, e^{\min\left(\frac{\phi_l}{\phi_v}, 50\right)}\right)} \quad \text{(II. 32)}$$

Where,

$$\phi_l = \frac{k_l}{\varepsilon_l} \quad \text{(II. 33)}$$

and,

$$\phi_v = d_B^2 \frac{\rho_v + C_{VM}\rho_l}{18\rho_l \nu_l} \quad \text{(II. 34)}$$

II.3.4.2. Mixture KEpsilon model

Behzadi et al. [41] proposed another turbulence model developed for a high void fraction that employs a mixture of values for (k) and (ε) rather than changing between models when phase-inversion happens. Mass averaging of $k, \varepsilon, \phi, \rho$ and ν are generated for mixture single phase $(k-\varepsilon)$ model. The turbulence response coefficient is used to calculate the turbulence properties of each phase, it is calculated as:

$$C_{t2} = \sqrt{1+(C_{t0}-1)e^{\left(-\alpha_d^f\right)}} \quad \text{(II. 35)}$$

Where,

$$C_{t0} = \frac{3+\beta}{1+\beta+2\frac{\rho_v}{\rho_l}} \quad \text{(II. 36)}$$

$$\beta = \frac{6C_\mu C_d k_l}{4\sqrt{\frac{3}{2}\rho_l \varepsilon_l}} \quad \text{(II. 37)}$$

$$\alpha_d^f = \alpha_v\left(180 + \alpha_v(-4.71 \times 10^3 + 4.26 \times 10^4 \alpha_v)\right) \quad \text{(II. 38)}$$

For liquid phase, the mass weighting is calculated as follows:

$$k_l = k_m \frac{\rho_m}{\alpha_l \rho_l + \alpha_v \rho_v C_{t2}}; \qquad \varepsilon_l = \varepsilon_m \frac{\rho_m}{\alpha_l \rho_l + \alpha_v \rho_v C_{t2}} \quad \text{(II. 39)}$$

$$\nu_{t,l} = C_\mu \frac{k_l^2}{\varepsilon_l} \quad \text{(II. 40)}$$

Then, for the gas phase:

$$k_v = k_m C_{t2}; \qquad \varepsilon_v = \varepsilon_m C_{t2} \quad \text{(II. 41)}$$

$$\nu_{t,v} = \nu_{t,l} \frac{C_{t2} \nu_l}{\nu_v} \quad \text{(II. 42)}$$

II.3.4.3. Sato K-omega SST model

The advantage of $k - \omega\ SST$ turbulence model (based on Menter and Esch (2001) [42]) is its reliability on curved boundary flows. It switches $k - \omega$ turbulence model near the wall and the standard $k - \varepsilon$ model in the free flow region, as both models have two transport equations. To account for eddies created by dispersed bubbles in the continuous liquid phase, Sato et al. [43] added a term of induced bubble turbulence in the viscosity equation [see equations (II.43 and II.44)].

For turbulent kinetic energy:

$$\frac{\partial(\alpha_l \rho_l k_l)}{\partial t} + \nabla \cdot \left(\alpha_l \rho_l k_l \vec{U}_l\right) = \nabla \cdot (\alpha_l(\mu + \mu_t \alpha_k)\nabla k) + \alpha_l(P - \beta^* \rho \omega k) + S^k \quad \text{(II. 43)}$$

For dissipation rate of turbulent kinetic energy:

$$\frac{\partial(\alpha_l \rho_l \omega_l)}{\partial t} + \nabla \cdot \left(\alpha_l \rho_l \omega_l \vec{U}_l\right) = \nabla \cdot (\alpha_l(\mu + \mu_t \alpha_\omega)\nabla \omega) + \alpha_l \left(C_{\omega P} \frac{\rho P}{\mu} - C_{\omega D} \rho \omega^2\right) + 2\alpha_l \rho_l (1 - F_1) \alpha_{\omega 2} \frac{\nabla k \cdot \nabla \omega}{\omega} + S^\omega \quad \text{(II. 44)}$$

The turbulent coefficients α_ω, α_k, $C_{\omega D}$, and $C_{\omega P}$ are calculated according to weighted average [look Table II.2]:

$$\gamma = \gamma_1 F_1 + \gamma_2 (1 - F_1) \quad \text{(II. 45)}$$

Table II.2. Turbulence coefficients for SST K-Omega model.

	β^*	$C_{\omega P}$	$C_{\omega D}$	$\alpha_k = \frac{1}{\sigma_k}$	$\alpha_\omega = \frac{1}{\sigma_\omega}$
$k-\omega$ (index 1)	0.09	0.5532	0.075	0.85034	0.5
$k-\varepsilon$ (index 2)	0.09	0.4403	0.0828	1.0	0.85616

F_1 denotes the blending function which assume a value one for $k-\omega$ model and zero for $k-\varepsilon$ model, it's defined as:

$$F_1 = \tanh\left[\left(\min\left(\max\left(\frac{\sqrt{k}}{\beta^*\omega y}, \frac{500\mu}{\rho\omega y^2}\right), \frac{4\alpha_{\omega 2}\rho k}{y^2 \max\left(2\alpha_{\omega 2}\rho\frac{\nabla k\cdot\nabla\omega}{\omega}, 10^{-10}\right)}\right)\right)^4\right] \quad \text{(II. 46)}$$

y is the normal distance to the wall.

P is the production limiter.

$$P = \min\left(2\mu_t \mathrm{D}:\nabla\vec{U}, 10\beta^*\rho\omega k\right) \quad \text{(II. 47)}$$

$$\mu_t = \frac{\alpha_1\rho k}{\max(\alpha_1\omega, F_2 S)} + \left(1-e^{-y^+/16}\right)^2 0.6 d_B \alpha_v\left(\vec{U}_v - \vec{U}_l\right) \quad \text{(II. 48)}$$

Where: $\alpha_1 = 0.31$

$$F_2 = \tanh\left[\left(\max\left(\frac{2\sqrt{k}}{\beta^*\omega y}, \frac{500\mu}{\rho\omega y^2}\right)\right)^2\right] \quad \text{(II. 49)}$$

The source terms are calculated:

$$S^k = \vec{F}_D\cdot\left(\vec{U}_v - \vec{U}_l\right) \quad \text{(II. 50)}$$

$$s^\omega = \frac{1}{\beta^* k}S^\varepsilon - \frac{\omega}{k}S^k \quad \text{(II. 51)}$$

$$S^\varepsilon = \frac{S^k\sqrt{k}}{d_B} \quad \text{(II. 52)}$$

For vapour phase, the standard $k-\omega$ SST is used.

II.4. Conclusion

The literature shows that the Eulerian mathematical method with the RPI wall boiling model, supplemented with additional models to account for interphase transfers, is the most robust model and requires no coefficient adjustment, unlike the VOF method. In the latter, the coefficient (r) of the Lee model [19] must be adjusted to accurately predict the rate of phase change, such as Wu et al. [18] who used a value of $r=0.1s^{-1}$, while Yang et al. [21] used $r=100s^{-1}$). Furthermore, VOF result accuracy requires a finer mesh than the Eulerian technique, which yields good accuracy even with a coarser mesh, as suggested by Guerrero et al. [6].

This study suggests using the two-fluid Eulerian method with the RPI wall-boiling model to study the DSG in the DISS solar power plant.

First, the model will be validated for boiling flow in straight and coiled horizontal tubes at a laboratory scale, as detailed below:

For horizontal straight tubes: the same geometry properties and operating conditions of the test section tube as Wojtan et al. [44] will be used. The numerical results of the void fraction will be compared to the Rouhani-Axelsson correlation [20]. In addition, the numerical results of the frictional pressure drop will be compared to the experimental results of Quibén and Thome [45], as they adopted the same experimental prototype as Wojtan et al. [44].

For horizontal coiled tubes: using the boiling experiment in the horizontal helical tube of Sajadi et al. [46] to validate the simulations by performing a comparative analysis of frictional pressure drop.

Secondly, the model will be used to predict the thermal-hydraulic behaviour of the DSG in the conventional straight absorber of the DISS solar installation (Spain). Finally, the model will be used to study the scenario where the conventional straight absorber would be replaced by the S-curved absorber recently proposed by Demagh et al. [47] and perform a comparative analysis.

References

[1] Eck M, Steinmann W. D. Modelling and design of direct solar steam generating collector fields. *Journal of Solar Energy Engineering*. 2005; 127(3): 371-380.

[2] Hachicha A. A, Rodríguez I, Ghenai C. Thermo-hydraulic analysis and numerical simulation of a parabolic trough solar collector for direct steam generation. *Applied Energy*. 2018; 214: 152-165.

[3] Kumar B. N, Reddy K. S. Comparison of two-phase flow correlations for thermo-hydraulic modeling of direct steam generation in a solar parabolic trough collector system. *Journal of Thermal Science and Engineering Applications*. 2018; 10(4), 041005.

[4] Elsafi A.M. On thermo-hydraulic modeling of direct steam generation. *Solar Energy*. 2015; 120: 636-650.

[5] Biencinto M, González L, Valenzuela L. A quasi-dynamic simulation model for direct steam generation in parabolic troughs using TRNSYS. *Applied energy*. 2016; 161: 133-142.

[6] Guerrero E, Muñoz F, Ratkovich N. Comparison between eulerian and vof models for two-phase flow assessment in vertical pipes. CT&F-Ciencia, *Tecnología y Futuro*. 2017; 7(1): 73-84.

[7] Krepper E, Končar B, Egorov Y. CFD modelling of subcooled boiling—concept, validation and application to fuel assembly design. *Nuclear engineering and design*. 2007; 237(7): 716-731.

[8] Kurul N, Podowski M. Z. On the modeling of multidimensional effects in boiling channels. ANS. *Proc. National Heat Transfer Con*. 1991. Minneapolis, Minnesota, USA.

[9] Fontoura D. V. R, Matos E. M, Nunhez J. R. A three-dimensional two-phase flow model with phase change inside a tube of petrochemical pre-heaters. *Fuel*. 2013; 110: 196-203.

[10] Braz Filho F. A, Ribeiro G. B, Caldeira A. D. Prediction of subcooled flow boiling characteristics using two-fluid Eulerian CFD model. *Nuclear engineering and design*. 2016; 308: 30-37.

[11] Alali A, Schöffel P. J, Herb J, Macian R. Numerical investigations on the coupling of the one-group interfacial area transport equation and subcooled boiling models for nuclear safety applications. *Annals of Nuclear Energy*. 2018; 120: 155-168.

[12] Lobón D. H, Baglietto E, Valenzuela L, Zarza E. Modeling direct steam generation in solar collectors with multiphase CFD. *Applied Energy*. 2014; 113: 1338-1348.

[13] Eck M, Steinmann W. D. Modelling and design of direct solar steam generating collector fields. *International Solar Energy Conference (ISEC2004)*. July 11-14, 2004. Portland, Oregon USA.

[14] Zarza E. DISS phase II - Final Project Report, EU-Project No. JOR3-CT980277 (2002).

[15] Dinsenmeyer R, Fourmigué J. F, Caney N, Marty P. Volume of fluid approach of boiling flows in concentrated solar plants. *International Journal of Heat and Fluid Flow*. 2017; 65: 177-191.

[16] Pal R. K, Kumar R. Two-fluid modeling of direct steam generation in the receiver of parabolic trough solar collector with non-uniform heat flux. *Energy*. 2021; 226, 120308.

[17] Malan A, Kumar K. R. Investigation of thermal performance of a large aperture parabolic trough solar collector. *In Proceedings of the 25th National and 3rd International ISHMT-ASTFE Heat and Mass Transfer Conference (IHMTC-2019).* Begel House Inc.

[18] Wu H. L, Peng X. F, Ye P, Gong Y. E. Simulation of refrigerant flow boiling in serpentine tubes. *International Journal of Heat and Mass Transfer*. 2007; 50(5-6): 1186-1195.

[19] Lee W. H. Pressure iteration scheme for two-phase flow modeling. *in multiphase transport: fundamentals, reactor safety, applications*. 1980; 407-432.

[20] Rouhani S. Z, Axelsson E. Calculation of void volume fraction in the subcooled and quality boiling regions. *International Journal of Heat and Mass Transfer*. 1970; 13(2): 383-393.

[21] Yang Z, Peng X.F, Ye P. Numerical and experimental investigation of two phase flow during boiling in coiled tube. *International journal of Heat and Mass transfer*. 2008; 51: 1003-1016.

[22] Sun B , Yu X , Liu S , Shi J, Yang L, Zhang G, Zhang P. Non-uniform wall temperature distribution of nucleate boiling heat transfer in helically coiled tubes. *Nuclear Engineering and Design*. 2018; 330: 356-367.

[23] Murai Y, Oiwa H, Sasaki T, Kondou K, Yoshikawa S, Yamamoto F. Backlight imaging tomography for gas liquid two-phase flow in a helically coiled tube. *Meas. Sci. Technol*. 2005; 16 (7): 1459–1468.

[24] Hwang K.W, Dong E.K, Yang K.H, Jin M.K, Kim M.H, Park H.S. Experimental study of flow boiling heat transfer and dryout characteristics at low mass flux in helically-coiled tubes. *Nucl. Eng. Des*. 2014; 273: 529–541.

[25] Chung Y.J, Bae K.H, Kim K.K, Lee W.J. Boiling heat transfer and dryout in helically coiled tubes under different pressure conditions. *Ann. Nucl. Energy*. 2014; 71: 298–303.

[26] Abdous M. A, Holagh S.G, Saffari H. Numerical Investigation of Flow Boiling Heat Transfer in Helically Coiled Tube under Constant Heat Flux. *Thermal Science and Engineering*. 2018; 1 : 1-18.

[27] Cioncolini A, Santini L, Ricotti ME. Subcooled and saturated water flow boiling pressure drop in small diameter helical coils at low pressure. *Exp Therm Fluid Sci* . 2008; 32 :1301–1312.

[28] Woldesemayat M.A, Ghajar A.J. Comparison of void fraction correlations for different flow patterns in horizontal and upward inclined pipes, *International Journal of Multiphase Flow*. 2007; 33: 347–370.

[29] Ishii M, Zuber N. Drag coefficient and relative velocity in bubbly, droplet or particulate flows. *AIChE journal*. 1979; 25(5): 843-855.

[30] Tomiyama A, Tamai H, Zun I, Hosokawa S. Transverse migration of single bubbles in simple shear flows. *Chemical Engineering Science*. 2002; 57(11): 1849-1858.

[31] De Bertodano M. A. L. *Turbulent bubbly two-phase flow in a triangular duct*. Rensselaer Polytechnic Institute. 1992.

[32] Antal S. P, Lahey Jr R. T, Flaherty J. E. Analysis of phase distribution in fully developed laminar bubbly two-phase flow. *International journal of multiphase flow*. 1991; 17(5): 635-652.

[33] Zuber N. On the dispersed two-phase flow in the laminar flow regime. *Chemical Engineering Science*. 1964; 19(11): 897-917.

[34] Ranz W. E, Marshall W. R. Evaporation from drops, Parts I & II. *Chem Eng Prog*. 1952; 48: 141-146.

[35] Anglart H, Nylund O. CFD application to prediction of void distribution in two-phase bubbly flows in rod bundles. *Nuclear Engineering and Design*. 1996; 163(1-2): 81-98.

[36] Mikic B, Rohsenow W. A new correlation of pool-boiling data including the effect of heating surface characteristics. *J. Heat Transfer*. 1969; 91 (2): 245–250.

[37] Tolubinsky V. I, Kostanchuk D. M. Vapour bubbles growth rate and heat transfer intensity at subcooled water boiling. *In International Heat Transfer Conference 4*. 1970; 23. Begel House Inc.

[38] Lemmert M, Chawla J. Influence of flow velocity on surface boiling heat transfer coefficient. *Heat Transfer Boiling*. 1977; 237-247.

[39] Cole R. A photographic study of pool boiling in the region of the critical heat flux. *AIChE Journal*. 1960; 6(4): 533-538.

[40] Lahey R. T. The simulation of multidimensional multiphase flows. *Nuclear Engineering and Design*. 2005; 235(10):1043-1060.

[41] Behzadi A, Issa R. I, Rusche H. Modelling of dispersed bubble and droplet flow at high phase fractions. *Chemical Engineering Science*. 2004; 59(4): 759-770.

[42] Menter F, Esch T. Elements of Industrial Heat Transfer Prediction. *16th Brazilian Congress of Mechanical Engineering (COBEM)*, Nov. 2001

[43] Sato Y, Sadatomi M. Momentum and heat transfer in two-phase bubble flow - I, Theory. *International Journal of Multiphase Flow*. 1981; 7: 167-177.

[44] Wojtan L, Ursenbacher T, Thome J. R. Investigation of flow boiling in horizontal tubes: Part I—A new diabatic two-phase flow pattern map. *International journal of heat and mass transfer*. 2005; 48(14): 2955-2969.

[45] Quibén J. M, Thome J. R. Flow pattern based two-phase frictional pressure drop model for horizontal tubes. Part I: Diabatic and adiabatic experimental study. *International Journal of Heat and Fluid Flow*. 2007; 28(5): 1049-1059.

[46] Sajadi B, Naserinejad J, Akhavan-Benhabadi M.A, Razi P, Soleimani M. Heat transfer and pressure drop of R1234yf boiling in helically coiled tubes. *Heat Transfer Engineering*. 2021; 43(7): 584-597.

[47] Demagh Y, Bordja I, Kabar Y, Benmoussa H. A design method of an S-curved parabolic trough collector absorber with a three-dimensional heat flux density distribution. *Solar Energy*. 2015; 122: 873-884.

Chapter III : Mathematical model validation

III.1. Introduction

This chapter includes validating the mathematical model established in the previous chapter by comparison with experimental data for horizontal straight and coiled tubes from the literature. Through this validation, valuable information can be gathered about the reliability of the mathematical model in predicting phase change phenomena and properties at the laboratory scale (for different operating conditions and steam quality) and what will guide us later in its use in commercial DSG configurations.

The experimental work of Wojtan et al. [1] for boiling flow in the horizontal tube will be studied numerically for different wall heat fluxes and mass velocities to determine the accuracy of the chosen mathematical models. The second part concerns the study of boiling flow in horizontal coiled tubes by Sajadi et al. [2], where particular attention is paid to validating the frictional pressure drop for different vapour qualities. Horizontal coiled tubes are chosen in this validation due to the lack of experimental or numerical studies of boiling flow in longitudinally curved tubes (S-shaped as in the new solar absorber) in the literature. Thus, validating the mathematical model with a horizontal coiled tube will be a promising solution to emphasize the accuracy of DSG results in the new solar absorber.

Only a few turbulence models are available for the Eulerian–Eulerian method under the OpenFOAM package. Different turbulence models will be adopted in the validation part to determine their reliability and choose the accurate ones for the DSG part.

III.2. Validation of the mathematical model

III.2.1. Horizontal tube

Wojtan et al. [1] and Wojtan [3] employed a visualisation technique to measure the cross-sectional void fraction in an externally heated horizontal tube. The laboratory-scale test facility shown in Figure III.1 has an inner diameter of 13.84 mm, an outer diameter of 15.87 mm, and a total straight length of 2.026 m. Table III.1 lists the four experimental cases that will be examined in this study.

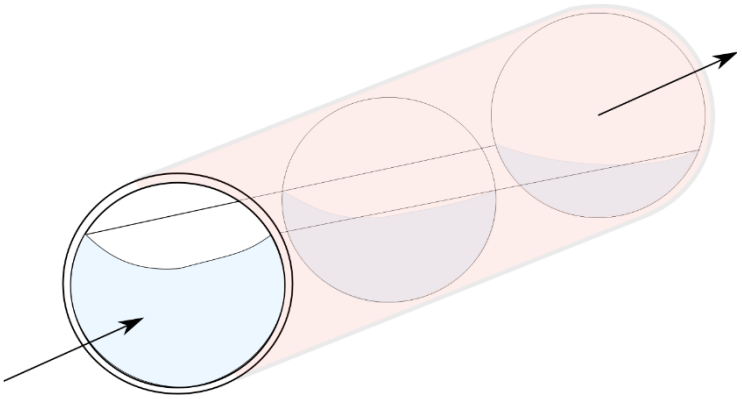

Figure III.1. Schematic of the experimental test section (by Wojtan et al. [1]).

Table III.1. The experimental conditions [3, 4, 5].

Cases	Fluid type	Mass velocity $G\ (kg/m^2\ s)$	Wall heat flux $q(W/m^2)$	Inlet vapor quality
1	R22	300	17.5	0
2	R22	150	7.5	0
3	R22	150	37.5	0
4	R22	150	17.5	0

III.2.1.1. Mesh independence tests

Salome Meca (2017) (a free source) created the structured meshing of hexahedral elements depicted in Figure III.2. The simulation time was reduced, assuming a symmetry boundary condition.

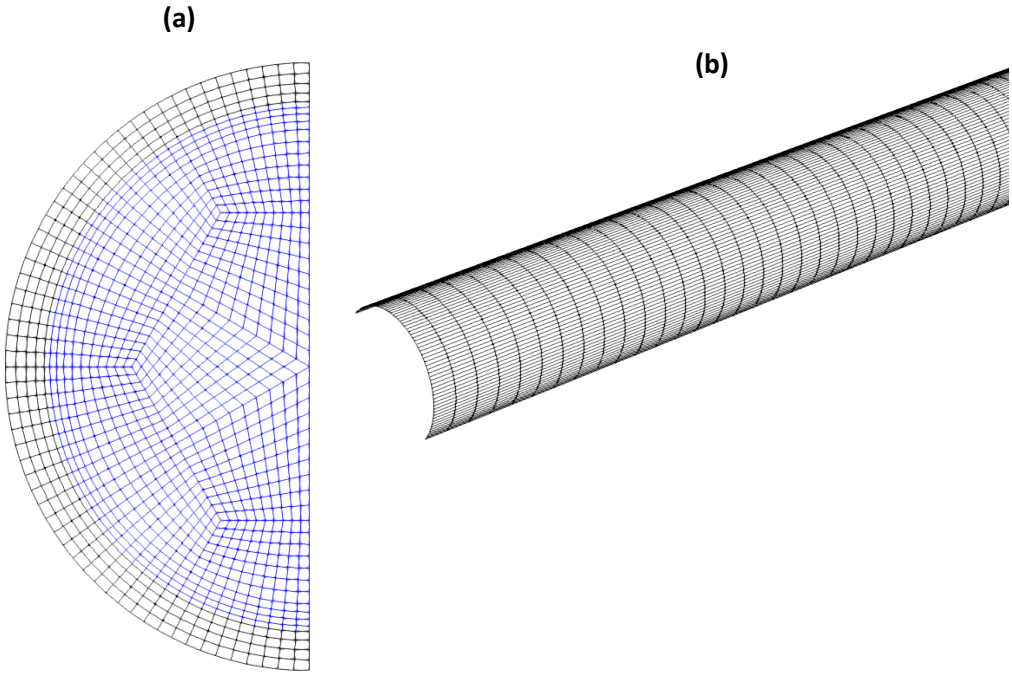

Figure III.2. Mesh generated by Salome Meca 2017. (a) Cross-section meshing, (b) Typical axial mesh.

Three mesh sizes with variable cross-sectional and axial meshing divisions were assumed, ranging from 0.34 to 1.2 million nodes. The inner wall boundary uses a logarithmic wall function, and the first mesh layer's distance from the wall is calculated to meet the y+>11.25 condition [6].

All equations' time terms are discretised with an implicit Eulerian scheme and a second-order limited linear scheme for the convective terms. The turbulence terms use the first-order Gauss upwind scheme to avoid simulation crashes. For the pressure-velocity coupled equations, the PISO algorithm was used. The simulations began with a rather significant Courant number; as the simulation approaches the steady state, it is modified to 0.9.

The boundary conditions for the fluid and solid regions are summarised in Table III.2 and Table III.3, respectively.

The numerical vapour quality at any cross-section will be estimated as follows:

$$x = \frac{\int \rho_v \left(\vec{U}_v \cdot \vec{n}\right) \alpha_v ds}{\dot{m}} \qquad \text{(III. 1)}$$

$\vec{n}$ is normal vector to cross-section oriented in the same direction as the flow.

Table III. 2. Boundary conditions for fluid region.

Variables	Inlet	Outlet	Interface fluid-solid	Symmetry
α_g	fixedValue	inletOutlet	zeroGradient	symmetryPlane
α_l	Calculated	Calculated	Calculated	SymmetryPlane
αt_g, αt_l (wall partitioned heat flux model)	Calculated	Calculated	Compressible: alpha-BoilingWallFunction	symmetryPlane
U_l / U_g	fixedValue	pressureInletOutlet-Velocity	fixedValue (0 0 0)	symmetryPlane
T_l	fixedValue	inletOutlet	Compressible: turbulentTemperature-TwoPhaseRadCouple-Mixed	symmetryPlane
T_g	fixedValue	inletOutlet	copiedFixedValue	symmetryPlane
$Prgh$ $(P - \rho gh)$	fixedFluxPr-essure	prghPressure	fixedFluxPressure	SymmetryPlane
P	Calculated	Calculated	Calculated	SymmetryPlane
k_l / k_g	fixedValue	inletOutlet	kqRwallFunction	symmetryPlane
ε_l / ε_g	fixedValue	inletOutlet	epsilonWallFunction	symmetryPlane
$\mu_{t,l}$ / $\mu_{t,g}$	Calculated	Calculated	nutkWallFunction	symmetryPlane

Table III.3. Boundary conditions for solid region.

Variables	*T*
Inlet wall	ZeroGradient
Outlet wall	ZeroGradient
External wall	ExternallWall-HeatFlux
Interface solid-fluid	Compressible: turbulent-Temperature-TwoPhase-RadCouple-Mixed
Symmetry	Symmetry-Plane

Table III.4. Mesh independence verification (case1).

Mesh size	Outlet void fraction (Lahey KEpsilon)	Outlet void fraction (Mixture KEpsilon)	Relative error (%) (Lahey KEpsilon)	Relative error (%) (Mixture KEpsilon)
Coarse mesh (340K nodes)	0.847449	0.77198		
Medium mesh (840K nodes)	0.836942	0.765752	-1.23984	-0.80676
Fine mesh (1200K nodes)	0.839058	0.769967	-0.99015	-0.26076
geometry mesh without symmetry assumption (612K nodes)	0.832396	0.762865	-1.77627	-1.18073

The Rouhani-Axelsson correlation [8] version of Steiner [7] is shown to be highly precise in predicting the void fraction in horizontal tubes for all flow patterns [3]. It is defined as:

$$\alpha_v = \frac{x}{\rho_v}\left[\left(1+0.12(1-x)\right)\left(\frac{x}{\rho_v}+\frac{1-x}{\rho_l}\right)+\frac{1.18(1-x)[g\sigma_t(\rho_l-\rho_v)]^{0.25}}{G\rho_l^{0.25}}\right]^{-1} \quad \text{(III. 2)}$$

The mesh independence test was performed using the experimental conditions of case 1, as summarized in Table III.1. These tests are shown in Figs III.3 (a) and (b), and in Table III.4.

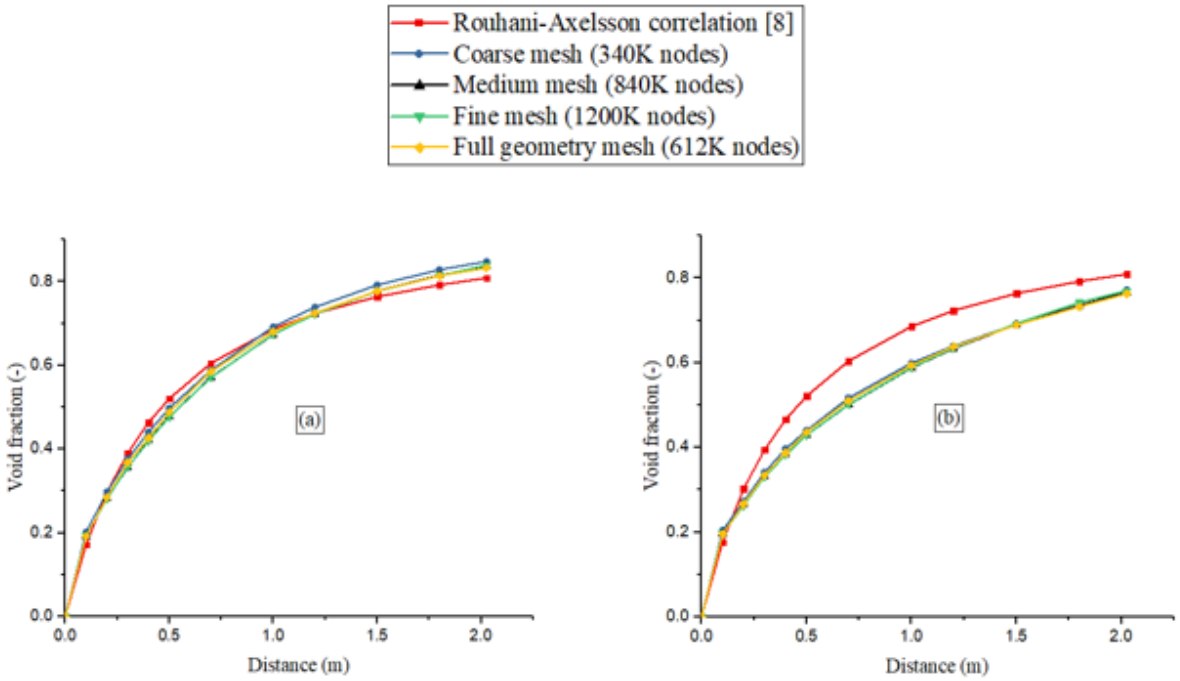

Figure III.3. Mesh independency verification (Operating conditions of Case 1, Table III.1). (a)- Lahey KEspsilon model. (b)- Mixture KEpsilon model.

From the medium mesh to the fine mesh, the relative errors of the outlet void fraction for both turbulence models are less than 1%. As a result, the solution is considered mesh-independent. The medium mesh will be utilized in the remaining simulations. Furthermore, applying a symmetry restriction to coarse, medium, and fine meshes proved sufficient, as the void fraction results agree with those of the entire geometry mesh for both turbulence models.

III.2.1.2. The void fraction results

The results of numerical simulations using the two turbulence models described above, considering the experimental parameters grouped in Table III.1, are shown in Figure III.4.

With an average relative error of 7.32%, the Lahey KEpsilon turbulence model [9] correctly predicted the vapour quality along the heated tube. However, using the Mixture KEpsilon model increased the error to 9.45%.

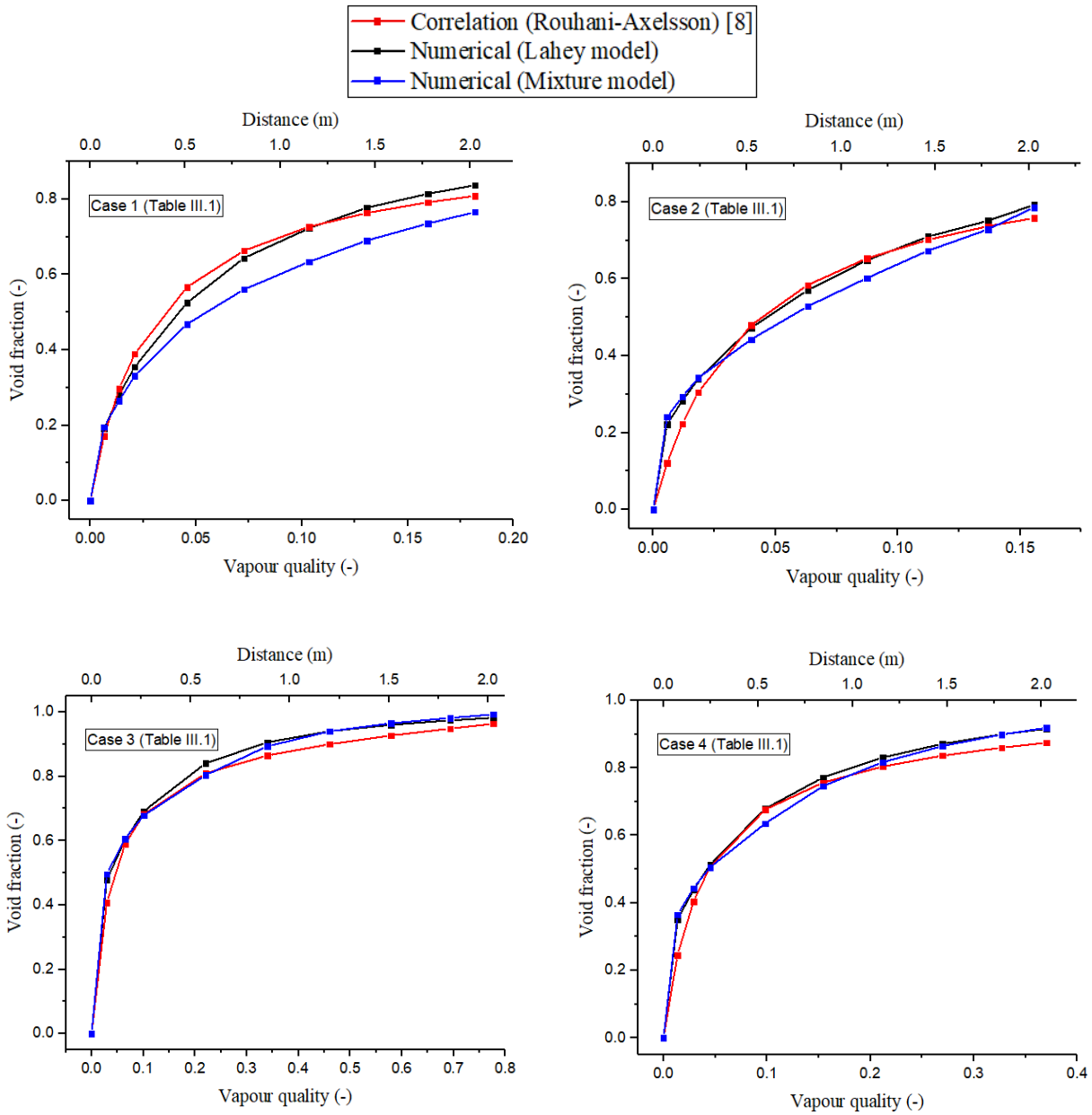

Figure III.4. The variation of void fraction with vapour quality in the different experimental conditions [3].

The Mixture KEpsilon model [10] for the test conditions of Case 1 produces noticeably under-predicted results due to the low vapour quality and high mass velocity relative to the other cases.

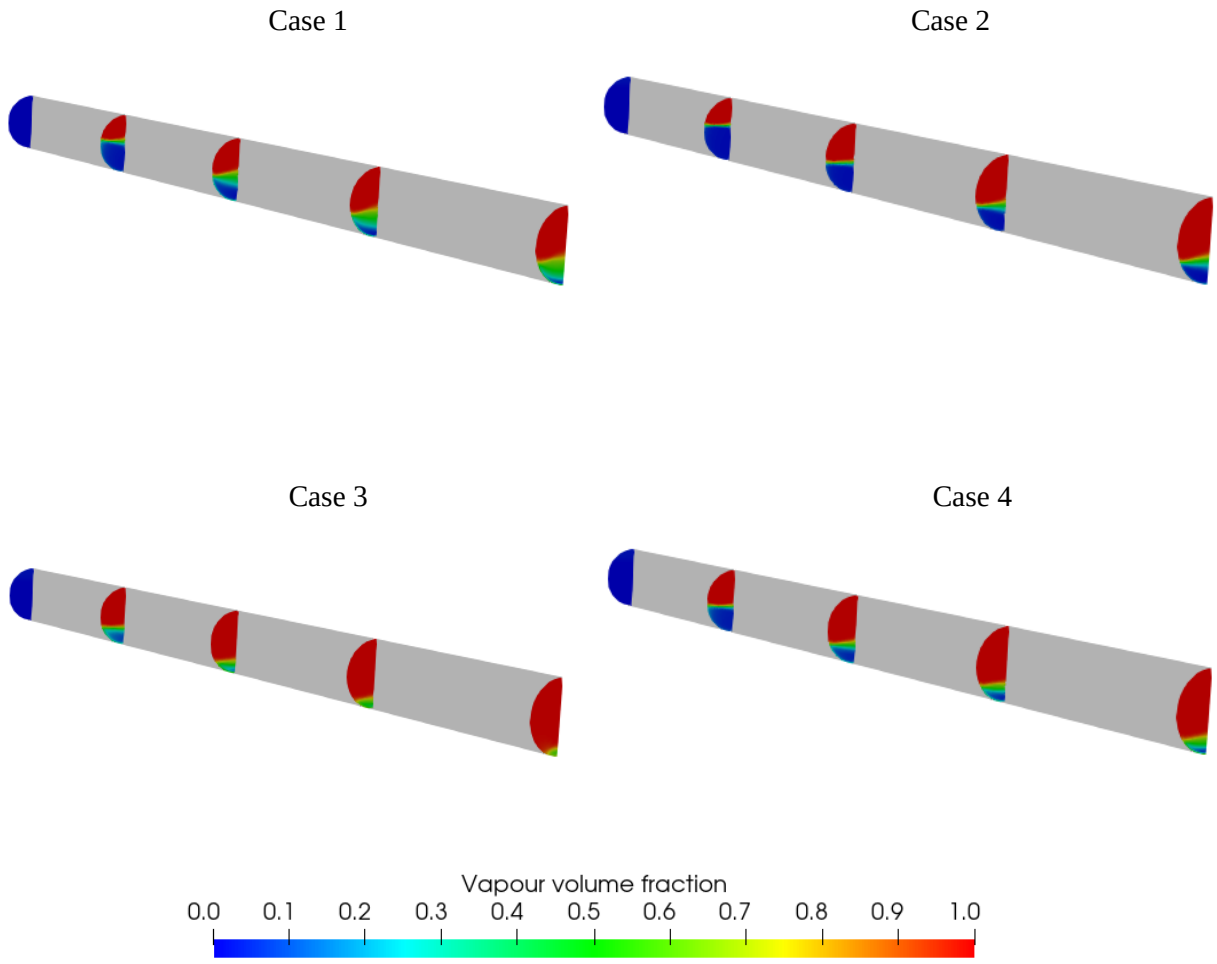

Figure III.5. The variation of void fraction with distance from the inlet (0m, 0.5m, 1m, 1.5m, 2.026m) using the Lahey KEpsilon turbulence model.

For low vapour quality, the turbulence of the liquid phase is dominant, and the vapour phase fluctuates in it, as in the case of the Lahey KEpsilon model. However, Mixture Epsilon treats both phases as a mixture, which needs to be corrected.

The void fraction distribution using the Lahey KEpsilon model is shown in Figure III.5. The distribution presents a stratified flow due to gravity with an unclear interface for all the cases. The Eulerian method does not follow liquid-gas interfaces; therefore, the other flow patterns are not seen [11]. Nevertheless, it is still practical for quantitative analysis and gives satisfactory results for void fractions, the primary purpose of this study.

III.2.1.3. The frictional pressure drop results

Quibén & Thome [4] and Quibén [5] used the same experimental setup as Wojtan et al. [1] to construct new correlations of the frictional pressure drop, taking into account the change of flow model using the Wojtan et al. [1] map. They established a correlation for each flow pattern and employed an interpolation technique in the equations to ensure a flexible transition when

the flow mode changes. Their primary objective [4, 12] was to avoid the constraints of previous correlations, such as Muller-Steinhagen & Heck [13], which do not consider the flow pattern and do not expect the peak of the frictional pressure drop at the start of dry-out.

In diabatic flow, the measured pressure drop is usually called the "total pressure drop," and it is made up of three parts:

$$\Delta P_{total} = \Delta P_{stat} + \Delta P_{mom} + \Delta P_{frict} \quad \text{(III. 3)}$$

(ΔP_{stat}) is the static pressure drop, it equals to zero for horizontal channels. Thus, the two-phase frictional pressure drop $\left(\Delta P_{frict}\right)$ is calculated as follows:

$$\Delta P_{frict} = \Delta P_{total} - \Delta P_{mom} \quad \text{(III. 4)}$$

(ΔP_{mom}) is the momentum pressure drop. It is defined as [4]:

$$\Delta P_{mom} = G^2 \left\{ \left[\frac{(1-x)^2}{\rho_l (1-\alpha_v)} + \frac{x^2}{\rho_v \alpha_v} \right]_{out} - \left[\frac{(1-x)^2}{\rho_l (1-\alpha_v)} + \frac{x^2}{\rho_v \alpha_v} \right]_{in} \right\} \quad \text{(III. 5)}$$

(ΔP_{mom}) equals to zero for an adiabatic channel.

Figure III.6 shows the comparison between the numerical friction loss and the experimental data (see references [4, 5])

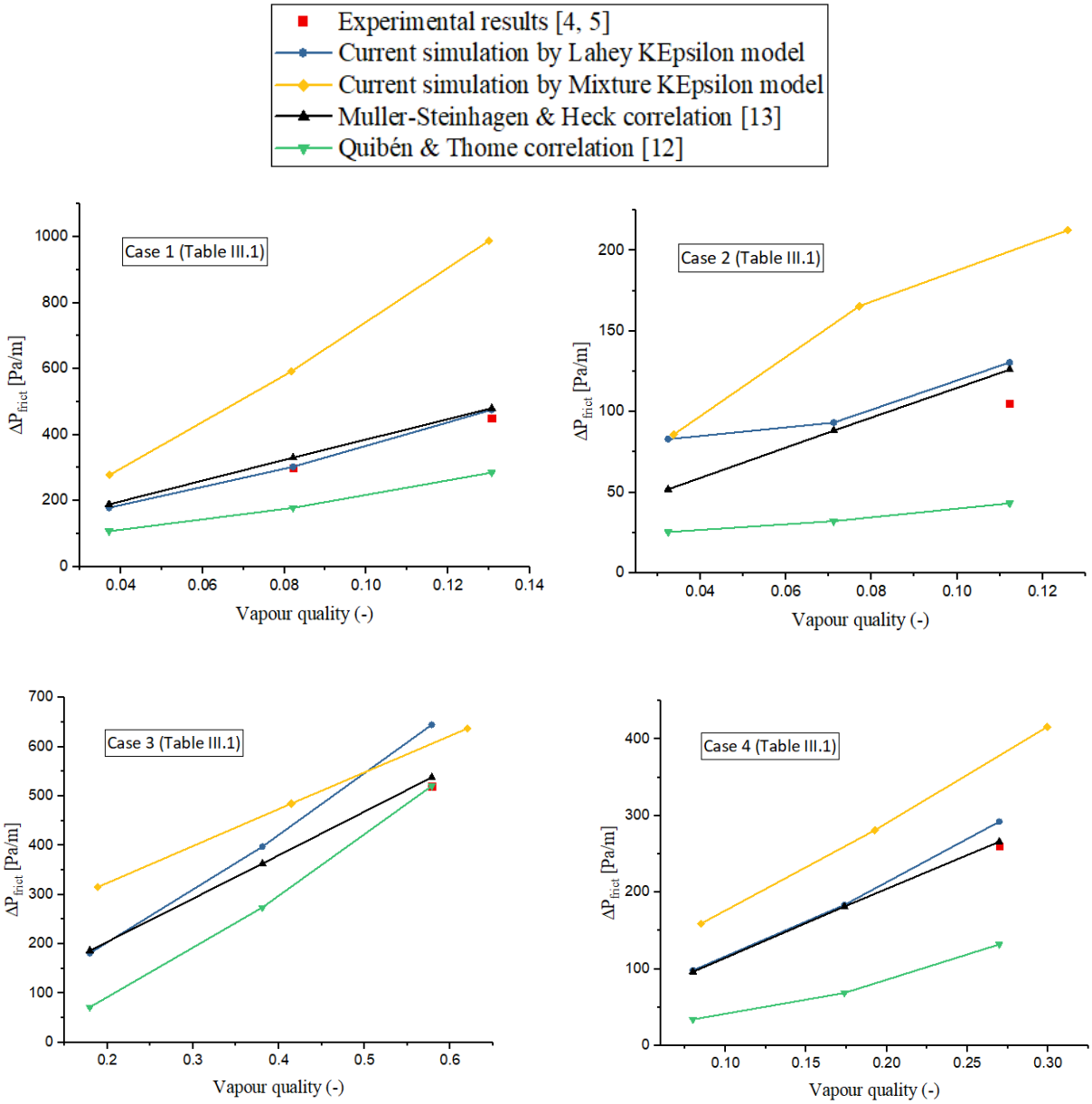

Figure III.6. Variations of the numerical and the experimental frictional pressure drop for different cases [4, 5].

The Lahey KEpsilon turbulence model predicts the pressure drop with a relative error of 10.84% for low vapour quality (<0.26). In contrast, at high vapour quality (>0.5), the MixtureKEpsilon model outperforms the Lahey KEpsilon model. Such a result is expected since the MixtureKEpsilon model was mainly developed for high void fraction flows (see reference [10]), which is not the case for the Lahey KEpsilon model.

The Muller-Steinhagen & Heck [13] correlation correctly anticipated pressure loss for all vapour qualities (as long as it did not reach the dry out of annular flow (x > 0.75)). Quibén and Thome's correlation [12], on the other hand, failed except for high vapour quality and needs further modifications and revisions.

III.2.2. Horizontal coiled tube

Sajadi et al. [2] (2021) studied heat transfer and pressure drop experimentally in helically coiled tubes using R1234yf as a working fluid, where the effects of the coil diameters and mass velocities were investigated.

The geometry assumed in this validation was a 2 m length tube with a 10.95 cm coil diameter. The tube's inner/outer diameters are 8.7/9.5 mm. The schematic of the geometry is shown below in Figure III.7 [2]:

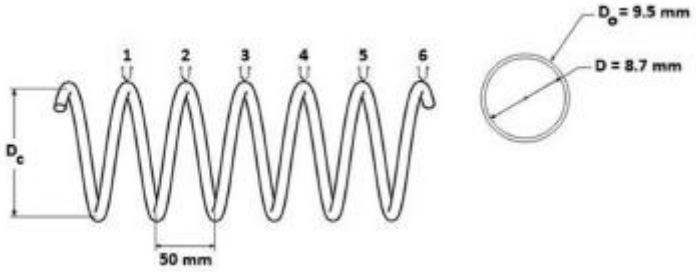

Figure III.7. The geometry of the experimental test section (by Sajadi et al. [2]).

The tube was heated by joule heating, so the source term in the energy equation was activated in the solid region of the domain (via fvOptions utility).

The boundary conditions are the same as in Tables III. (2, 3), except that epsilonWallFunction is replaced with omegaWallFunction due to using SatokOmegaSST as a turbulence model [14] for the liquid phase, and kOmegaSST for the vapour phase. The physical domain has no plane of symmetry that could be used to reduce the computational domain.

Table III.5. The experimental conditions (from Sajadi et al. [2]).

Cases	Mass velocity $G\ (kg/m^2\ s)$	Source power $q(W)$	Inlet-outlet vapour quality
1	330	900.137	0-0.3
2	330	600.09	0.3-0.5
3	330	751.49	0.5-0.75

III.2.2.1. Mesh independence tests

Considering the operating conditions of Case 1, two different meshes, shown in Figure III.8, were sufficient to rule on mesh independence. Table III.6 groups the total pressure drop and outlet void fraction results. With relative errors of 0.52% and 0.24%, respectively, the first mesh

size of 469,437 nodes is sufficient for the simulation and will be considered in the rest of the study.

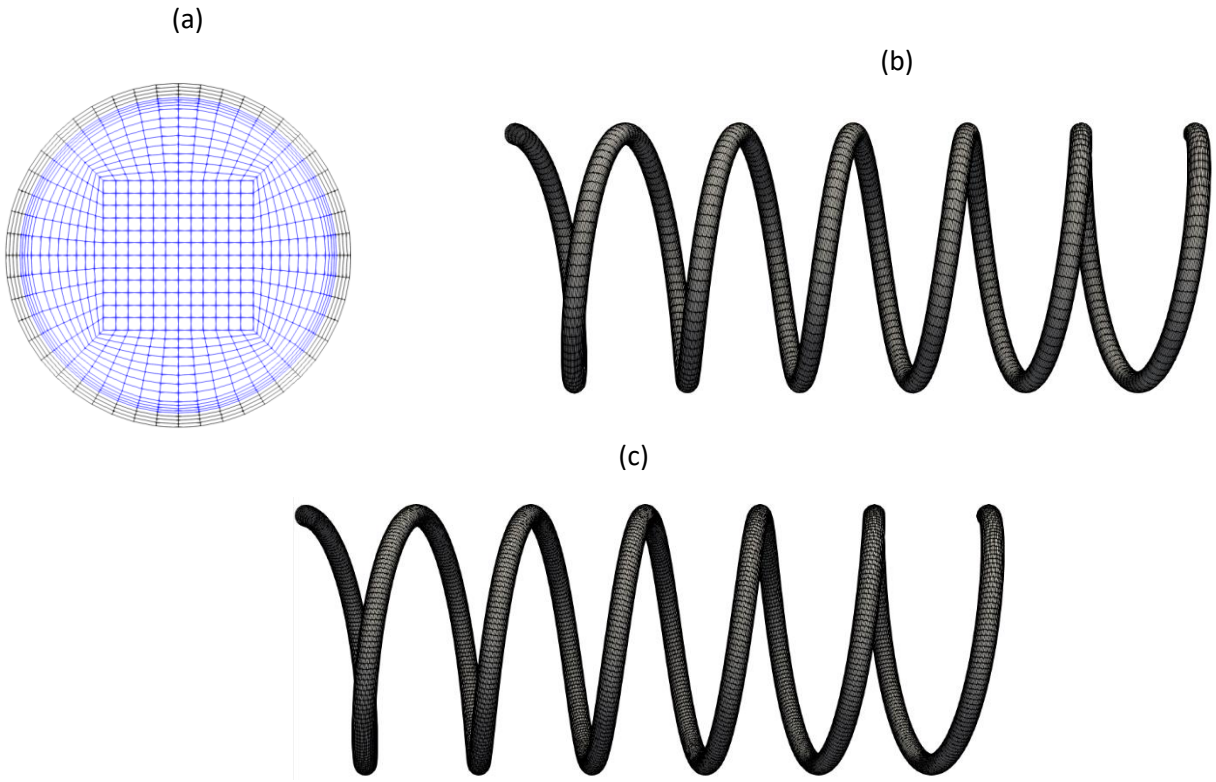

Figure III.8. Typical mesh: a) cross-sectional mesh; b) coarse wall mesh; c) fine wall mesh .

the obtained results for mesh independency are shown in Table III.6.

Table III.6. Mesh independency test (case 1).

	Δp [Pa] (between inlet and outlet)	Outlet void fraction
Mesh 1 (469437 nodes)	4146.12	0.8436
Mesh 2 (937937 nodes)	4124.51	0.8418

III.2.2.2. The frictional pressure drop results

As in the straight tube, the frictional pressure drop is calculated as follows:

$$\Delta P_{frict} = \Delta P_{total} - \Delta P_{mom} \quad \text{(III. 6)}$$

Figure III.9 compares numerical and experimental frictional pressure drops for different vapour qualities. It is essential to know that the experimental friction pressure drops, specific to a particular vapour quality, have been interpolated to obtain precise values for a better comparison with the numerical results. The good accord between numerical and experimental results for all values of vapour quality, with a mean relative error of 2.94%, confirms the

reliability of the kOmegaSSTsato as turbulence model [14] for the liquid phase and kOmegaSST for the vapour phase.

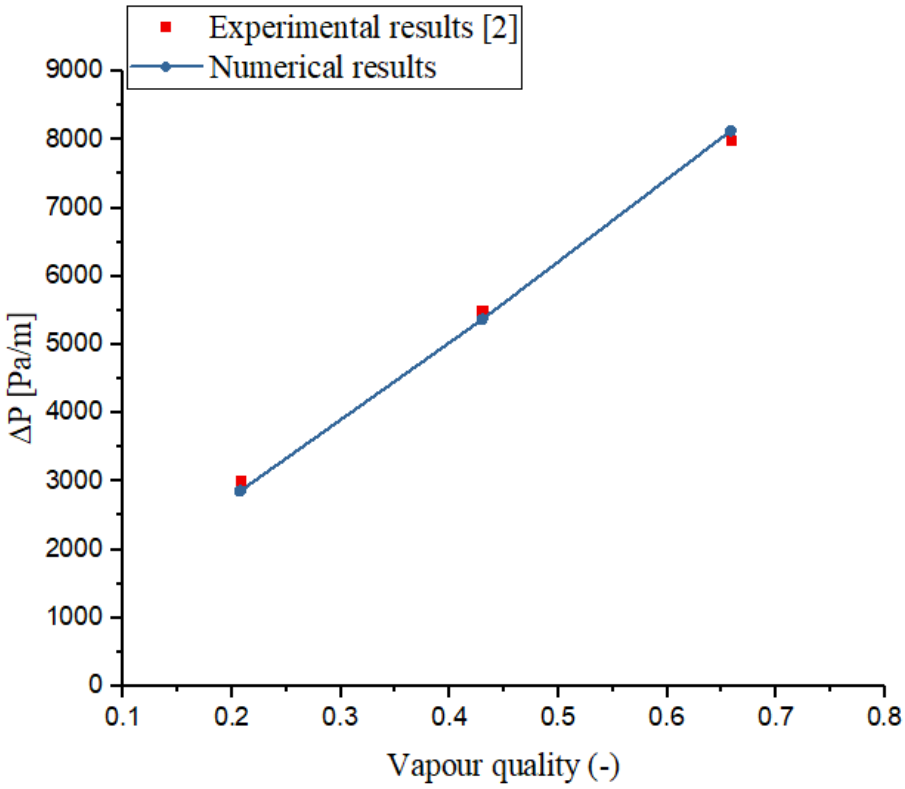

Figure III.9. The numerical and the experimental results of frictional pressure drop (horizontal coiled tube).

III.2.2.3. The void fraction results

The void fraction distribution in the cross-section of the coiled tube is shown for different locations for case 1 (example) in Figure III.10. The centrifugal force and gravity show their effects on the phase distribution. The liquid (high density) is always pushed to the outer side of the wall. It is apparent the dominance of gravity for cross sections of the down part of the coiled tube (π, 3π, 5π, 7π, 11π, 13π). In the upper part of the tube, the centrifugal force and gravity act in opposite directions, which leads to a mixture of phases for cross sections (2π, 4π, 6π, 8π, 10π, 12π). There is no experimental data for void fraction distributions to validate these numerical results, but the same observations have been remarked for similar studies in the literature [6, 11, 15, and 16].

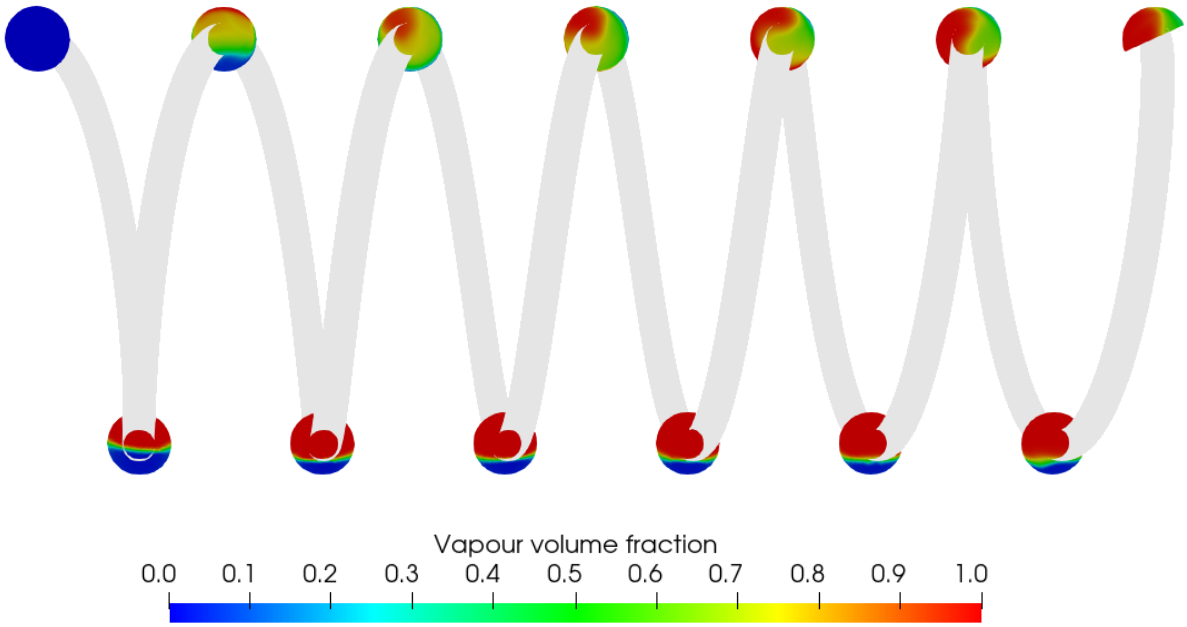

Figure III.10. The void fraction for different locations from the inlet (horizonat coiled tube).

III.3. Conclusion

The Eulerian two-fluid approach and the RPI wall-boiling model are validated with boiling flow regimes in horizontal straight and horizontal coiled tubes. The model validation is achieved for:

- Horizontal tube: The numerical results of the void fraction were in excellent agreement with the Steiner [7] version of the Rouhani-Axelsson correlation [8]. Also, the numerical frictional pressure drop agreed well with the experimental data of Quibén and Thome [4] and Quibén [5]. It has been found that the Lahey KEpsilon model is appropriate for low vapour quality, and the Mixture KEpsilon model is better for high values.
- Horizontal coiled tube: Using the experimental work of Sajadi et al. [2] for the mathematical validation, the numerical frictional pressure drop was in excellent agreement with the experimental data [2]. It was found that the SST turbulence model (Sato kOmegaSST for the liquid phase and kOmegaSST for the vapour phase) was suitable for such a coiled geometry.

After the mathematical model has been validated, it will be used to predict the thermo-hydraulic behaviour of DSG in the parabolic trough absorber of the DISS solar facility in Almeria, Spain, under actual operating conditions, and the straight absorber will then be replaced with the new S-shaped absorber as a unit collector, highlighting its benefits and limitations.

References

[1] Wojtan L, Ursenbacher T, Thome J. R. Investigation of flow boiling in horizontal tubes: Part I—A new diabatic two-phase flow pattern map. *International journal of heat and mass transfer*. 2005; 48(14): 2955-2969.

[2] Sajadi B, Naserinejad J, Akhavan-Benhabadi M.A, Razi P, Soleimani M. Heat transfer and pressure drop of R1234yf boiling in helically coiled tubes. *Heat Transfer Engineering*. 2021; 43(7): 584-597.

[3] Wojtan L. *Experimental and analytical investigation of void fraction and heat transfer during evaporation in horizontal tubes*. Thesis No. 2978, Swiss Federal Institute of Technology, Lausanne. 2004.

[4] Quibén J. M, Thome J. R. Flow pattern based two-phase frictional pressure drop model for horizontal tubes. Part I: Diabatic and adiabatic experimental study. *International Journal of Heat and Fluid Flow*. 2007; 28(5): 1049-1059.

[5] Quibén J. M. *Experimental and analytical study of two-phase pressure drops during evaporation in horizontal tubes*, PhD. Thesis, Swiss Federal Institute of Technology (EPFL), Lausanne, Switzerland. 2005.

[6] Abdous M. A, Holagh S.G, Saffari H. Numerical Investigation of Flow Boiling Heat Transfer in Helically Coiled Tube under Constant Heat Flux. *Thermal Science and Engineering*. 2018; 1: 1-18.

[7] Steiner D. Heat transfer to boiling saturated liquids. *VDI-Warmeatlas (VDI Heat Atlas)*. 1993.

[8] Rouhani S. Z, Axelsson E. Calculation of void volume fraction in the subcooled and quality boiling regions. *International Journal of Heat and Mass Transfer*. 1970; 13(2): 383-393.

[9] Lahey R. T. The simulation of multidimensional multiphase flows. *Nuclear Engineering and Design*. 2005; 235(10):1043-1060.

[10] Behzadi A, Issa R. I, Rusche H. Modelling of dispersed bubble and droplet flow at high phase fractions. *Chemical Engineering Science*. 2004; 59(4): 759-770.

[11] Wu H. L, Peng X. F, Ye P, Gong Y. E. Simulation of refrigerant flow boiling in serpentine tubes. *International Journal of Heat and Mass Transfer*. 2007; 50(5-6): 1186-1195.

[12] Quibén J. M, Thome J. R. Flow pattern based two-phase frictional pressure drop model for horizontal tubes, Part II: New phenomenological model. *International Journal of Heat and Fluid Flow*. 2007; 28(5): 1060-1072.

[13] Müller-Steinhagen H, Heck K. A simple friction pressure drop correlation for two-phase flow in pipes. *Chemical Engineering and Processing: Process Intensification*. 1986; 20(6): 297-308.

[14] Sato Y, Sadatomi M. Momentum and heat transfer in two-phase bubble flow - I, Theory. *International Journal of Multiphase Flow*. 1981; 7: 167-177.

[15] Sun B , Yu X , Liu S , Shi J, Yang L, Zhang G, Zhang P. Non-uniform wall temperature distribution of nucleate boiling heat transfer in helically coiled tubes. *Nuclear Engineering and Design*. 2018; 330: 356-367.

[16] Murai Y, Oiwa H, Sasaki T, Kondou K, Yoshikawa S, Yamamoto F. Backlight imaging tomography for gas liquid two-phase flow in a helically coiled tube. *Meas. Sci. Technol*. 2005; 16 (7): 1459–1468.

Chapter IV : Direct steam generation in the DISS test facility

IV.1. Introduction

After the validation of the mathematical model, the two-fluid Eulerian approach, and the RPI wall boiling model for the case of laboratory-scale straight and coiled horizontal tubes boiling flow studies, it is essential to verify its validity for full-scale commercial installations, similar to the DSG in DISS [1].

The physical phenomena in laboratory-scale evaporator tubes and those in commercial-scale solar absorbers for DSG are the same. However, the commercial-scale cases involve other parameters whose effects have yet to be verified, and this includes non-uniform heat flux around the absorber due to solar concentration and combined radiation/convection heat loss, which we will attempt to test in this chapter to see how the mathematical model responds to both. The DSG in the DISS test facility (Lobon et al. [1]) is an excellent outcome to validate our mathematical model for extreme and actual conditions where the effects of the overcurrent parameters are present.

IV.2. DSG in the DISS test facility

From the literature, most of the DSG studies in parabolic troughs [1-15] refer to the DISS test facility in Almeria, Spain. The system is flexible and can operate for different solar irradiation, flow properties, and operating modes (once-through, injection, and recirculation modes). The commonly used mode in literature is once through mode, as shown in Figure IV.1. The subcooled water flows through the loop by a feed water pump, passes within 13 collectors and evaporates. The generated vapour drives the turbine to generate electricity.

The three main steps along the DSG loop are described as follows:

- **Liquid water state**: In the first two collectors ET (200 m), the subcooled water is heated to saturation temperature. It can sometimes be expanded to the third collector (the first LS3) if the water does not reach saturation due to unfavourable operating conditions (low DNI, high mass velocity, low inlet temperature, Etc.).
- **Two-phase flow state:** Occurs in the evaporation section (LS3) (collectors #2 or #3 to #8 or #9) and is the most extended section (400m).
- **Vapour state**: Occurs in the superheating section to heat the saturated vapour from the end of collectors #8 or #9 until the last collector (13) (LS3).

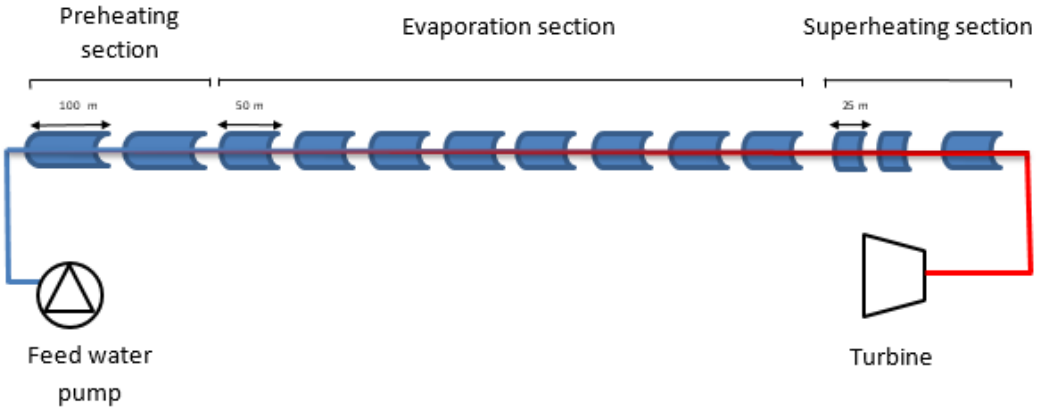

Figure IV.1. Schematic of the DISS test facility sections for once-through mode [1].

IV.2.1. The solar collector unit in the DISS test facility

It includes a parabolic mirror that collects and concentrates solar radiation on the solar receiver. The latter consists of a solar absorber tube inside a vacuumed glass envelope. The collector LS3 in the DISS facility has specific geometrical characteristics, optical efficiency, and validated experimental correlations, as described below.

IV.2.1.1. Geometrical characteristics

The evaporation section we are interested in is made up of LS3-type collectors, whose geometrical characteristics are listed in Table IV.1 below, in addition to the characteristics of the parabolic mirrors.

Table IV.1. The LS3 collector's geometrical characteristics [1].

Absorber	D_{outer}/D_{inner}	0.07/0.05 m
	Length	48.72 m
Mirror	Width	5.76 m
	Length	48.72 m
	Focal line	1.71 m

IV.2.1.2. Energy balances

Figure IV.2 shows the radiative/convective energy losses through the outer face of the glass tube surrounding the absorber tube where the working fluid circulates.

The energy absorbed by the solar receiver is defined below as:

$$q_{eff} = q - q_{loss} \quad \text{(IV. 1)}$$

Where q is the mean heat flux, it is applied at the absorber's outer surface after a multiple heat flux reduction due to the optical efficiency of different components (mirror, glass cover, solar absorber, Etc.).

Therefore, the heat flux at the receiver's outer surface wall (q) is defined as follows:

$$q = \eta \cdot DNI \frac{A_{aperture}}{A_{absorber}} \quad \text{(IV. 2)}$$

(η) is the overall efficiency of the collector. It includes the optical efficiency of the components (mirror reflectivity, glass cover transmissivity, receiver absorptivity, Etc.) and other losses and deviations.

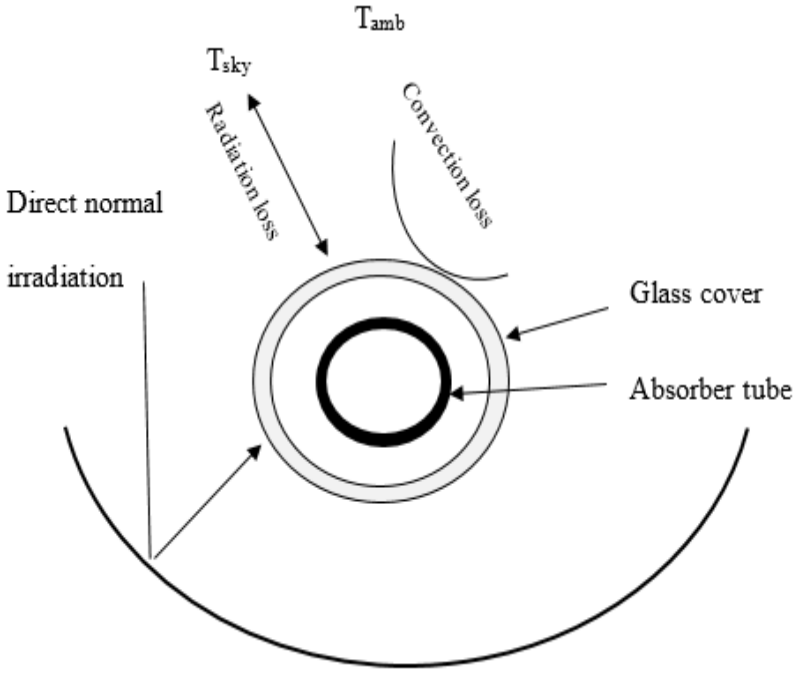

Figure IV.2. The energy balance in solar receiver [6].

(DNI) refers to the Direct Normal Irradiation.

(q) can also be described as the mean of the sum of local actual heat fluxes around the absorber:

$$q = \eta \cdot \frac{1}{2\pi} \cdot \int_0^{2\pi} q(\varphi) d\varphi \quad \text{(IV. 3)}$$

$q(\varphi)$ denotes the heat flux distribution around the absorber. It was created using the open source program Tonatiuh [16], employing the Monte Carlo ray tracing method.

(q_{loss}) is the heat loss by convection and radiation, which can be estimated accurately by the experimental correlation obtained by curve fitting for LS3 collectors (see References [1, 6, 13]); it is given as follows:

$$q_{loss} = U_L(T_a - T_{amb}) \quad \text{(IV. 4)}$$

Where:

$$U_L = a_1 + a_2(T_a - T_{amb}) + a_3(T_a - T_{amb})^2 \quad \text{(IV. 5)}$$

The coefficients a_1, a_2 and a_3 are derived from Table IV.2 (see Reference [13]).

Table IV.2. Curve-fitting coefficients for U_L of the LS-3 collector.

T_a	a_1	a_2	a_3
< 200	0.687257	0.001941	0.000026
≤ 300	1.433242	-0.00566	0.000046
> 300	2.895474	-0.01640	0.000065

IV.3. Validation of the mathematical model in the DISS facility

The numerical study of Lobon et al. [1] is about the DSG in the DISS test facility. This paper was chosen for this validation as it provides all the necessary experimental data required for this validation. Its experimental data was used in many recent works of literature [1, 6, 7, and 17]. This study will analyze two cases, as illustrated in Table IV.3.

Table IV.3. The DISS test cases.

Cases	$\boldsymbol{P_{in}[MPa]}$	$\boldsymbol{T_{in}}$ $\boldsymbol{[C]}$	**Mass flow** $\boldsymbol{[kg/s]}$	$\boldsymbol{DNI}$ $\boldsymbol{[W/m^2]}$
1	3.42	205	0.47	822
2	6.25	239	0.55	971

IV.3.1. Boundary conditions

As in chapters 2 and 3, the mathematical model and boundary conditions remain the same in this validation, except for the noun-uniform wall heat flux at the external wall that can not be applied with the standard OpenFOAM boundary condition module. It must be coded by groovyBC in the external library swak4FOAM. It enables the introduction of functions, tables, and transient variables in the boundary conditions in C++ language.

The boundary conditions for the fluid and solid regions are grouped in Tables IV.4 and IV.5, respectively.

Table IV.4. Boundary conditions for the fluid region in the solar absorber.

Variables	Inlet	Outlet	Interface fluid-solid	Symmetry
α_g	fixedValue	inletOutlet	zeroGradient	symmetryPlane
α_l	Calculated	Calculated	Calculated	SymmetryPlane
$\alpha t_g, \alpha t_l$ (wall partitioned heat flux model)	Calculated	Calculated	Compressible: alpha-BoilingWallFunction	symmetryPlane
U_l / U_g	fixedValue	pressureInletOutlet-Velocity	fixedValue (0 0 0)	symmetryPlane
T_l	fixedValue	inletOutlet	Compressible: turbulentTemperature-TwoPhaseRadCouple-Mixed	symmetryPlane
T_g	fixedValue	inletOutlet	copiedFixedValue	symmetryPlane
$Prgh$ $(P - \rho gh)$	fixedFluxPr-essure	prghPressure	fixedFluxPressure	SymmetryPlane
P	Calculated	Calculated	Calculated	SymmetryPlane
k_l / k_g	fixedValue	inletOutlet	kqRwallFunction	symmetryPlane
ε_l / ε_g	fixedValue	inletOutlet	epsilonWallFunction	symmetryPlane
$\mu_{t,l}$ / $\mu_{t,g}$	Calculated	Calculated	nutkWallFunction	symmetryPlane

Table IV.5. Boundary conditions for the solid region in the solar absorber.

Variables	T
Inlet wall	zeroGradient
Outlet wall	zeroGradient
External wall	groovyBC
Interface solid-fluid	Compressible:turbulent-Temperature-TwoPhase-RadCouple-Mixed
Symmetry	Symmetry-Plane

The applied external wall boundary condition is defined as:

$$-\lambda_a \frac{\partial T}{\partial n} = \left(\eta \cdot q(\varphi)\right) - \frac{\sigma\left(T_{a,wall}^4 - T_g^4\right)}{\frac{1}{\epsilon_a} + \frac{\left(1-\epsilon_g\right)}{\epsilon_g}\left(\frac{D_{a,outer}}{D_g}\right)} \quad \text{(IV. 6)}$$

Where:

$q(\varphi)$ represents the heat flux distribution obtained by the Monte Carlo method considering perfect optical efficiency.

(η), the overall optical efficiency; was not stated by Lobon et al. [1]. It can be defined as the rate of actual power that reaches the absorber (integrate local heat flux (obtained from the maximum heat flux and the normalized function) over the circumferential angle) to the power the aperture receives (see Reference [12]). By calculation, its value was found to be 0.51167, closer to Valenzuela et al. [13] $(\eta = 0.5)$ for a similar study.

Assuming an absolute vacuum in the glass-tube annulus, the heat losses (q_{loss}) reduce only to the radiation losses [6]; and then take the following form according to [7, 18]:

$$q_{loss} = \frac{\sigma\left(T_{a,wall}^4 - T_g^4\right)}{\frac{1}{\epsilon_a} + \frac{\left(1-\epsilon_g\right)}{\epsilon_g}\left(\frac{D_{a,outer}}{D_g}\right)} \quad \text{(IV. 7)}$$

T_g $(T_g = T_{amb} - 8)$ is the glass cover temperature, assumed as the sky temperature [18], and $T_{amb} = 25°C$ [14, 15].

IV.3.2. Heat flux by Tonatiuh software

The heat flux distribution on the outer face of the absorber tube was established using the Monte Carlo ray-tracing method under the Tonatiuh package [16] for the two cases (1, 2) in Table IV.1. The inputs for such simulations are the geometrical properties of the concentrator (LS3) and the DNI; all optical properties are assumed to be perfect, and the incidence angle is considered zero [1]. Finally, the results obtained will be exported in tabular form for OpenFOAM boundary conditions.

The 2D heat flux distributions for both cases are shown in Figure IV.3, and the 3D display in Figure IV.4.

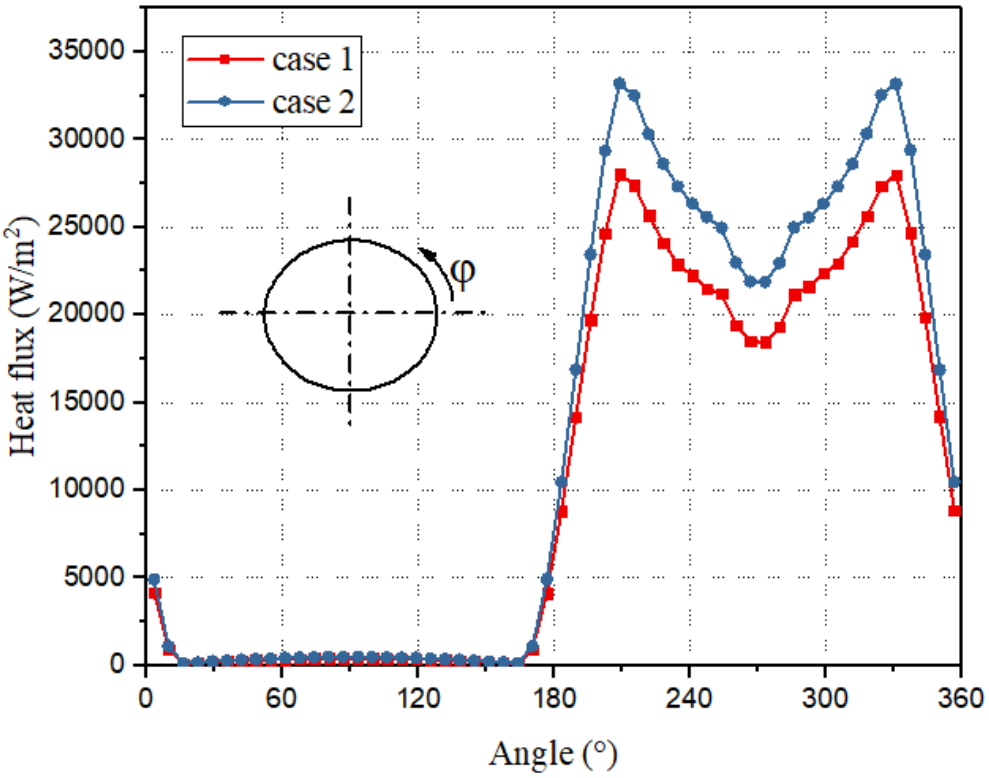

Figure IV.3. The outer wall heat flux influenced by optical efficiency Vs the circumferential angle.

Case 1

Case 2

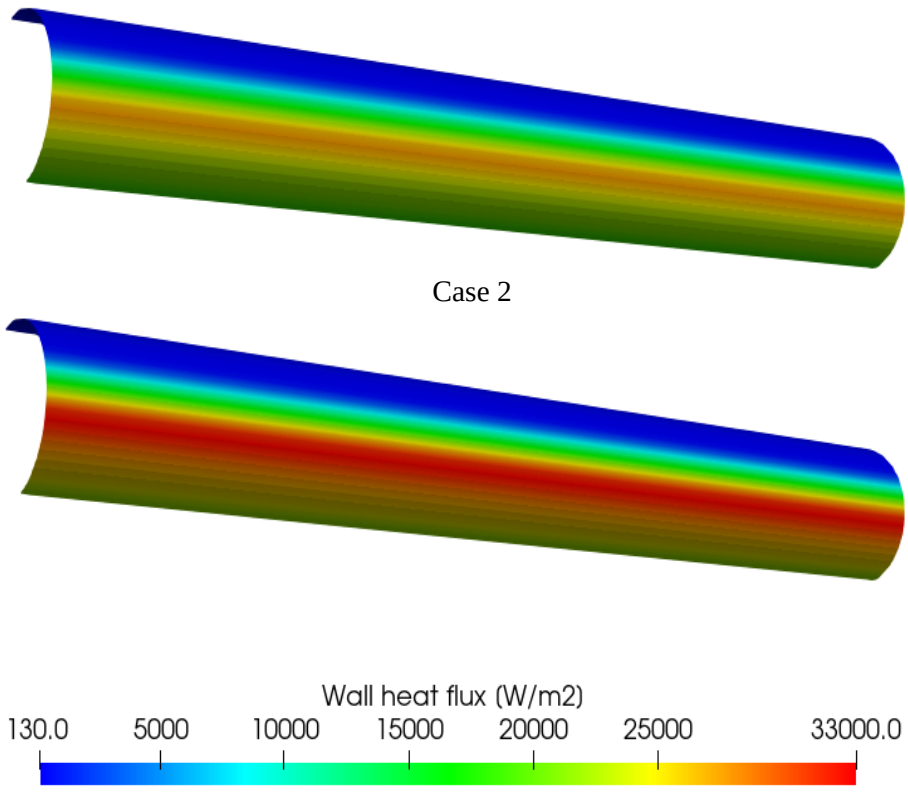

Figure IV.4. 3D display of the non-uniform heat flux distributions around the absorber.

IV.3.3. Mesh independency

The evaporation section is part of the interest in this study; it is 400m long and includes eight (08) collectors. Operating the simulation on eight (08) relays to the number of collectors would be preferable. In this way, each collector with a length of 50m will be considered alone in the simulation independently of the rest of the collectors, whose entry conditions are those of the exit results of the previous one, and so on until the last one. This last stunt is realized using the OpenFOAM utility "mapFields".

In order to perform a solution mesh independence test, the first collector in the evaporation section (collector #2 (LS-3)) in case 1 (Table IV.3) is simulated with three different mesh refinements.

The meshes differ in the number of axial divisions (1000-2000), while the central square of the cross-section is divided into 7:14 on both sides. A smooth growth of the mesh divisions is consummated between the first cell to the wall (y+>11.25) to the first cell to the central square, as shown in Figure IV .5.

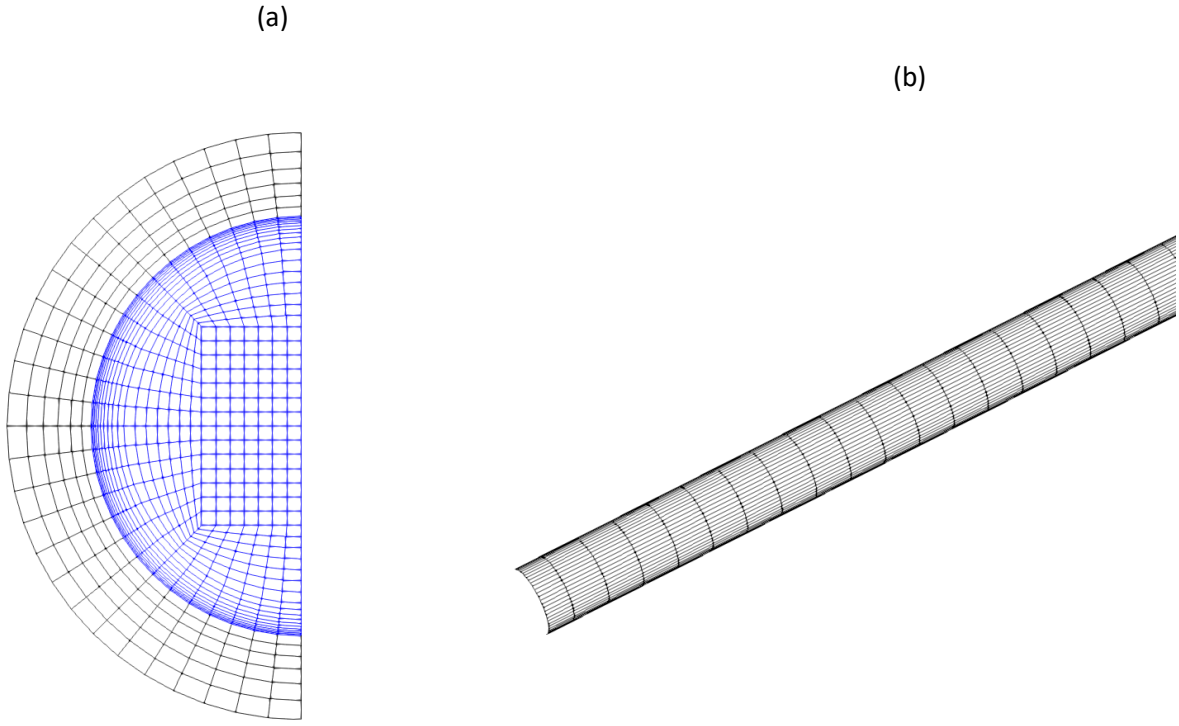

Figure IV.5. The absorber mesh generated by Salome Meca 2017. (a) Cross-section meshing, (b) Axial meshing.

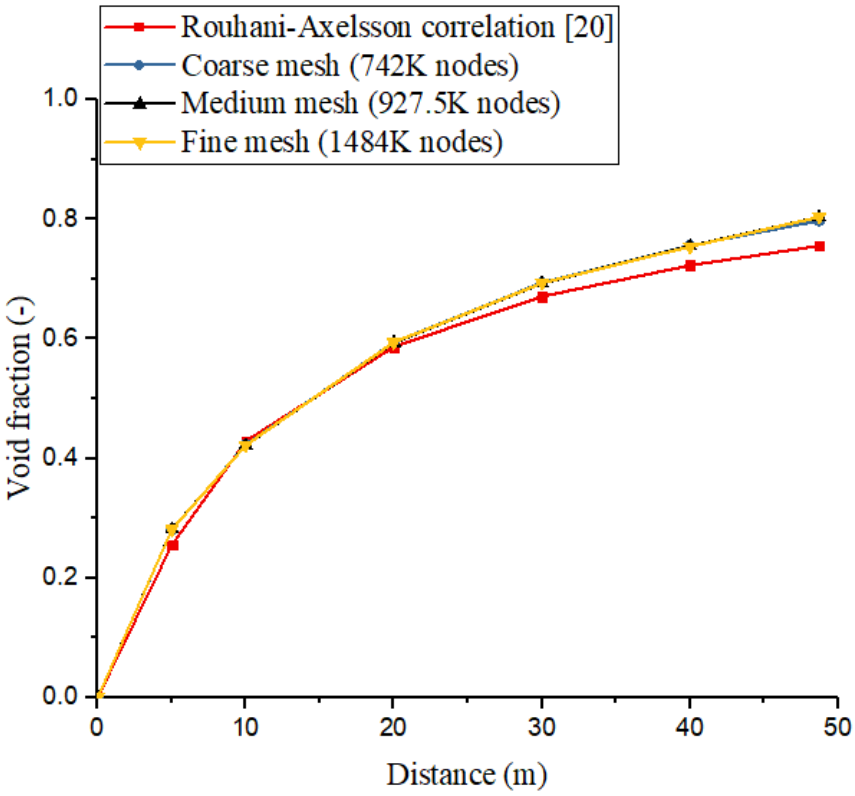

Figure IV.6. Mesh sensitivity verification (collector #2, case 1).

The average relative difference in output void fraction for mesh 2 (medium) and mesh 3 (fine) is less than 0.052%, indicating that mesh 2 can be used accurately for the remainder of the simulations (see Figure IV.6).

In these tests, the Lahey KEpsilon turbulence model and collector 2 of case 1 were assumed. The vapour quality at the outlet of collector 2 in case 1 is 0.137, which justifies using the Lahey KEpsilon turbulence model in these tests, which is better for low vapour quality, as discussed in the previous chapter.

IV.4. Results and discussion

The results obtained after performing the simulation of the entire evaporation section (8x50m, collector #2 to #9), the results will be compared to the experimental data [1], the numerical results of Lobon et al. [1], and the experimentally validated correlations for DSG in DISS [19, 20].

IV.4.1. The pressure drop

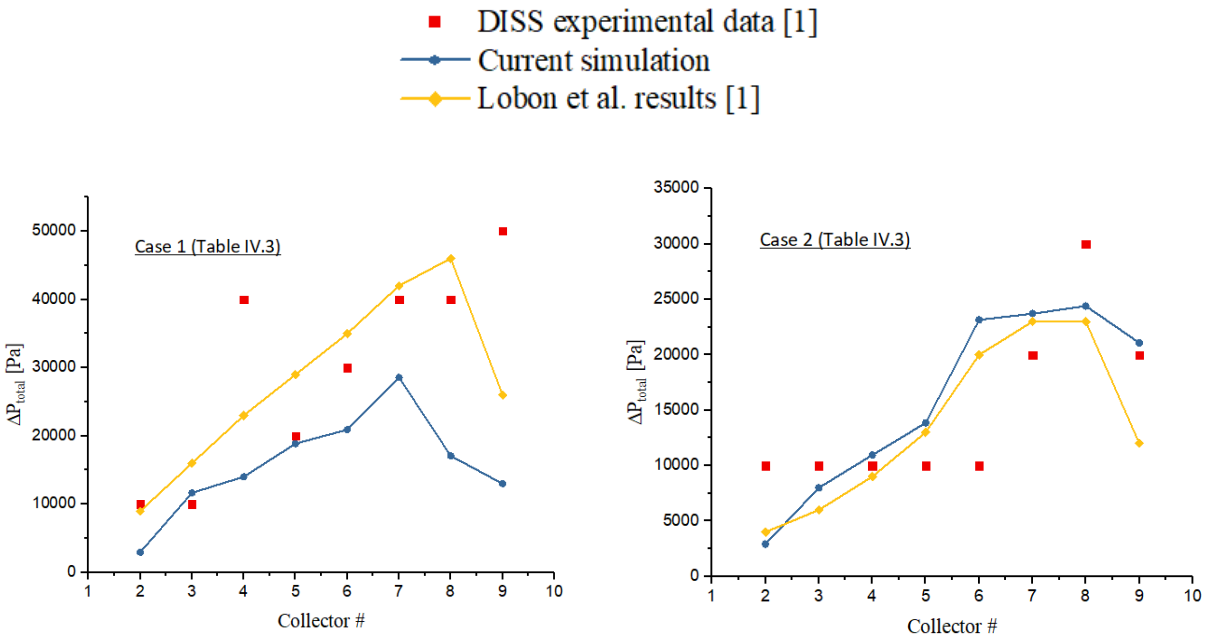

Figure IV.7. Comparison between numerical total pressure drop, experimental data, and Lobon et al. [1].

The experimental pressure data [1] are given only between collectors. It is easy to determine the pressure drop in each collector. Figure IV.7 shows the numerical total pressure loss through each collector of the evaporation section (collector #2 to #9) compared with the experiment data [1] and the CFD results by Lobon et al. [1]. For case 2, the current results are in good agreement with the numerical results of Lobon et al. [1] for all collectors. However, it presents a relative error of 39.12% compared to the experimental data, as they are measured with large uncertainties and errors. Whereas for case 1, the numerical results underpredict the pressure drop, especially for the last collectors, and marked a relative error of 39.28%. Nevertheless, it remains within the margin of error prediction of previous research in the literature [6].

It must be known that the relative error between the numerical and experimental results is taken for each point as an absolute value. Therefore, it shows such a high error percentage.

In order to calculate the frictional pressure drop along the absorber or predict the pressure drop for a specific vapour quality, the experimental correlation of Friedel [19] is used. It is the most accurate during the research of DSG in the DISS facility, and it is adopted in many research works [4, 6, and 8].

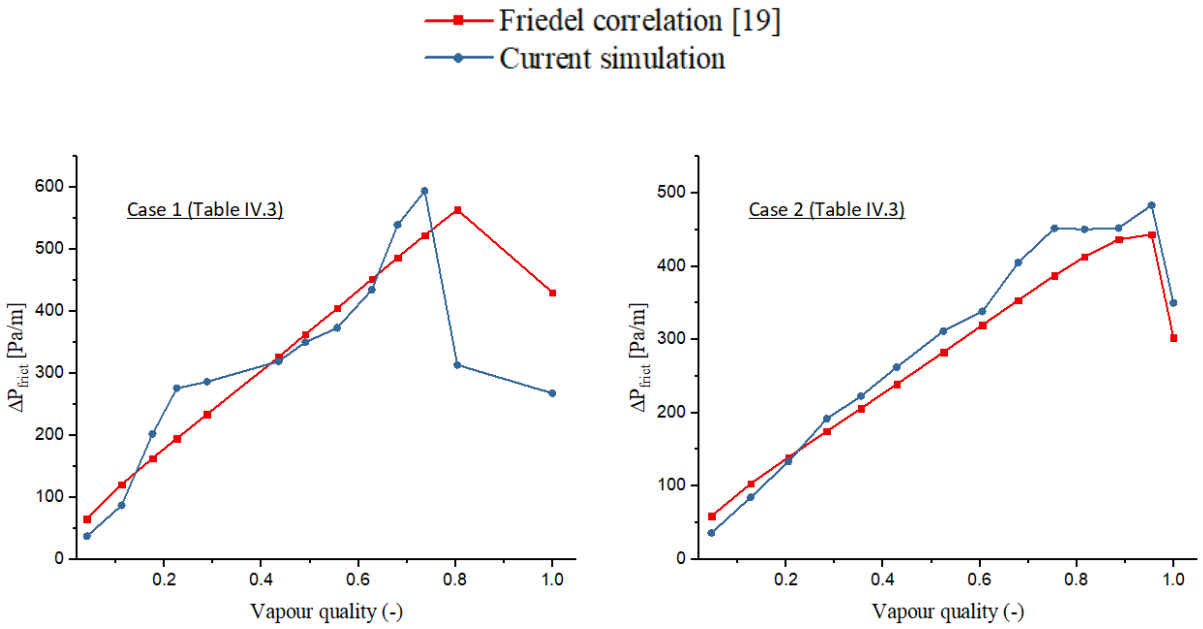

Figure IV.8. Frictional pressure drop: numerical and Friedel correlation comparison.

Figure IV.8 presents the evolution of the frictional pressure drop for numerical results and the Friedel correlation for both cases (1, 2). The Lahey KEpsilon turbulence model is used for low vapour quality, and the Mixture KEpsilon model is for higher. The model change occurs at the outlet of collector 4 when both turbulence models give similar results. Generally, there is a good consistency between the numerical results and the correlation for cases 1 and 2, with an overall relative error of 21.71% and 12.41%, respectively.

IV.4.2. Void fraction

The void fraction results are crucial to accounting for boiling flow pressure drop and mass transfer. In the literature [4, 8], many researchers in DSG in the DISS facility domain adopted the Rouhani-Axelsson correlation for void fraction [20], which gives a satisfactory prediction.

This study compares the numerical void fraction with the Rouhani-Axelsson correlation for both cases. Figure IV.9 shows excellent agreement between the numerical results and the correlation for both cases, where the relative error for case 1 is 3.89% and for case 2 is 3.17%.

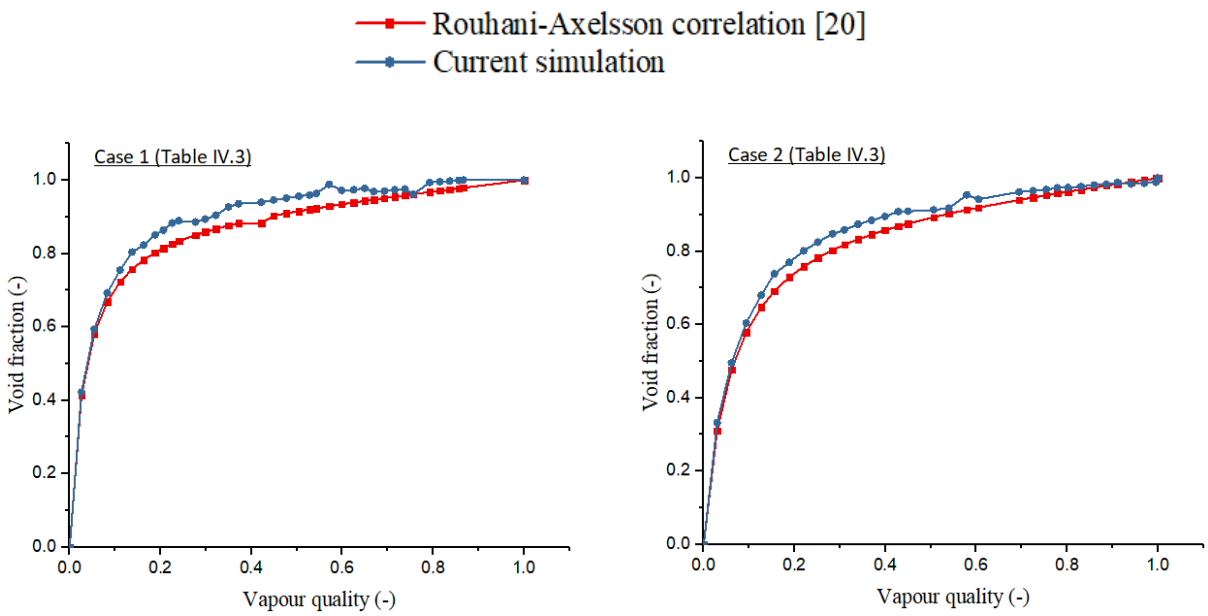

Figure IV.9. The void fraction in the evaporation section for cases (1, 2).

The numerical void fraction at the outlet of each collector is shown in Figure IV.10.

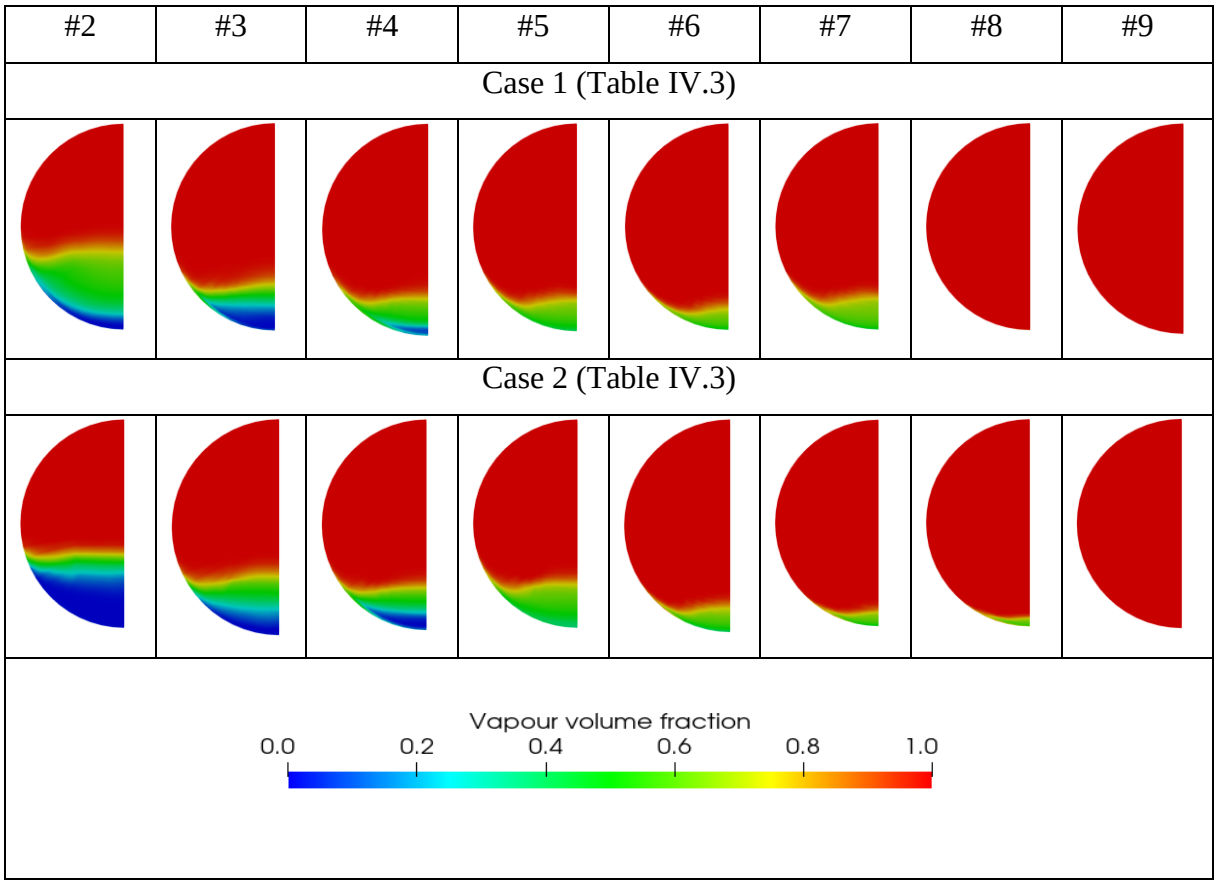

Figure IV.10. Variation of the void fraction at the outlet of each collector.

IV.4.3. Wall temperature

Wall temperature distribution in the solar absorber is very important in its design. For a high circumferential temperature gradient, the absorber can bend from the focal line and not intercept all the reflected solar radiation from the mirror. In the LS3 collector of the DISS solar power plant, the absorber's maximum circumferential temperature difference should not exceed 50K [4].

The flow characteristics and the non-uniform heat flux applied at the receiver's outer surface influence the circumferential wall temperature of the solar absorber. The maximum temperature is usually marked at the absorber's bottom (left and right), corresponding to the largest heat flux. It lowers significantly in the shadow zone (bottom side of the absorber). The upper half of the absorber facing the sun has the lowest temperature because it is heated directly by the sunlight without concentration/reflection from the mirror (see Figure IV.11).

The maximum wall circumferential temperature gradients for both cases are noticed at the outlet of the evaporation section (collector #9) due to the low conductivity of the vapour near the wall. The maximum wall temperature difference for case 1 is ΔT=30.817 K, and for case 2 is ΔT=26.72 K, which is in the range of the safety zone [4].

In order to validate the adopted equation (IV.7) to account for energy losses by radiation, the numerical heat loss will be compared to the experimental correlation of LS3-DISS (equation (IV.4)) [13]. The overall numerical heat loss for case 1 is $564.52\ W/m^2$, and by experimental correlation, it is $591.24\ W/m^2$. Whereas the numerical heat loss for case 2 is $772.45\ W/m^2$, and by the experimental correlation, it is $810.36\ W/m^2$.

The corresponding relative error for heat loss (between the numerical results and the experimental correlation) for cases 1 and 2 is -4.52% and -4.86%, respectively. It ensures the validity of the mathematical model.

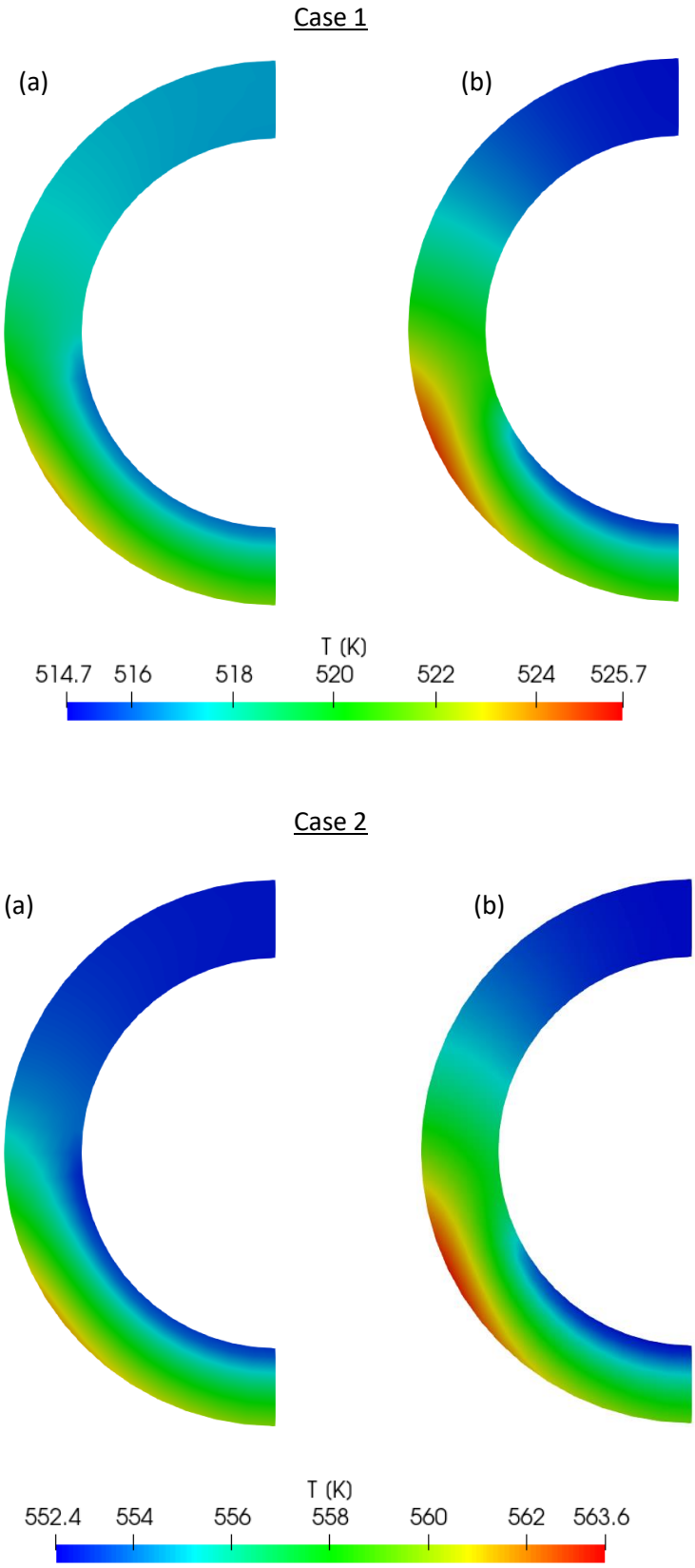

Figure IV.11. Wall temperature distribution for various absorber wall sections (a- coll #2, b- coll #5).

IV.5. Conclusion

The numerical study of DSG in the parabolic trough in the DISS solar power facility is validated with an Eulerian two-fluid approach and the RPI wall-boiling model, in addition to the receiver external wall modelling for heat absorption and loss via swak4FOAM library and Tonatiuh outputs (as a simulator for the Monte Carlo method).

The validation for this commercial-scale solar absorber is achieved for the following:

- Total pressure drop: comparison of the numerical total pressure drop with the experimental data [1] and the CFD results of Lobon et al. [1], the results were adequate compared to 1D numerical simulations in the literature.
- Frictional pressure drop: comparison of the numerical frictional pressure drop with Friedel correlation [19], commonly used in the DISS. The overall relative error is 17.06%.
- Void fraction: comparison of the numerical results of the void fraction to the Rouhani-Axelsson correlation [20], which is commonly used in DSG in literature. The overall relative error is 3.53%.
- Heat loss: comparison of the numerical heat loss with the experiment correlation [13] developed as a curve fitting for DSG in DISS. The relative error is -4.69%.

This combination of mathematical models was able to predict the different thermohydraulic parameters in DSG. It can also handle the simulation of DSG with different modifications or insertions in the solar absorber.

In the next chapter, this mathematical model will be used to study DSG in the DISS facility with the S-solar absorber shape.

References

[1] Lobón D. H, Baglietto E, Valenzuela L, Zarza E. Modeling direct steam generation in solar collectors with multiphase CFD. *Applied Energy*. 2014; 113: 1338-1348.

[2] Giglio A, Lanzini A, Leone P, García M. M. R, Moya E. Z. Direct steam generation in parabolic-trough collectors: a review about the technology and a thermo-economic analysis of a hybrid system. *Renewable and Sustainable Energy Reviews*. 2017; 74: 453-473.

[3] Dirker J, Juggurnath D, Kaya A, Osowade E. A, Simpson M, Lecompte S, ... & Markides C. N. Thermal energy processes in direct steam generation solar systems: Boiling, condensation and energy storage–A review. *Frontiers in Energy Research*. 2019; 6: 147.

[4] Eck M, Steinmann W. D. Modeling and design of direct solar steam generating collector fields. *J. Sol. Energy Eng*.2005; 127(3): 371-380.

[5] Valenzuela L, Zarza E, Berenguel M, Camacho E. F. Control scheme for direct steam generation in parabolic troughs under recirculation operation mode. *Solar Energy*. 2006; 80(1): 1-17.

[6] Hachicha A. A, Rodríguez I, Ghenai C. Thermo-hydraulic analysis and numerical simulation of a parabolic trough solar collector for direct steam generation. *Applied Energy*. 2018; 214: 152-165.

[7] Kumar B. N, Reddy K. S. Comparison of two-phase flow correlations for thermo-hydraulic modeling of direct steam generation in a solar parabolic trough collector system. *Journal of Thermal Science and Engineering Applications*. 2018; 10(4), 041005.

[8] Biencinto M, González L, Valenzuela L. A quasi-dynamic simulation model for direct steam generation in parabolic troughs using TRNSYS. *Applied energy*. 2016; 161: 133-142.

[9] Eck M, Zarza E, Eickhoff M, Rheinländer J, Valenzuela L. Applied research concerning the direct steam generation in parabolic troughs. *Solar energy*. 2003; 74(4): 341-351.

[10] Zarza E, Valenzuela L, Leon J, Hennecke K, Eck M, Weyers H. D, Eickhoff M. Direct steam generation in parabolic troughs: Final results and conclusions of the DISS project. *Energy*. 2004; 29(5-6): 635-644.

[11] Pal R. K, Kumar R. Two-fluid modeling of direct steam generation in the receiver of parabolic trough solar collector with non-uniform heat flux. *Energy*. 2021; 226, 120308.

[12] Roldan M.I, Valenzuela L, Zarza E. Thermal analysis of solar receiver pipes with superheated steam. *Applied energy*. 2013; 103: 73-84.

[13] Valenzuela L, Zarza E, Berenguel M, Camacho E. F. Control concepts for direct steam generation in parabolic troughs. *Solar Energy*. 2005; 78(2): 301-311.

[14] Montes M. J, Rovira A, Muñoz M, Martínez-Val J. M. Performance analysis of an integrated solar combined cycle using direct steam generation in parabolic trough collectors. *Applied energy*. 2011; 88(9): 3228-3238.

[15] Hoffmann A, Merk B, Hirsch T, Pitz-Paal R. Simulationen zur Thermofluiddynamik in Absorberrohren von Parabolrinnenkraftwerken mit Direktverdampfung mit dem Computercode ATHLET. *Kerntechnik*. 2014; 79(3): 175-185.

[16] Blanco M.J, Mutuberria A, Garcia P, Gastesi R, Martin V. Preliminary validation of Tonatiuh. *SOLARPACES Symposium*. 2009. Berlin, Germany.

[17] Elsafi A.M. On thermo-hydraulic modeling of direcr steam generation. *Solar Energy*. 2015; 120: 636-650.

[18] Forristall, R. *Heat transfer analysis and modeling of a parabolic trough solar receiver implemented in engineering equation solver*. (No. NREL/TP-550-34169). National Renewable Energy Lab, Golden, CO. (US). 2003.

[19] Friedel L. Improved friction pressure drop correlation for horizontal and vertical two-phase pipe flow. *Proc. of European Two-Phase Flow Group Meet*. 1979. Ispra, Italy.

[20] Rouhani S. Z, Axelsson E. Calculation of void volume fraction in the subcooled and quality boiling regions. *International Journal of Heat and Mass Transfer*. 1970; 13(2): 383-393.

Chapter V : Direct steam generation in the DISS test facility with an S-shaped absorber

V.1. Introduction

The Eulerian two-fluid approach and the RPI wall boiling model showed good consistency in the laboratory-scale studies of boiling flow in straight and coiled horizontal tubes, and they were able to simulate the commercial scale of the DSG in the parabolic trough when coupled with the Tonatiuh output of heat flux. The model was flexible for different geometries and scales, as there are no empirical correlations or models specific to a unique geometry like in most studies in the literature [1–5].

The straight absorber in the DISS facility [6-8] will be replaced with the new S one provided by Demagh et al. [9], keeping the same operating conditions. A comparative numerical study will take place for different results of frictional pressure drop, maximum wall temperature, and phase distribution, showing the advantages and disadvantages of the new absorber.

V.2. DSG in the DISS Test Facility

This study is a continuation of the previous study of DSG in the DISS test facility under the once-through mode, as shown in Figure V.1.

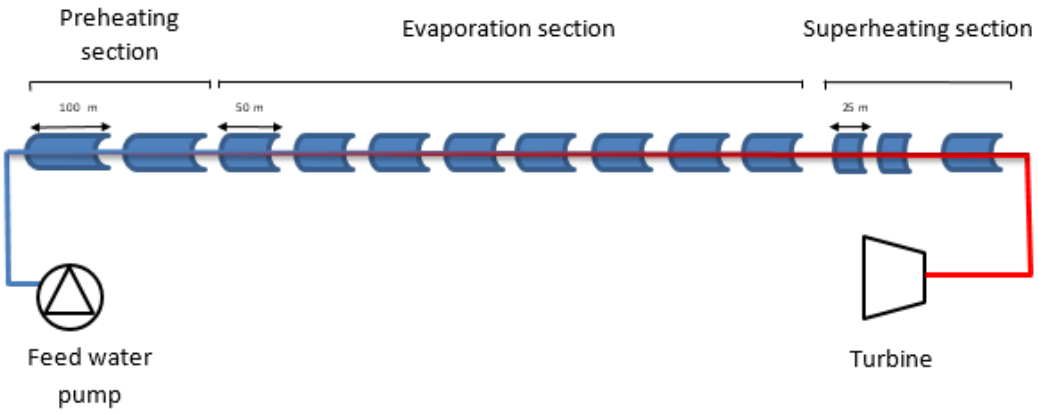

Figure V.1. Schematic of the DISS test facility sections for once-through mode [6].

The absorber in the evaporation section will be replaced with a corrugated one, as shown in Figure V.2.

Figure V.2. The geometry of the absorbers, straight (left), and the new S-shaped (right) [10].

To ensure the fidelity of the comparison, the S-shaped absorber is put under the same geometrical characteristics and operating conditions as the straight one, as illustrated in Tables V.1 and V.2.

Table V.1. The LS3 collector's geometrical characteristics for straight and S-shaped absorber [6].

Absorber	D_{outer}/D_{inner}	0.07/0.05 m
	Length	48.72 m
Mirror	Width	5.76 m
	Length	48.72 m
	Focal line	1.71 m

Table V.2. The DISS test cases for straight and S-shaped absorber [6].

Cases	$P_{in}[MPa]$	T_{in} $[C]$	Mass flow $[kg/s]$	DNI $[W/m^2]$
1	3.42	205	0.47	822
2	6.25	239	0.55	971

V.2.1. The S-shaped absorber constraints

The absorber in the parabolic trough is placed in a focal position, in which it intercepts all the reflected rays, and any displacement relative to the focal line can affect the interception process. Fortunately, for a slight deviation Δ, the absorber can still intercept the entire rays as long as it does not exceed the maximum acceptable deviation Δ_{max} that is defined as [9]:

$$\Delta_{max} = \frac{D_e}{2} - \left[f_l + \frac{L_r^2}{16 f_l} \right] \sin(\theta_{sun}) \qquad \text{(V. 1)}$$

Where, from Table V.1, $D_e = 0.07\ m$ is the external absorber diameter, $L_r = 5.76\ m$ is the aperture width, $f_l = 1.71m$ is the focal length, and $\theta_{sun} = 16'$ is the finite size of the sun half angle.

Applying the LS3 collector geometrical characteristics, $\Delta_{max} = 0.02141\ m$.

Then, the absorber shape can be defined as:

$$y = g(z) = A \cdot \left(\cos\left(\left(\frac{2\pi}{\lambda} \right) \cdot z \right) - 1 \right) \qquad \text{(V. 2)}$$

Where, $2A = \Delta = 2\ cm$ is peak to peak amplitude, and $\lambda = 0.195\ m$ is periodicity length as shown below in Figure V.3.

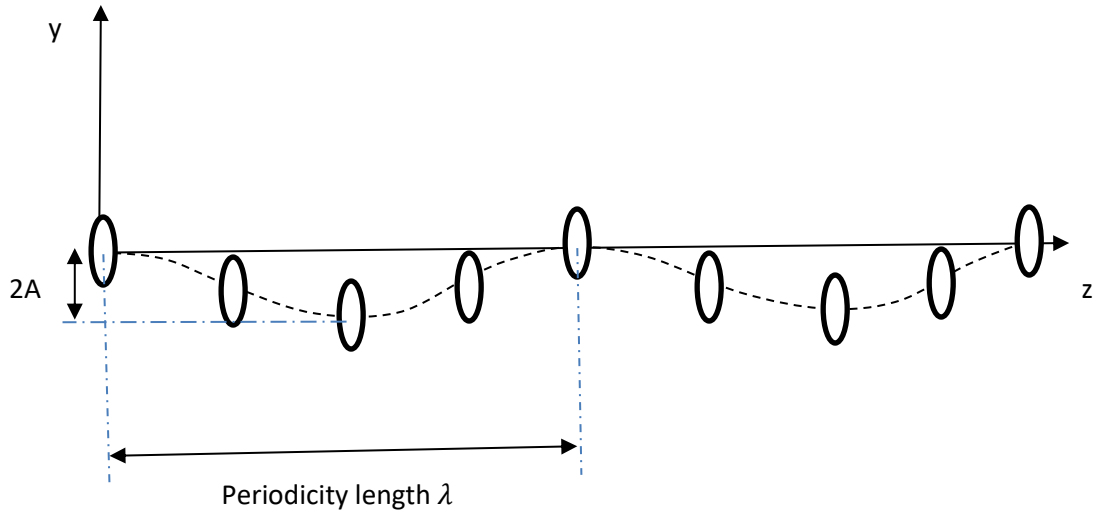

Figure V.3. The S-shaped absorber construction [9].

The S-shaped absorber length must be 48.72 m to replace the straight one. It was found by calculation that it is composed of 249 periodic curves of length 0.195 m, and the last 16.5 cm is considered straight.

V.2.1.1. Heat flux around the S-shaped absorber

In Tonatiuh software, importing the S-shaped absorber geometry as an STL file and running the Monte Carlo simulation to obtain heat flux distribution is possible. However, there is no way to export the results, as Tonatiuh post-processing supports only simple geometries (straight pipes for parabolic troughs or a disk in dish concentrators).

Demagh et al. [9] considered that the S-shaped geometry is just a series of tiny straight pipes with different positions relative to the focal line with their corresponding heat flux distribution. In addition, they suggest that the optical efficiency remains the same in both straight and corrugated absorbers as the optical properties of the parabola, the glass cover, and the solar absorber are independent of geometry, and only the intercept factor increased with a ratio of the length between straight and corrugated absorbers.

The previous approach will be used in this study. The heat flux of the S-shaped absorber will be obtained as different local heat flux of straight absorber for different positions (bending) as shown in Table V.3 below, proposed by Demagh et al. [9].

Table V.3. The coordinates of points of the first periodic curve used in heat flux generation [9].

Cross section order	z (m)	Δ (m)
1 & 17	0 and λ	0
2 & 16	0.02243021 and $\lambda - 0.02243021$	2.5×10^{-3}
3 & 15	0.0325 and $\lambda - 0.0325$	5×10^{-3}
4 & 14	0.04090801 and $\lambda - 0.04090801$	7.5×10^{-3}
5 & 13	0.04875 and $\lambda - 0.04875$	10×10^{-3}
6 & 12	0.056592 and $\lambda - 0.056592$	12.5×10^{-3}
7 & 11	0.065 and $\lambda - 0.065$	15×10^{-3}
8 & 10	0.075069788 and $\lambda - 0.075069788$	17.5×10^{-3}
9	$\lambda/2 = 0.0975$	20×10^{-3}

In the recent versions of the swak4FOAM library, the lookup2DTable utility is developed to read tables with two variables and supports 2D interpolation. It will import the heat flux tables of different positions and couple them with OpenFOAM external wall boundary conditions.

The heat flux distributions for different bending are shown below in Figure V.4

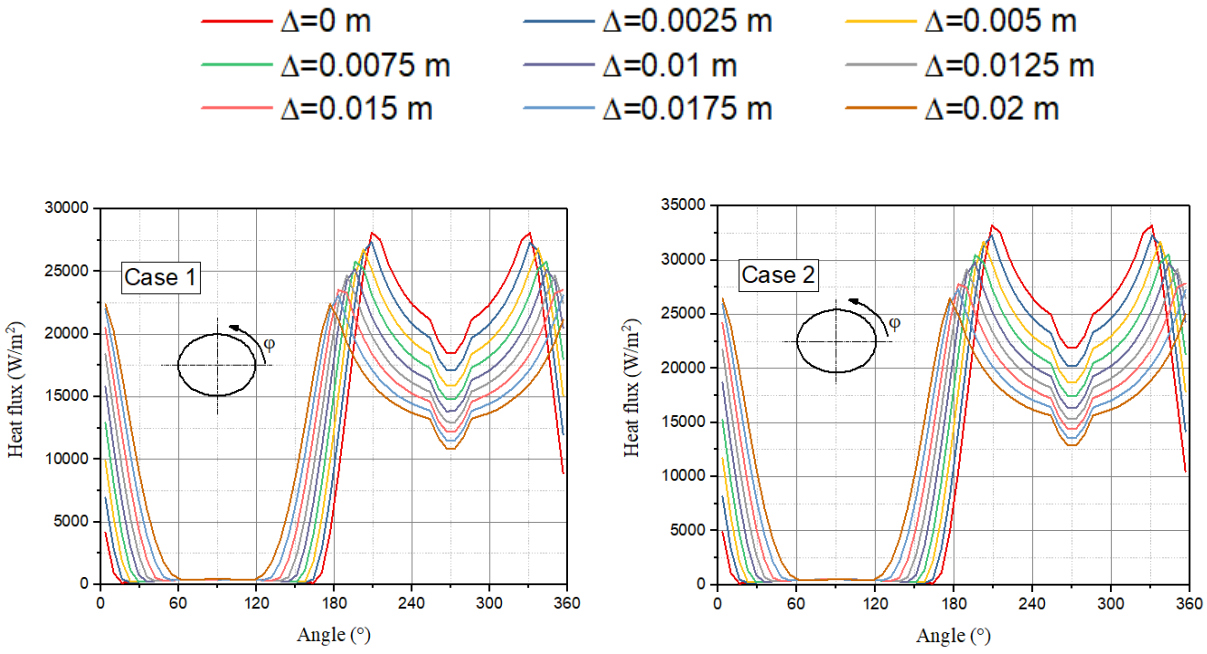

Figure V.4. 2D heat flux distribution for different bending in S-shaped absorber affected by optical efficiency.

The heat flux distribution for both the circumferential angle and the periodic length is shown below in Figure V.5.

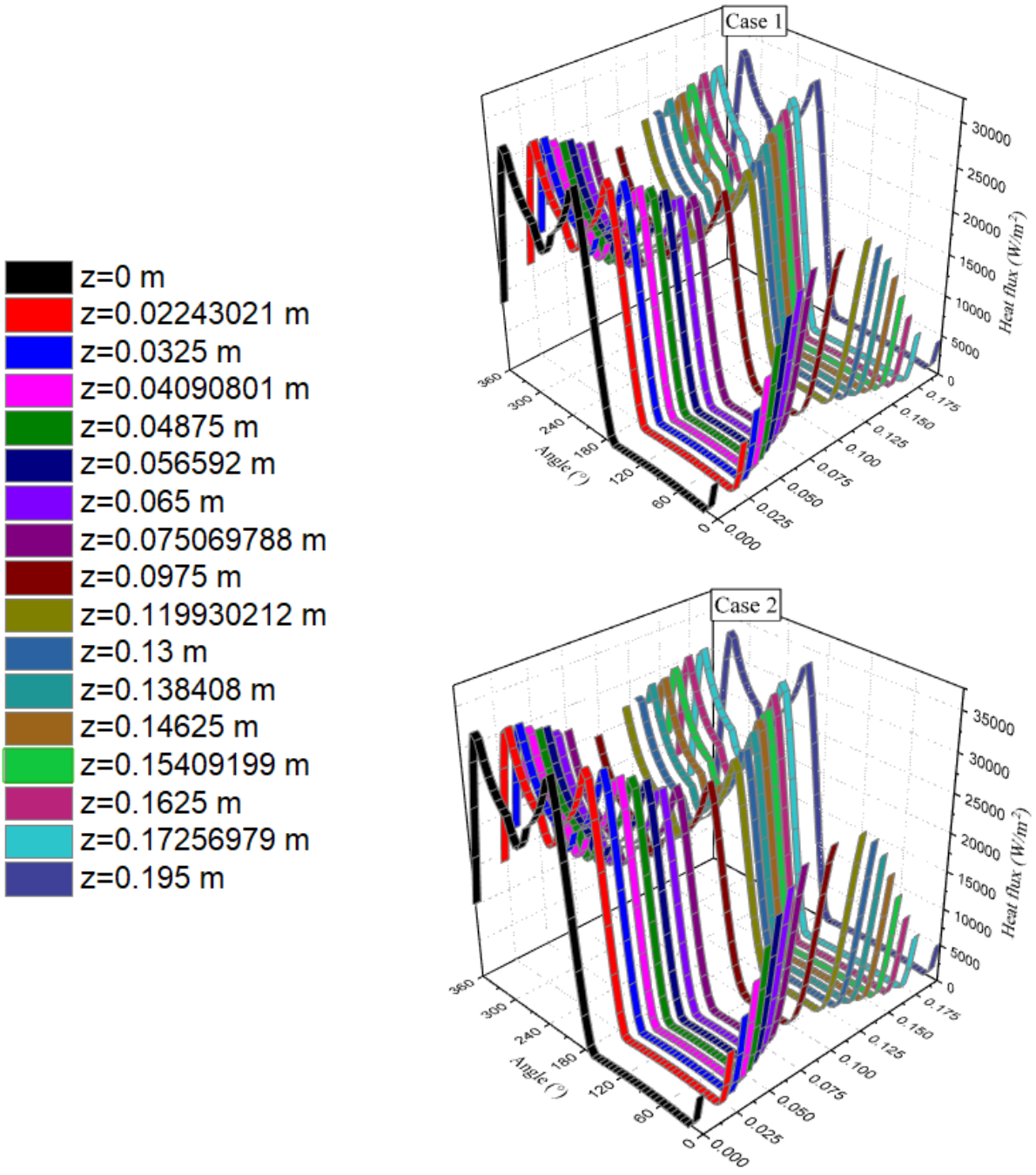

Figure V.5. 3D heat flux distribution for different locations in the z direction in the S-shaped absorber.

The obtained heat flux at the external wall boundary conditions for both cases is shown in Figure V.6 compared with the straight absorber.

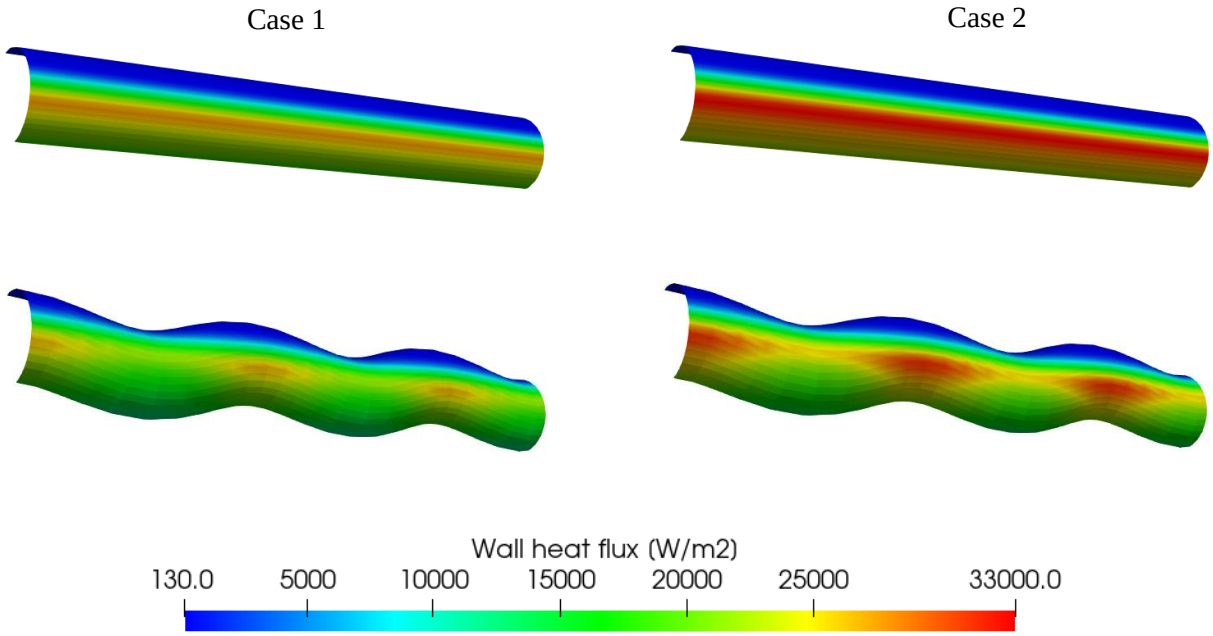

Figure V.6. 3D heat flux distribution for both straight and S-shaped absorbers.

As for the straight absorber, the energy absorbed by the S-shaped solar receiver is defined below in equation V.3

$$q_{eff} = q - q_{loss} \tag{V.3}$$

Where q is the mean heat flux, it is applied at the absorber's outer surface after a multiple heat flux reduction due to the optical efficiency of different collector components (mirror, glass cover, solar absorber, Etc.).

(q) can also be described as the mean of the sum of local actual heat fluxes around the absorber:

$$q = \eta \cdot \frac{1}{2\pi} \cdot \int_{0}^{2\pi} q(\varphi, z) d\varphi \tag{V.4}$$

$q(\varphi, z)$ represents the heat flux distribution around the S-shaped absorber.

V.2.2. Boundary conditions

As in the previous chapter, the mathematical model and the boundary conditions remain the same, except for the turbulence model, where the sato SST k omega is used. The noun-uniform wall heat flux at the external wall is coded by groovyBC in the external library called swak4FOAM using lookupTables2D.

The boundary conditions for the fluid and solid regions are grouped in Tables V.(4, 5), respectively.

Table V.4. Boundary conditions for the fluid region in the S-shaped absorber.

Variables	Inlet	Outlet	Interface fluid-solid	Symmetry
α_g	fixedValue	inletOutlet	zeroGradient	symmetryPlane
α_l	Calculated	Calculated	Calculated	SymmetryPlane
$\alpha t_g, \alpha t_l$ (wall partitioned heat flux model)	Calculated	Calculated	Compressible: alpha-BoilingWallFunction	symmetryPlane
U_l / U_g	fixedValue	pressureInletOutlet-Velocity	fixedValue (0 0 0)	symmetryPlane
T_l	fixedValue	inletOutlet	Compressible: turbulentTemperature-TwoPhaseRadCouple-Mixed	symmetryPlane
T_g	fixedValue	inletOutlet	copiedFixedValue	symmetryPlane
$Prgh$ $(P - \rho gh)$	fixedFluxPr-essure	prghPressure	fixedFluxPressure	SymmetryPlane
P	Calculated	Calculated	Calculated	SymmetryPlane
k_l / k_g	fixedValue	inletOutlet	kqRwallFunction	symmetryPlane
ω_l / ω_g	fixedValue	inletOutlet	omegaWallFunction	symmetryPlane
$\mu_{t,l}$ / $\mu_{t,g}$	Calculated	Calculated	nutkWallFunction	symmetryPlane

Table V.5. Boundary conditions for the solid region in the S-shaped absorber.

Variables	Inlet wall	Outlet wall	External wall	Interface solid-fluid	Symmetry
T	zeroGradient	zeroGradient	groovyBC	Compressible: turbulent-Temperature-TwoPhase-RadCouple-Mixed	Symmetry -Plane

The applied external wall temperature is defined as:

$$-\lambda_a \frac{\partial T}{\partial n} = \left(\eta \cdot q(\varphi, z)\right) - \frac{\sigma\left(T_{a,wall}^4 - T_g^4\right)}{\frac{1}{\epsilon_a} + \frac{\left(1-\epsilon_g\right)}{\epsilon_g}\left(\frac{D_{a,outer}}{D_g}\right)} \quad (V.5)$$

Where:

$q(\varphi, z)$ represents the heat flux distribution (2D table) obtained by the Monte Carlo method considering perfect optical efficiency.

(η) is the overall optical efficiency. It remains the same as in the straight absorber due to the optical characteristics are not affected by the geometry change $\left(\alpha_a \tau_g R\right)^{S-curved} = \left(\alpha_a \tau_g R\right)^{straight}$(look in the Reference work of Demagh et al. [9]), only the intercept factor $\gamma^{S-curved} \neq \gamma^{Straight}$ due to the geometry change, and Demagh et al. [9] considered :

$$\frac{\gamma^{S-curved}}{\gamma^{Straight}} = \frac{l^{S-curved}}{l^{Straight}} \quad (V.6)$$

Where $l^{S-curved}$ and $l^{Straight}$ are the lengths of S-shaped and straight absorbers, respectively. Thus, the overall optical efficiency is $(\eta = 0.51167)$, as in the straight absorber.

q_{loss} considers heat loss by radiation only because the annular zone between the absorber and glass cover is a vacuum [6]. In the previous chapter, the energy loss by radiation adopted from [11, 12] (look equation V.7) is validated with the experimental correlation of heat loss in the LS3 collector of the DISS facility [13]. It can also be used in the S-shaped absorber:

$$q_{loss} = \frac{\sigma\left(T_{a,wall}^4 - T_g^4\right)}{\frac{1}{\epsilon_a} + \frac{\left(1-\epsilon_g\right)}{\epsilon_g}\left(\frac{D_{a,outer}}{D_g}\right)} \quad (V.7)$$

V.2.3. Mesh independency

The first collector of case 1 is considered for the mesh independence check. Two meshes with different cross-section divisions are adopted because it has been found in previous validations in chapters 3 and 4 that the Eulerian method is not sensitive to mesh refinement.

The mesh refinement near the wall is coarse due to the use of the omega wall function. When using an immensely refined mesh adjacent to the wall, the time step becomes very small to satisfy Courant number $CFL < 1$, making the time simulation reach the steady state very long.

The mesh in Salome Meca 2017 is performed with hexahedral type. The division of the cross-section is built for the central square and extruded for the divided S line to construct the corrugated geometry, as shown in Figure V.7 below:

The difference in the numerical total pressure drop between the inlet and outlet of the solar absorber between mesh 1 (coarse) and mesh 2 (fine) is 2.01%, and the mean external wall temperature is the same, which indicates that mesh 1 can be used for the rest of the simulations.

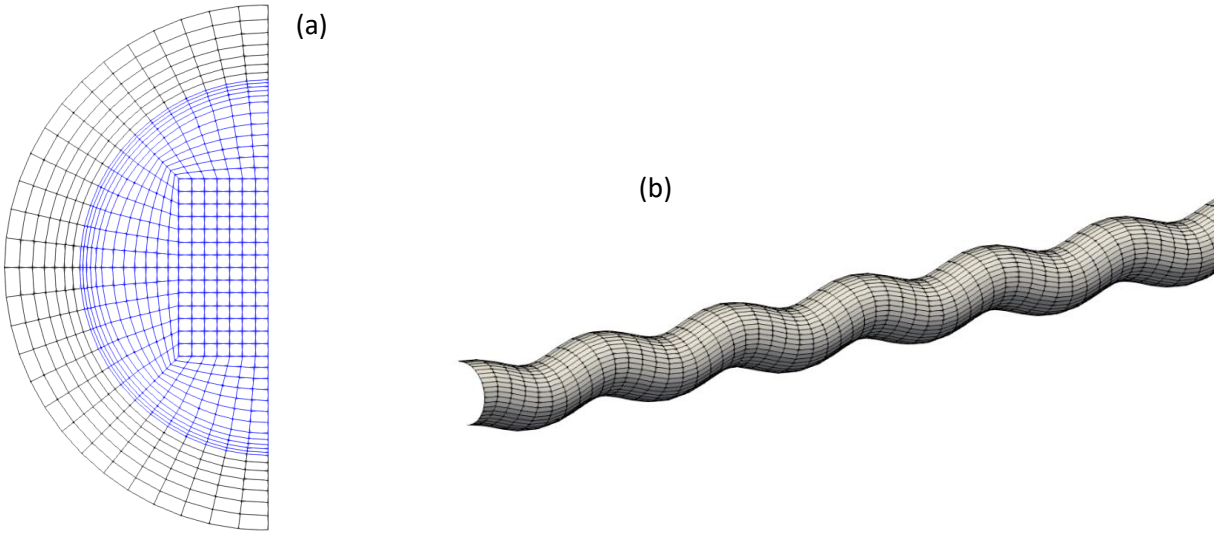

Figure V.7. The S-shaped absorber mesh generated by Salome Meca 2017. (a) Cross-section meshing, (b) Axial meshing.

Table V.6. Mesh independnce test (case 1 Collector #2).

	Total pressure drop between inlet and outlet	Mean temperature of external surface of absorber
Mesh 1 (925 000 nodes)	5831.9	520.4266
Mesh 2 (1 575 000 nodes)	5951.8	520.4274

V.3. Results and discussion

In order to compare the thermo-hydraulic behaviour of the DSG in the parabolic trough for both straight and S-shaped absorbers accurately with high fidelity, the inlet of each collector of the straight absorber will be used in the new S-shaped absorber with the mapFieldDict utility in OpenFOAM to ensure the same inputs for both phases distribution, which enables to compare collector by collector for both geometries. The simulations of the S-shaped absorber are

performed for collectors (#2, #3, #4, #5, #6, and #7) for both cases, as it is sufficient for the general comparison.

V.3.1. The pressure drop

The total pressure drop for each collector is the sum of frictional and momentum pressure drops. The comparison of total pressure drop between the straight and the S-shaped absorbers for both cases is shown in Figure V.8. It is observed that the total pressure drop in the S-shaped absorber is more significant than the straight one by 16.54% for case 1 for the studied collectors (Colls #2, #3, #4, #5, #6, and #7) and 26.42 % for case 2. For the first two collectors, the total pressure drop for both absorbers tends to be similar, while the difference increases in middle collectors (4-6). On the other hand, the peak of the total pressure drop is shifted from collector 7 in the S-shaped absorber to collector 6 in the straight one.

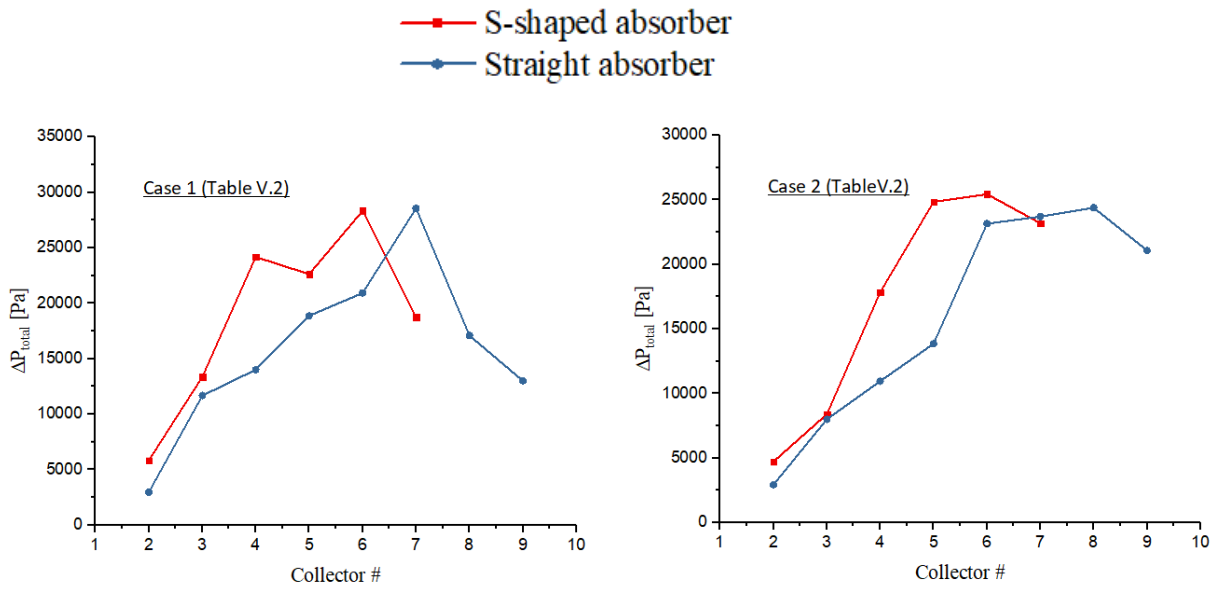

Figure V.8. Comparison between numerical total pressure drop for straight and S-shaped absorbers.

The same observations are stated in the frictional pressure drop in Figure V.9; a slight difference is remarked in the low vapour quality, then it increases with the increase in vapour quality for both cases until it reaches its peak, which is noticed in the S-shaped absorber before the straight one.

Generally, the frictional pressure drop increased in the S-shaped absorber compared to the straight one, with 16.4% for case 1 for the same vapour quality comparison points and 24.43% for case 2.

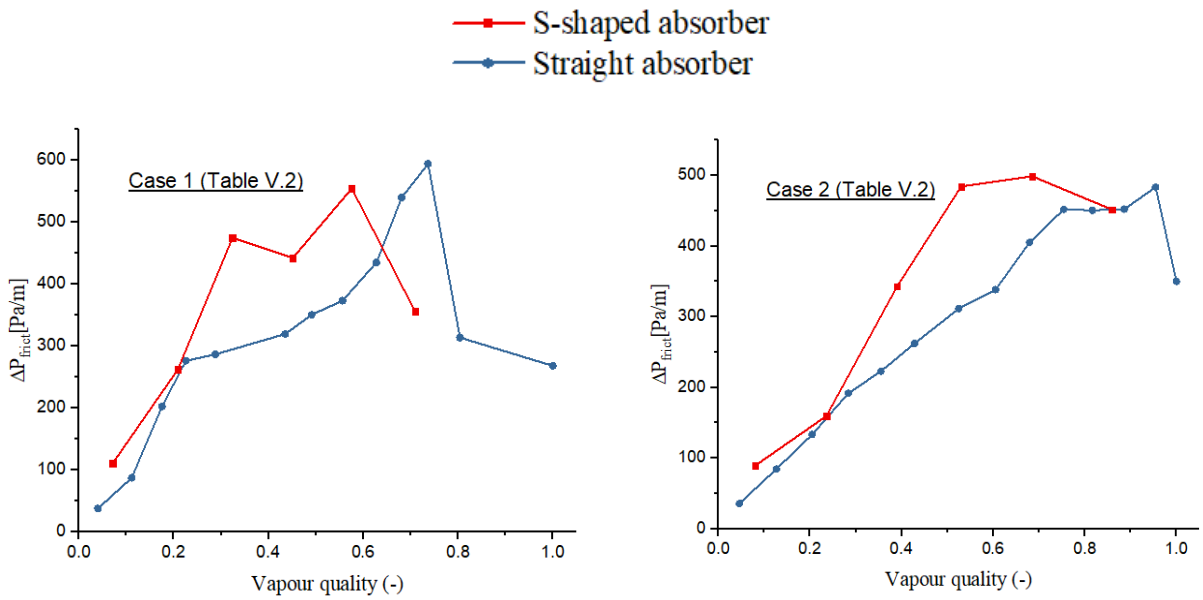

Figure V.9. Frictional pressure drop: numerical results for straight and S-shaped absorbers.

V.3.2. Two-phase distribution

In the straight absorber, a stratified flow is observed in all collectors in both cases, as the Eulerian method does not track the interface between the liquid and the vapour. This observation is still acceptable, as the flow patterns such as stratified wavy, slug, and intermittent are defined as mean stratified flow with different stratified angles in the literature [14, 15]. The same observations are remarked in the numerical study of DSG in the parabolic trough with the Eulerian method done by Pal and Kumar [16]. The annular flow cannot be obtained by this method, even in the VOF method with interface tracking technique; it is challenging to obtain an annular flow where researchers [17, 18] impose the two-phase distribution at the inlet to facilitate the creation of annular flow either by a mathematical equation [17] or impose annular distribution at the inlet [18].

In the coiled and corrugated geometries, the Eulerian two-fluid method choice is better than the VOF approach as the bubbles coalesce and split continuously due to the mixed flow imposed by the bends (it does not require interface capture as one phase fluctuates in the other). It makes the VOF method very expensive (highly refined mesh demands).

The Wojtan et al. [15] maps for Two-phase flow that track the phase distribution during the evaporation in the straight absorber for both cases are shown below in Figure V.10.

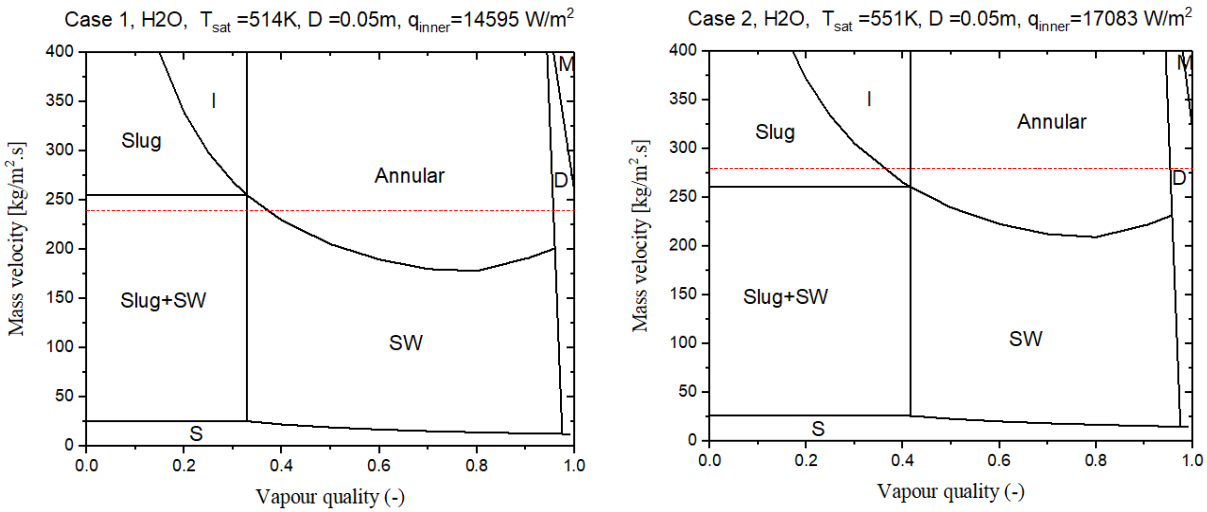

Figure V.10. Two-phase distribution for both cases in the straight absorber obtained by Wojtan et al. [15] map.

It is clear from the map that the flow patterns for both cases in the straight absorbers transform from stratified wavy (SW)/Slug to annular flow (A), then ultimately Dryout and mist flows.

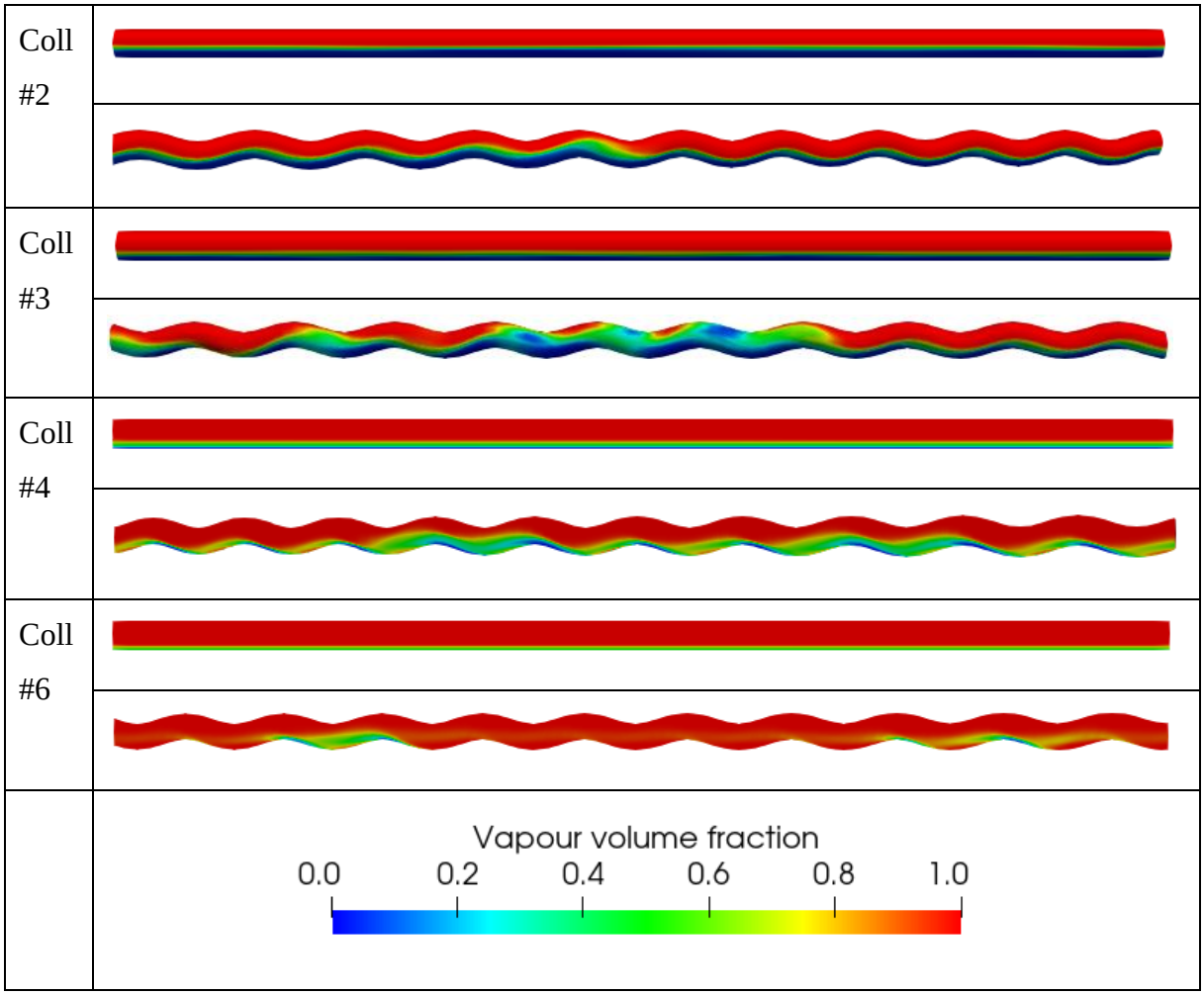

Figure V.11. Two-phase distribution in straight and corrugated absorbers for case 1.

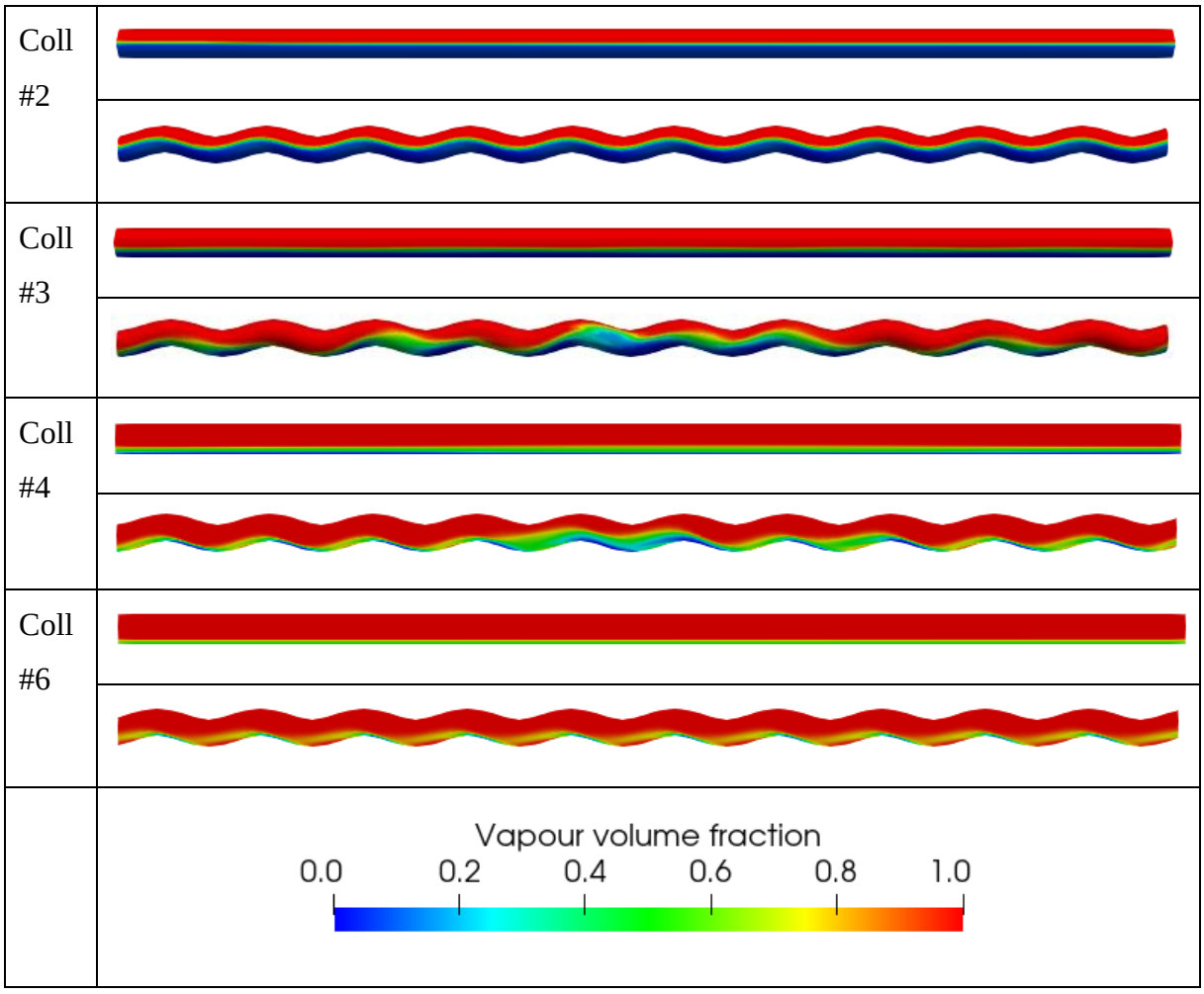

Figure V.12. Two-phase distribution in straight and corrugated absorbers for case 2.

In the DSG in the parabolic trough, the annular flow is the preferred flow pattern as it has the highest heat transfer coefficient by evaporation because the periphery of the absorber is wet. At the same time, stratified (S) and stratified wavy (SW) are avoided because the upper part of the absorber is dry due to the existence of the vapour with low conductivity that can create a high circumferential temperature gradient and deform the absorber by thermal stress [19].

In Figures V.11 and 12, the two-phase distribution in the straight absorbers shows a stratified flow. In contrast, intermittent and stratified wavy flows are observed in the S-shaped absorber, enhancing the heat transfer coefficient.

According to Wojtan et al. map [15] (See Figure V.10), the annular flow starts at vapour quality ($x \approx 0.4$) corresponding to collector #4. It is evident to keep the straight absorber as it produces an annular flow with low pressure drop and easy manufacturing. On the other hand, for low vapour quality ($x < 0.4$) corresponding to collectors #2 and #3, it is preferable to use the S-shaped absorber as it repeatedly transforms the stratified wavy flow (SW) predicted in Wojtan et al. [15] map to slug or intermittent flow in which liquid touches the upper side of the absorber.

The S-shaped absorber is preferable to be used in the entire evaporation section when operating with a low mass velocity that produces stratified and stratified wavy flows (see Figure V.10).

V.3.3. Wall temperature

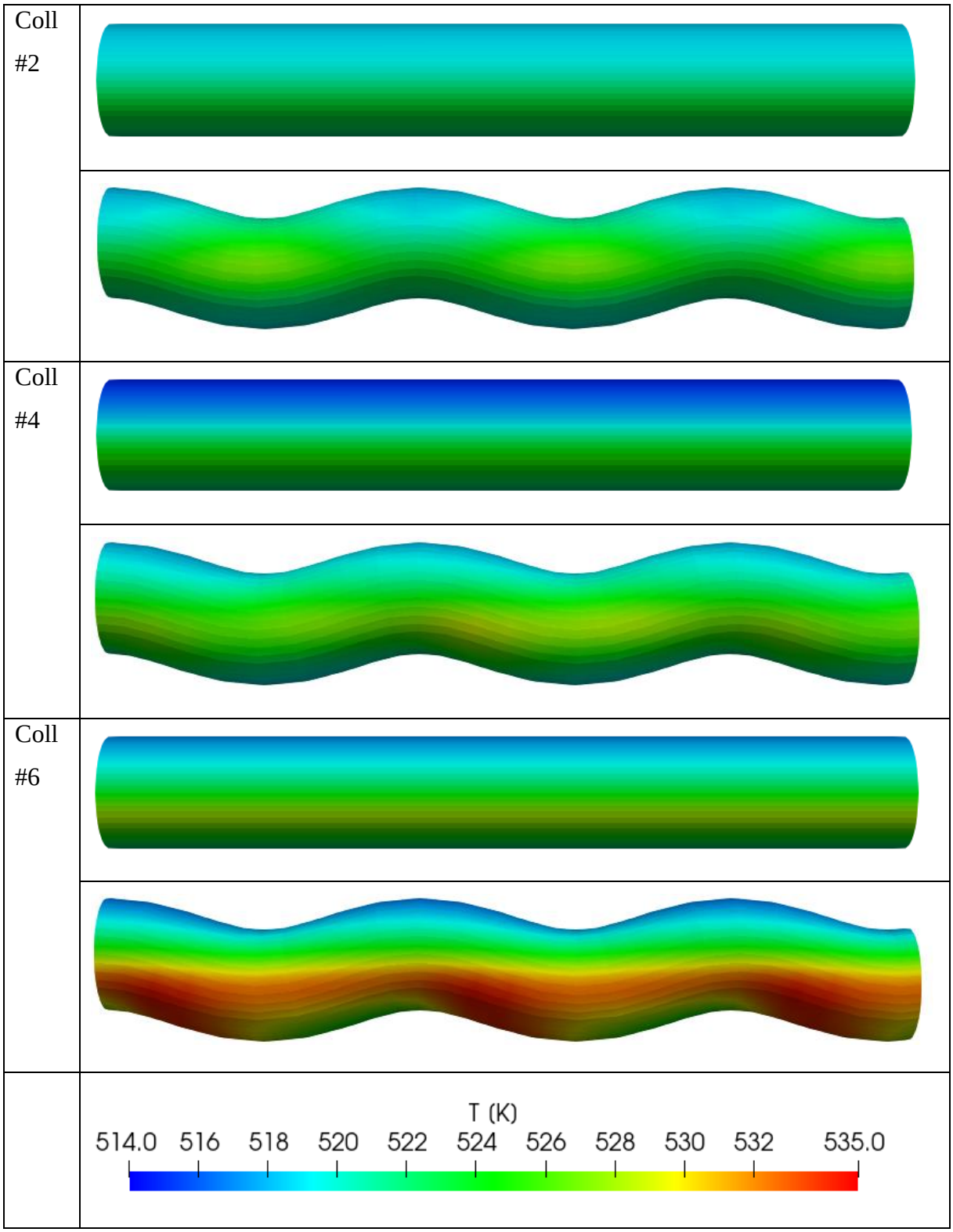

Figure V.13. Temperature distribution in straight and corrugated absorbers for case 1.

The wall temperature distribution in the S-shaped solar absorber is affected by the heat flux distribution as in the straight one. The higher temperature is observed in the bottom part of the absorber due to its higher heat flux. A comparison of temperature distribution is shown in Figures V.13 and V.14.

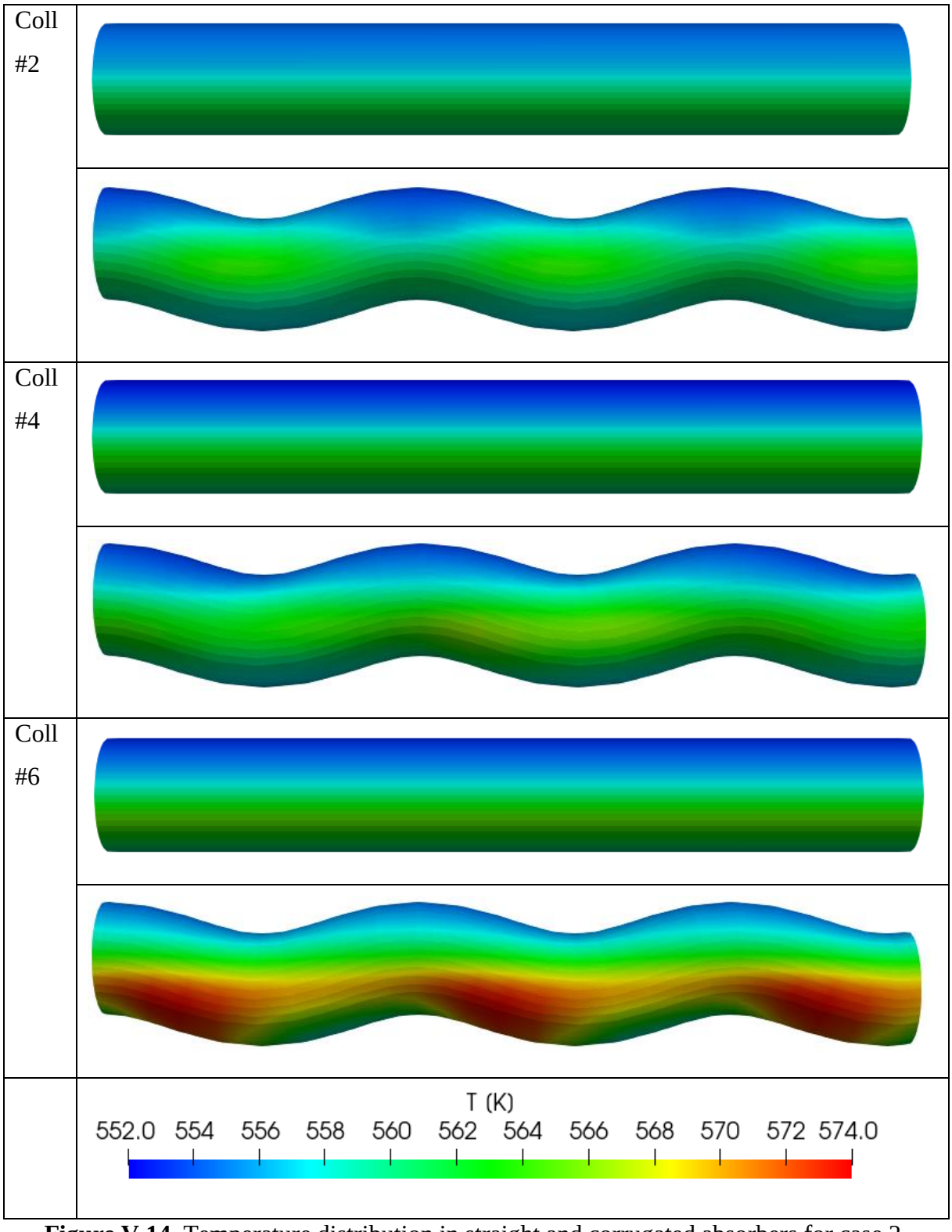

Figure V.14. Temperature distribution in straight and corrugated absorbers for case 2.

The temperature in the S-shaped absorber is higher than in the straight one, especially for collector 6 in both cases due to the absorber bends effect (look at Figures V.11 and V.12) that pushes the liquid away from the bottom part, which creates a vapour isolation layers that contribute to increasing temperature, especially the highest fluxes are applied there. However, the gradient temperature in the wall remains in the safe zone below 50 K.

The mean heat loss for both cases in collectors is shown in Table V.7 below:

Table V.7. Comparison of mean heat loss in each collector for straight and S-shaped absorbers.

	Mean heat loss in each collector $[W/m^2]$			
	Case 1		Case 2	
Collectors	Straight	S-shaped	Straight	S-shaped
#2	513.77	517.5817	750.638	754.126
#3	513.03	526.9032	754.049	768.864
#4	512.343	528.143	755.095	764.821
#5	514.553	541.8203	757.526	780.934
#6	523.692	546.59	762.016	794.476
#7	515.102	553.35	770.318	792.305

The heat loss in both cases for the straight and S-shaped absorbers is similar due to the same operating temperature and slight difference in temperature distribution around the absorbers.

V.4. Conclusion

The comparative numerical study between the S-shaped and the straight absorbers has been established for the same operating conditions in the DISS solar power facility. To ensure the fidelity of comparison, the heat flux around the absorber is simulated with the Monte Carlo method taking into account the effect of bending relative to the focal line on heat flux using the lookupTables2D utility in swak4FOAM that enables getting the heat flux in all points of the outer surface using 2D interpolation. The inlet of the S-shaped collector has the same inputs as the straight one by using the mapFields utility that enables mapping the fields and boundaries of different mesh divisions with high precision.

The comparison between both absorbers shows that:

- The pressure drop in the S-shaped absorber increased for case 1 by 16.54%, and case 2 by 26.42%.
- The frictional pressure drop in the S-shaped absorber increased by 16.4% for case 1 and 24.43% for case 2.
- The two-phase distribution in the S-shaped absorber showed stratified wavy, slug, and intermittent flow, in which the liquid can touch the upper side of the absorber and increase the heat transfer coefficient by evaporation.
- The temperature distribution in the S-shaped absorber is higher than in the straight one, especially for high vapour quality, where the bends push the liquid away from the bottom part of the tube, which creates an isolation layer of vapour that increases the temperature.
- The heat loss in both absorbers is similar.

References

[1] Eck M, Steinmann W. D. Modeling and design of direct solar steam generating collector fields. *J. Sol. Energy Eng*.2005; 127(3): 371-380.

[2] Hachicha A. A, Rodríguez I, Ghenai C. Thermo-hydraulic analysis and numerical simulation of a parabolic trough solar collector for direct steam generation. *Applied Energy*. 2018; 214: 152-165.

[3] Kumar B. N, Reddy K. S. Comparison of two-phase flow correlations for thermo-hydraulic modeling of direct steam generation in a solar parabolic trough collector system. *Journal of Thermal Science and Engineering Applications*. 2018; 10(4), 041005.

[4] Biencinto M, González L, Valenzuela L. A quasi-dynamic simulation model for direct steam generation in parabolic troughs using TRNSYS. *Applied energy*. 2016; 161: 133-142.

[5] Elsafi A.M. On thermo-hydraulic modeling of direct steam generation. *Solar Energy*. 2015; 120: 636-650.

[6] Lobón D. H, Baglietto E, Valenzuela L, Zarza E. Modeling direct steam generation in solar collectors with multiphase CFD. *Applied Energy*. 2014; 113: 1338-1348.

[7] Giglio A, Lanzini A, Leone P, García M. M. R, Moya E. Z. Direct steam generation in parabolic-trough collectors: a review about the technology and a thermo-economic analysis of a hybrid system. *Renewable and Sustainable Energy Reviews*. 2017; 74: 453-473.

[8] Dirker J, Juggurnath D, Kaya A, Osowade E. A, Simpson M, Lecompte S, ... & Markides C. N. Thermal energy processes in direct steam generation solar systems: Boiling, condensation and energy storage–A review. *Frontiers in Energy Research*. 2019; 6: 147.

[9] Demagh Y, Bordja I, Kabar Y, Benmoussa H. A design method of an S-curved parabolic trough collector absorber with a three-dimensional heat flux density distribution. Solar *Energy*. 2015; 122: 873-884.

[10] Demagh Y, Bordja L. A 1D thermal model for PTR including pressure drop and kinetic energy change within the fluid: conventional absorber tube vs. S-curved. *In AIP conference proceedings*, 2019..

[11] Bitam E, Demagh Y, Hachicha A, Benmoussa H, Kabar Y. Numerical investigation of a novel sinusoidal tube receiver for parabolic trough technology. *Applied Energy*. 2018; 218: 494-510.

[12] Forristall, R. *Heat transfer analysis and modeling of a parabolic trough solar receiver implemented in engineering equation solver*. (No. NREL/TP-550-34169). National Renewable Energy Lab, Golden, CO. (US). 2003.

[13] Valenzuela L, Zarza E, Berenguel M, Camacho E. F. Control concepts for direct steam generation in parabolic troughs. *Solar Energy*. 2005; 78(2): 301-311.

[14] Kattan N, Favrat D, Thome J. R. Flow Boiling in Horizontal Tubes. Part 3; Development of a New Heat Transfer Model Based on Flow Pattern. *Journal of heat transfer*. 1998; 120(1): 156-165.

[15] Wojtan L, Ursenbacher T, Thome J. R. Investigation of flow boiling in horizontal tubes: Part I—A new diabatic two-phase flow pattern map. *International journal of heat and mass transfer*. 2005; 48(14): 2955-2969.

[16] Pal R. K, Kumar R. Two-fluid modeling of direct steam generation in the receiver of parabolic trough solar collector with non-uniform heat flux. *Energy*. 2021; 226, 120308.

[17] Ban S, Pao W, Sakhir N. M. Numerical simulation of two-phase flow regimes in horizontal pipeline and its validation. *International Journal of Numerical Methods for Heat & Fluid Flow*. 2018; 28(6): 1279-1314.

[18] Thaker J. P, Banerjee J. CFD simulation of two-phase flow phenomena in horizontal pipelines using openfoam. *Proc. 40th National Conference on Fluid Mechanics. & Fluid Power*. 2013. India.

[19] Pal R. K, Kumar K. R. Investigation of thermo-hydrodynamics, structural stability, and thermal energy storage for direct steam generation in parabolic trough solar collector: A comprehensive review. *Journal of Cleaner Production*. 2021; 311, 127550.

General conclusion and perspectives

General conclusion and perspectives

This work aimed to study the direct steam generation in the parabolic trough in the DISS test facility (in Spain) using a new patent S-curved absorber with free software (Salome Meca, OpenFOAM, swak4FOAM, ParaView, and Tonatiuh). The main undesirable flow pattern in the DISS test facility is stratified flow, as it has the lowest heat transfer coefficient and can cause thermal stress in the solar absorber. The new S-curved absorber can disturb the flow distribution and overcome the stratified problems without any inserts that can cause water leakage or absorber bending due to the weight of the inserts. The geometry of the S-shaped absorber can affect the flow pattern by continuous centrifugal force effects up and down in the bends. It was the primary motivation to implement this work.

The DISS facility is vast, which is a CFD challenge. Many authors in the literature used 1D simulations in their studies using empirical correlations. However, in this study, 3D simulation is necessary as the absence of correlations that address the new geometry.

The Eulerian-Eulerian two-fluid method coupled with the RPI model is chosen in this study as it is accurate even in coarse meshes and does not contain a coefficient that must be calibrated in each simulation.

First, the validation was established on laboratory scales of horizontal straight and coiled tubes, and the results were consistent with the experiments. The coiled tube is chosen as it can represent the same physics as in the S-curved absorber and to check the reliability of the adopted mathematical model.

Second, the validation of the mathematical model has been established on the commercial scale of the straight absorber in the DISS test facility, and the results were in good agreement with the experimental data.

After the successful validations of the mathematical model for different geometries and scales, it has been used in the study of DSG in the DISS facility with the S-curved absorber as an alternative to the straight one under the same operating conditions, and the comparative study shows that:

- When the straight absorber produces stratified flow, the S-curved absorber could produce stratified wavy and slug flows, which is very favourable for increasing the heat transfer coefficient.
- The pressure drop in the S-curved absorber is more significant than in the straight one.

- The straight absorber can produce annular flow for specific mass velocities and vapour quality, which makes using the new absorber not recommended.
- For low DNI, which imposes low mass velocity that produces stratified flow (look Wojtan map in Figure V.10), it is recommended to use the new S-curved absorber in the whole evaporation section of the DISS facility.

As perspectives, it would be impressive to:

- Use a smaller periodic length of the corrugated S-curved absorber to enhance the effect of the centrifugal force in the two-phase distribution.
- Study the DSG inside the S-curved absorber experimentally for different periodic lengths.
- Use the VOF method to study DSG in the DISS facility with an S-curved absorber and compare it with the Eulerian-Eulerian obtained results.

Abstract

This numerical study focuses on the feasibility of the new solar receiver proposed and patented by Demagh Yassine in 2015 for linear concentrating modules. After the promising numerical results obtained in single-phase flow with synthetic oil, it was interesting to move towards the Direct Steam Generation (DSG) in parabolic trough collectors by adopting the scenario where this absorber would replace the conventional straight one in a full-scale installation like the DISS test facility in Almeria, Spain. First, the mathematical model was validated by comparison with experimental data for boiling flows in straight and coiled horizontal tubes at a laboratory scale and followed by validation under actual conditions in the commercial scale of the DSG in the DISS facility. Preforming 3D simulations in the OpenFOAM environment, the obtained numerical results were more than satisfactory. In the second step, the previously validated model is used to perform simulations of DSG in the DISS facility parabolic trough collector equipped with the new S-curve absorber in replacement of the conventional straight one; the same (actual) operating conditions are adopted for both absorbers for better performance comparison. The curved shapes of the tube greatly disturb the stratified flow by converting it into a stratified wavy and slug flows, further improving the evaporative heat transfer coefficient. It is evident that a penalty accompanies any improvement in thermal performance in terms of pressure drops, but it remains entirely acceptable. The S-curved absorber is not recommended when the conventional straight absorber can provide an annular flow alone, which is not always true.

Key words: Boiling flow, DSG, Parabolic trough, DISS test facility, S-shaped absorber, coiled tube, Monte Carlo Ray Tracing method.

Résumé

Cette étude numérique se concentre sur la faisabilité du nouveau récepteur solaire proposé et breveté par Demagh Yassine en 2015 pour les modules à concentration linéaires. Après les résultats numériques prometteurs obtenus en écoulement monophasique avec de l'huile synthétique, il était intéressant de passer à la génération directe de vapeur (Direct Steam Generation DSG) dans les collecteurs cylindro-paraboliques en adoptant le scénario où cet absorbeur remplacerait l'absorbeur conventionnel droit dans une installation à grande échelle comme l'installation d'essai DISS à Almería, en Espagne. Tout d'abord, le modèle mathématique a été validé par comparaison avec des données expérimentales pour les écoulements d'ébullitions dans des tubes horizontaux droits et hélicoïdaux à l'échelle de laboratoire, et suivi d'une validation dans des conditions réelles à l'échelle commerciale de DSG dans l'installation DISS. Par l'exécution de simulations 3D dans l'environnement OpenFOAM, les résultats numériques obtenus étaient plus que satisfaisants. Dans la deuxième étape, le modèle précédemment validé est utilisé pour effectuer des simulations de DSG dans le collecteur cylindro-parabolique de l'installation DISS équipée du nouvel absorbeur à courbe en S en remplacement de l'absorbeur droit classique; les mêmes conditions de fonctionnement (réelles) sont adoptées pour les deux absorbeurs pour une meilleure comparaison des performances. Les formes courbées du tube perturbent énormément l'écoulement stratifié en le convertissant en un écoulement stratifié ondulé et en bouchon, et améliore d'avantage le coefficient de transfert thermique par évaporation. Il est évident qu'une pénalité accompagne toujours toute amélioration de performances thermiques en termes de pertes de charge, mais elle reste tout à fait acceptable. L'absorbeur à courbe en S n'est pas recommandé lorsque l'absorbeur conventionnel droit peut fournir à lui seul un écoulement annulaire, ce qui n'est pas toujours vrai.

Mots clés : Écoulement en ébullition, DSG, Les cylindro-paraboliques, installation d'essai DISS, absorbeur solaire en forme de S, Tubes hélicoïdaux, La méthode Monte Carlo de poursuite de rayons.

ملخص

تركز هذه الدراسة على استخدام براءة الاختراع الجديدة لامتصاص الطاقة الشمسية التي قدمها دماغ ياسين في عام 2015 ، بعد نتائجه العددية الواعدة التي تم الحصول عليها في التدفق أحادي الطور مع الزيت الاصطناعي ، كان من المفضل استخدام هذا الماص المنحني كبديل الماص المستقيم في منشأة توليد البخار المباشر في حوض مكافئ مع محاكاة حقيقية على نطاق واسع. أولاً ، قمنا بالتحقق من صحة النموذج الرياضي بمقياس مختبري مع دراسات تجريبية لتدفق الغليان في أنابيب أفقية مستقيمة وملفوفة ، وبعد أن حصلنا على نتائج مرضية ، تحققنا من صحة النموذج الرياضي بمقياس حقيقي لمنشأة توليد البخار المباشر ، وكانت النتائج متوافقة مع بيانات التجربة ، وكانت واحدة من الدراسات القليلة التي تتعامل مع محاكاة ثلاثية الأبعاد في هذا المجال. ثانيًا ، استخدمنا هذا النموذج الرياضي الذي تم التحقق من صحته لمحاكاة توليد البخار في حوض القطع المكافئ باستخدام جهاز الامتصاص المنحني الجديد كبديل للنموذج المستقيم لنفس ظروف التشغيل. وجدنا أن هندسة هذا الماص يغير التدفق الطبقي ويحوله إلى تدفقات مموجة وطبقية ، وهو أمر مرغوب فيه للغاية لتقليل الإجهاد الحراري في الممتص وتعزيز معامل انتقال الحرارة عن طريق التبخر. تشمل عيوب هذا الامتصاص المنحني مقارنة بالممتص المستقيم زيادة انخفاض الضغط ولا يوصى باستخدامه عندما يمكن للممتص المستقيم توفير تدفق حلقي.

الكلمات الأساسية: توليد البخار المباشر ، حوض مكافئ ، مرفق اختبار توليد البخار المباشر DISS ، جهاز امتصاص على شكل حرف S ، طريقة مونت كارلو لتتبع الأشعة.